Cloud Geometry for Passive Remote Sensing

Tobias Kölling

Munich 2020

Cloud Geometry for Passive Remote Sensing

Tobias Kölling

Dissertation
at the Faculty of Physics
of Ludwig–Maximilians–Universität
Munich

submitted by
Tobias Kölling
born in Starnberg

Munich, 16 January 2020

1^{st} supervisor: Prof. Dr. Bernhard Mayer
2^{nd} supervisor: Prof. Dr. Markus Rapp
Date of oral exam: 20.05.2020

Wolkengeometrie für passive Fernerkundung

Tobias Kölling

Dissertation
an der Fakultät für Physik
der Ludwig–Maximilians–Universität
München

vorgelegt von
Tobias Kölling
aus Starnberg

München, den 16. Januar 2020

Erstgutachter: Prof. Dr. Bernhard Mayer
Zweitgutachter: Prof. Dr. Markus Rapp
Tag der mündlichen Prüfung: 20.05.2020

Warum sollten wir über Wolken sprechen, Mister Stevens?

Sie sind schön.

Bjorn Stevens
in DIE ZEIT
19.07.2018

Abstract

An important cause for disagreements between current climate models is lack of understanding of cloud processes. In order to test and improve the assumptions of such models, detailed and large scale observations of clouds are necessary. Passive remote sensing methods are well-established to obtain cloud properties over a large observation area in a short period of time. In case of the visible to near infrared part of the electromagnetic spectrum, a quick measurement process is achieved by using the sun as high-intensity light source to illuminate a cloud scene and by taking simultaneous measurements on all pixels of an imaging sensor. As the sun as light source can not be controlled, it is not possible to measure the time light travels from source to cloud to sensor, which is how active remote sensing determines distance information. But active light sources do not provide enough radiant energy to illuminate a large scene, which would be required to observe it in an instance. Thus passive imaging remains an important remote sensing method. Distance information and accordingly cloud surface location information is nonetheless crucial information: cloud fraction and cloud optical thickness largely determines the cloud radiative effect and cloud height primarily influences a cloud's influence on the Earth's thermal radiation budget. In combination with ever increasing spatial resolution of passive remote sensing methods, accurate cloud surface location information becomes more important, as the largest source of retrieval uncertainties at this spatial scale, influences of 3D radiative transfer effects, can be reduced using this information. This work shows how the missing location information is derived from passive remote sensing. Using all sensors of the improved hyperspectral and polarization resolving imaging system specMACS, a unified dataset, including classical hyperspectral measurements as well as cloud surface location information and derived properties, is created.

This thesis shows how RGB cameras are used to accurately derive cloud surface geometry using stereo techniques, complementing the passive remote sensing of cloud microphysics on board the German High-Altitude Long-Range research aircraft (HALO). Measured surface locations are processed into a connected surface representation, which in turn is used to assign height and location to other passive remote sensing observations. Furthermore, cloud surface orientation and a geometric shadow mask are derived, supplementing microphysical retrieval methods. The final system is able to accurately map visible cloud surfaces while flying above cloud fields. The impact of the new geometry information on microphysical retrieval uncertainty is studied using theoretical radiative transfer simulations and measurements. It is found that in some cases, information about surface orientation allows to improve classical cloud microphysical retrieval methods. Furthermore, surface information helps to identify measurement regions where a good microphysical retrieval quality is expected. By excluding likely biased regions, the overall microphysical retrieval uncertainty can be reduced. Additionally, using the same instrument payload and based on knowledge of the 3D cloud surface, new approaches for the retrieval of cloud droplet radius exploiting measurements of parts of the polarized angular scattering phase function become possible. The necessary setup and improvements of the hyperspectral and polarization resolving measurement system specMACS, which have been developed throughout four airborne field campaigns using the HALO research aircraft are introduced in this thesis.

Zusammenfassung

Ein wichtiger Grund für Unterschiede zwischen aktuellen Klimamodellen sind nicht ausreichend verstandene Wolkenprozesse. Um die zugrundeliegenden Annahmen dieser Modelle zu testen und zu verbessern ist es notwendig detaillierte und großskalige Beobachtungen von Wolken durch zu führen. Methoden der passiven Fernerkundung haben sich für die schnelle Erfassung von Wolkeneigenschaften in einem großen Beobachtungsgebiet etabliert. Für den sichtbaren bis nahinfraroten Bereich des elektromagnetischen Spektrums kann eine schnelle Messung erreicht werden, in dem die Sonne als starke Lichtquelle genutzt wird und die Wolkenszene durch simultane Messung über alle Pixel eines Bildsensors erfasst wird. Da die Sonne als Lichtquelle nicht gesteuert werden kann, ist es nicht möglich die Zeit zu messen die von einem Lichtstrahl für den Weg von der Quelle zur Wolke und zum Sensor benötigt wird, so wie es bei aktiven Verfahren zur Distanzbestimmung üblich ist. Allerdings können aktive Lichtquellen nicht genügend Energie bereitstellen um eine große Szene gut genug zu beleuchten um diese Szene in einem kurzen Augenblick vollständig zu erfassen. Aus diesem Grund werden passive bildgebende Verfahren weiterhin eine wichtige Methode zur Fernerkundung bleiben. Trotzdem ist der Abstand zur beobachteten Wolke und damit der Ort der Wolke eine entscheidende Information: Wolkenbedeckungsgrad und die optische Dicke einer Wolke bestimmen einen Großteil des Strahlungseffektes von Wolken und die Höhe der Wolken ist der Haupteinflussfaktor von Wolken auf die thermische Strahlungsbilanz der Erde. Einhergehend mit der weiterhin zunehmenden Auflösung von passiven Fernerkundungsmethoden werden genaue Informationen über den Ort von Wolkenoberflächen immer wichtiger. Dreidimensionale Strahlungstransporteffekte werden auf kleineren räumlichen Skalen zum dominierenden Faktor für Fehler in Messverfahren für Wolkenmikrophysik. Dieser Einfluss auf die Messverfahren kann durch die Nutzung von Informationen über die Lage der Wolken reduziert und die Ergebnisse somit verbessert werden. Diese Arbeit zeigt, wie die fehlenden Ortsinformationen aus passiven Fernerkundungsmethoden gewonnen werden können. Damit kann ein vereinheitlichter Datensatz aller Sensoren des verbesserten specMACS-Systems für hyperspektrale und polarisationsaufgelöste Bilderfassung erstellt werden, in dem außer den gemessenen Strahlungsdichten auch die Positionen der beobachteten Wolkenoberflächen und daraus abgeleitete Größen enthalten sind.

In dieser Arbeit wird gezeigt, wie RGB-Kameras genutzt werden, um mit Hilfe stereographischer Techniken die Geometrie der beobachteten Wolken ab zu leiten und so die

Möglichkeiten zur passiven Fernerkundung auf dem Forschungsflugzeug HALO zu erweitern. Aus den so gemessenen Positionen der Wolkenoberflächen wird eine geschlossene Darstellung der Wolkenoberflächen berechnet. Dies ermöglicht es die Daten aus anderen passiven Fernerkundungsmethoden um Höhe und Ort der Messung zu erweitern. Außerdem ist es so möglich die Orientierung der Wolkenoberflächen und eine Schattenmaske auf Grund der nun bekannten Beobachtungsgeometrie zu berechnen. Das fertige System ist in der Lage, die sichtbaren Wolkenoberflächen aus Daten von einem Überflug zu rekonstruieren. Mit Hilfe theoretischer Strahlungstransportsimulationen und Messungen wird der Einfluss der neu gewonnenen Informationen auf bestehende Rekonstruktionsmethoden für Wolkenmikrophysik untersucht. In manchen Fällen helfen die neu gewonnenen Informationen direkt die Ergebnisse dieser Methoden zu verbessern und in jedem Fall ermöglichen es die Positionsdaten Bereiche zu identifizieren für die bekannt ist, dass bisherige Rekonstruktionsmethoden nicht funktionieren. Durch Ausschluss solcher Bereiche wird der Gesamtfehler von Mirkophysikrekonstruktionen weiterhin reduziert. Das aktuelle specMACS System ermöglicht auch polarisationsaufgelöste Messungen, wodurch eine sehr genaue Bestimmung der Wolkentropfengrößen möglich wird. Die nun verfügbaren Positionsdaten der Wolkenoberflächen helfen die Genauigkeit dieses Verfahrens deutlich zu verbessern. Die notwendigen Auf- und Umbauten des hyperspektralen und polarisationsauflösenden Messsystems specMACS, die während vier Flugzeuggestützer Messkampagnen auf dem Forschungsflugzeug HALO entwickelt wurden sind in dieser Arbeit beschrieben.

Contents

Chapter 1

Introduction

Clouds are and have always been fascinating objects, known to everyone since being a child. Despite being virtually present every day, they are hard to grasp physically. The imagination of standing or walking on a cloud is very common, which implies that most people have some intuition about what and where the surface or boundaries of a cloud might be. This intuition also manifests in common quantities (cloud base height, cloud top height and cloud cover) which are used in meteorological observations. Despite of this intuitively simple concept, in reality it is very hard to quantify cloud boundaries universally. Cloud fraction has been known to be an ill-posed quantity for decades (Slingo and Slingo, 1988) and an impressive illustration of this difficulty is given by Stevens et al. (2019), where a typical cloud field during the NARVAL-II field campaign has been observed using various independent active and passive remote sensing techniques in order to determine the cloud cover (Fig. 1.1). The results range from 19 % to 45.9 % between different measurement techniques for the same cloud field, a very large spread for such a supposedly simple problem.

While looking at beautiful clouds is generally a good idea, looking at them in a scientific way is important as well. Climate change has been studied for decades, yet large uncertainties in the estimated radiative forcing due to anthropogenic emissions remain (IPCC, 2013). Dufresne and Bony (2008) decomposed climate feedbacks of the 12 global climate models of the third phase of the Coupled Model Intercomparison Project CMIP3 into various driving mechanisms and show that by far the largest source of inter model differences result from cloud feedbacks. Furthermore, it has been shown that differences in cloud feedback primarily arise from the response of low-level clouds (Bony and Dufresne, 2005; Webb et al., 2006; Wyant et al., 2006). It is concluded that the understanding of the underlying physical processes is not yet developed well enough and better parameterizations of cloud-scale processes are required. Consequently, the World Climate Research Programme has formulated the goal to the better understanding of Clouds, Circulation and Climate Sensitivity as one of it's grand challenges (Bony et al., 2015). Due to the earth's temperature profile, low-level clouds are typically liquid water clouds. In particular

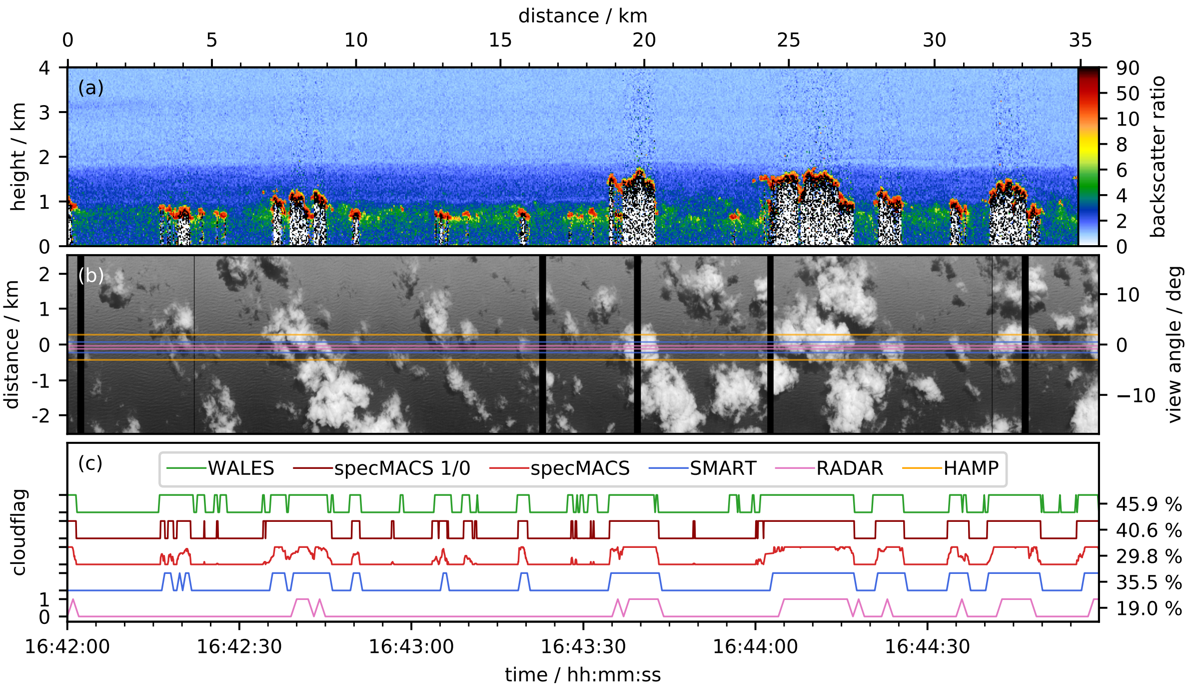

Figure 1.1: Comparison of cloud masks using different remote sensing instruments. (a) The lidar perspective: a vertical cut through the scene showing the backscatter ration from the WALES lidar (Wirth et al., 2009). (b) Top view: a horizontal view at the scene from the hyperspectral imager specMACS (Ewald et al., 2016). (c) Cloud flags along the centerline from different sensors on board the HALO aircraft during the NARVAL-II field campaign. From Stevens et al. (2019).

shallow trade wind cumuli are the cloud type with the highest frequency of occurrence on earth and their radiative effect is very sensitive to changes in environmental conditions (Bony et al., 2017).

In order to better understand the behaviour of low-level liquid water clouds, it is required to capture the physical properties of the clouds and their surrounding by measurements. Besides the aforementioned visible cloud properties size and location, liquid water content and droplet size distribution define how clouds interact with radiation and subsequently the climate. In fact, droplet effective radius (Hansen and Travis, 1974) describes most of the droplet radiation interaction and is commonly used for first estimates of the droplet size distribution. This work focusses on the effective radius accordingly. The classic approach for effective radius retrievals is the combination of passive observations at two different wavelengths from the satellite perspective. By assuming a plane-parallel atmosphere, a look-up table can be obtained, which relates the two radiance values to cloud optical thickness (or liquid water path) and droplet effective radius (Nakajima and King, 1990). Operational retrievals based on this method can be found on commonly used spaceborne imagers, such as the Moderate Resolution Imaging Spectroradiometer (MODIS), the Advanced Very High Resolution Radiometer (AVHRR), and the Spinning Enhanced Visible Infrared Imager (SEVIRI) (King et al., 2003; Platnick et al., 2003; Roebeling et al., 2006). These satellites provide a relatively coarse spatial resolution in the order of 1 km and the retrievals are applied to stratiform clouds and thereby the plane-parallel assumption is a valid approach. Improving spatial resolution to values well below 1 km however leads to higher inaccuracies in the retrieved quantities. Davis et al. (1997) discuss the radiative smoothing scale η_{rad}, which describes the size of the region in which radiation is transported horizontally in a cloud and thus the area across which radiative effects get smoothed. They conclude that radiation measurements of clouds should be averaged across 200 m to reduce effects from pixel cross-talk. The authors further state that the application of plane-parallel theory on scales less than 600 m leads to an underestimation of small-scale variability due to radiative smoothing.

Typical trade wind cumuli are neither large nor stratiform as can be seen in Figure 1.1. These clouds feature a detailed structure at scales well below 1 km and many clouds are even smaller than that. At this small scale, the measurable radiance can quickly be dominated by effects of three dimensional (3D) radiative transfer and information about droplet size or water content can not be retrieved, if the three dimensional structure is not accounted for. Finite cloud geometry in more than one dimension creates a big challenge for both, the forward computation of radiance fields and even more so for the retrieval of cloud microphysical properties. Typical one dimensional models can not be generalized into three dimensional counterparts and proper three dimensional models require orders of magnitude higher computational effort.

Davies (1978) investigated how irradiance on a finite sized cuboidal cloud behaves differently from the plane-parallel assumption using Monte Carlo methods and also an analytical approximation. The studied cases correspond to the comparison between Fig. 1.2 (a) and (b). An important observation being that clouds of small horizontal extent, compared to their thickness, will appear darker than compared to their plane-parallel counterpart. Várnai and Marshak (2002) show the influence of three dimensional radiative transfer effects on cloud optical thickness retrieved from MODIS data. Later, Várnai and Marshak (2003) describe a method for analyzing the influence of different parts of clouds on each other's brightness. Vant-Hull et al. (2007) looked at effects of 3D cloud geometry on the retrieval of droplet effective radius. Common to all these approaches is the insight, that some knowledge of the 3D cloud structure is required to properly account for 3D radiative effects. However, estimating the 3D cloud structure from observations is even more difficult than computing the influence of a given cloud structure on the radiance field. Zinner et al. (2006) developed a method which allows to estimate 3D cloud structure for marine stratocumulus clouds when observed at low solar zenith angles using an iterative scheme of deconvolution and Monte Carlo forward simulations.

Ideas on how to correctly handle three dimensional cloud structures evolved further since Marshak et al. (2006) asked what cloud side observations can tell about the vertical

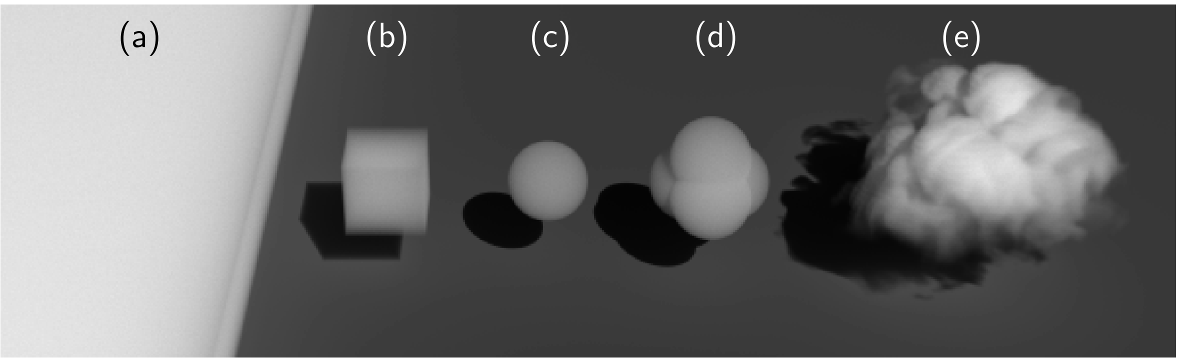

Figure 1.2: 1D vs 3D radiative transfer: The scene shows a series of artificial clouds. (a) the edge of a semi-infinite plane-parallel cloud slab, corresponding to an observed cloud in plane-parallel theory. (b) a cuboidal cloud of the same geometrical and optical thickness. (c) a sphere, which has the same diameter as the edge length of the cube. (d) a pyramid of four intersecting spheres. (e) a realistic cloud shape, produced by a run of UCLA-LES (Stevens et al., 2005), which has been provided by Fabian Jakub. For the illustration, all scattering phase functions of the cloudy volumes have been set to the same double Henyey-Greenstein phase function as in Davies (1978). The image has been computed using RayLi.

evolution of cloud droplet size. As cloud sides (Fig. 1.2(e)) certainly can not be approximated using the assumption of one dimensional horizontal clouds and the investigation of the vertical profile requires spatial resolutions well below 1 km, they investigated the possibility to use data from 3D radiative transfer simulations as a basis for a statistical retrieval of cloud droplet size in the presence of 3D cloud structure. The idea has been further refined and tested using simulations of realistic 3D cloud fields (Zinner et al., 2008; Ewald et al., 2019) and successfully applied to aircraft observations (Martins et al., 2011; Ewald, 2016). The methods are based on the evaluation of a large set of 3D radiative transfer simulations, which can be used as a look-up table for a probability distribution of possible droplet effective radii matching the measured combination of radiances, sun and observation angle.

Highly resolved microphysical properties need to be associated with location information to actually provide an added value. Consequently Ewald et al. (2019) conclude: "The height and location assignment of retrieval results is [. . .] of uttermost importance for the comparison with in situ measurements and models". Additionally, Ewald et al. (2019) point out that an unknown cloud surface orientation leads to an ambiguity of radiance measurements in bi-spectral effective radius retrievals. Thus a better knowledge of cloud surface orientation might directly improve the accuracy of a droplet effective radius retrieval. Given that cloud geometry information is important for a better understanding of clouds, it is important to account for the ambiguities between the different methods to retrieve cloud boundaries. Several studies indicate that large parts of the differences can be explained by different sensor resolutions, different spectral regions or viewing geometries (e.g. Roebeling et al., 2006; Pavicic, 2018).

The different findings in the literature indicate that if a retrieved cloud boundary should be transferred between measurements of different instruments, the instruments should operate at similar parts of the electromagnetic spectrum and at comparable spatial resolution. Furthermore, they should observe the scene from the same viewing geometry. Such requirements can be fulfilled if cloud geometry is retrieved from the same sensors or different cameras which are co-located near the spectral sensors. The following research questions target the derivation and application of cloud geometry information and are answered in this study:

- Can cloud geometry be determined from passive airborne remote sensing in the solar spectral range?
- Can this information be used to improve optical and microphysical property retrievals of inhomogeneous clouds?

In order to investigate these questions, 2D RGB imagers have been added to the existing specMACS hyperspectral imagers from the Ludwig-Maximilians-Universität (LMU) in Munich. The combined system has been adapted such that it can be operated on board the HALO research aircraft as part of the cloud observatory configuration (Stevens et al., 2019). The combined system has been operated during a series of field campaigns on board the HALO research aircraft. Based on the data obtained during these field campaigns, a method to retrieve cloud surface geometry has been developed and validated. Furthermore, the bi-spectral retrieval method for cloud microphysical properties according to Nakajima and King (1990) has been adapted to consider cloud surface orientation as an additional input and the applicability of that method has been evaluated using theoretical and experimental studies.

Chapter 2

Theory

This work is about the retrieval of cloud geometry and microphysical properties by means of passive remote sensing. Accordingly, the measured data is the amount of light or, more general, radiation received at the sensor. In order to relate the measured radiation at the sensor to properties at the clouds location, the process of transferring radiation throughout the atmosphere and the interaction of radiation and cloud microphysics must be understood. Additional to the microphysical properties, the scene and observation geometry must be considered carefully in the process. This section covers the theoretical background of these topics.

2.1 Solar Radiative Transfer in the Atmosphere

This thesis is based on passive optical measurements in the solar spectral range. While these measurements are taken at the location of the respective cameras, the values of the measured quantities are influenced by everything the light has passed from it's way from the sun through the atmosphere and into the sensor. Consequently, understanding the measurements requires to understand how light is influenced along this path. While in general, light is only a special case of an electromagnetic field which can be described by Maxwell's equations, solving these equations for a large problem domain like the earth's atmosphere is infeasible. Luckily, the largest part of the light path can be described by classical geometric optics and the easier to solve radiative transfer theory. This section is based on Pharr et al. (2017) with influences from Mayer (2009) and own ideas.

2.1.1 Radiative Quantities

Radiative transfer theory describes how radiant energy (Q) moves through space. As the speed of light is very high compared to other processes in the atmosphere, radiative transfer problems can usually be solved in steady-state. Thus the more interesting quantity is radiant flux or power (Φ) which is the amount of radiant energy per unit time:

$$\Phi = \frac{dQ}{dt} \tag{2.1}$$

When measuring radiant flux, the measurement device will have a finite surface area (A) which can receive the radiative energy. This leads to the term of irradiance (E), the amount of flux received by a given surface:

$$E = \frac{d\Phi}{dA} \tag{2.2}$$

The surface in this case is the surface perpendicular to the direction of incoming radiance. If in stead the receiving surface is tilted with respect to the incoming radiance, the effective surface area is reduced by the cosine of the angle of incidence (Lambert, 1892, p.22) and thus:

$$E' = \frac{d\Phi}{\cos\Theta \cdot dA} \tag{2.3}$$

This thesis observes radiant flux using different kinds of cameras, which additional to their finite lens area also feature directional sensitivity. This adds the opening angle (Ω) or instantaneous field of view (IFOV) to the picture and leads to radiance (L):

$$L = \frac{d\Phi}{dA \cdot d\Omega} \tag{2.4}$$

Of course, radiance is suspect to Lambert's cosine law accordingly. For spectrally resolved measurements, the received power is also broken down by wavelength and accordingly measured in terms of spectral radiance L_λ:

$$L_\lambda = \frac{d\Phi}{dA \cdot d\Omega \cdot d\lambda} \tag{2.5}$$

As this thesis does not cover effects like fluorescence or phosphorescence, radiances of different wavelengths do not interact and can be considered as independent. For that reason, spectral radiance is often used implicitly.

Radiance is likely the most important quantity in radiative transfer theory as it is usually conserved along an unobstructed light path and other quantities can be derived from radiance by integration over unused differentials. In Figure 2.1, the observer (red arc) on the left side is closer to the light source (Φ) than the observer on the left. Accordingly, the emitted flux is distributed over a smaller area and the received irradiance is higher. Conversely, as the left observer is further away from the light source, it can see more of the radiating area of the light source, which leads to more received power. Both effects scale with r^2 so they cancel out exactly and lead to the conservation of radiance along a light path. Note that in both cases, the opening angle is equal but infinitesimal, so as long as the light source is of finite extent, it will always be possible to see more of it by moving further away.

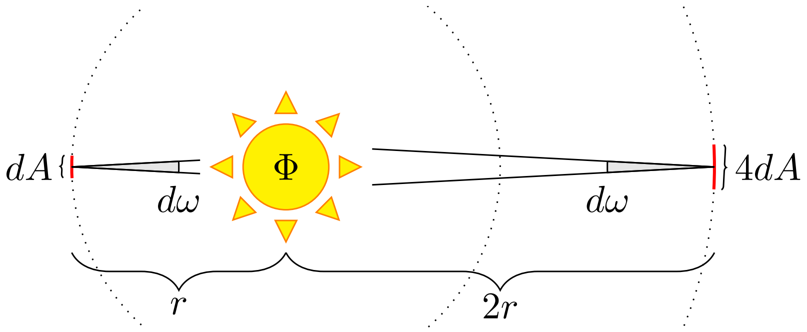

Figure 2.1: Without an interacting medium, radiance is conserved along a light path. While a close observer (red arc on the left) gets more radiance due to the smaller area across which the source flux is distributed, the observer on the right sees more of the light sources area. Both effects compensate exactly and thus, radiance is conserved along a light path.

It can also be useful to consider infinite light sources, which typically appear in two kinds. One is an infinitely far away light source, the other is an infinitely small (point-like) light source. A closer look at these cases reveals a slightly different behaviour of radiance and irradiance. An infinitely far away light source can be seen as a light source which only emits light in perfectly perpendicular rays. It may be of a finite extent and is illustrated in Fig. 2.2 (b). Independent of how far the observer is away from the light source, the receiving area will not change and as such, the irradiance E stays constant. Interestingly, the radiance L is constant in this case as well, but for a different reason. While the infinite opening angle conceptually sees more of the light sources area, it actually does not receive more radiance as the angular distribution of the radiance leaving the light source is described by a delta distribution. In other words, only the tiny portion of the opening angle which is perfectly parallel to the emitted light will receive any radiance and this portion does not increase with distance. The other case, a point-like light source (Fig. 2.2 (c)) can be explained using a similar reasoning. In this case, irradiance E scales as expected with $1/r^2$, however the radiance L does not stay constant anymore. For the radiance, the receiving area increases as in the finite case (a), but the area observed from the light source does not increase, similarly to the previous case. As a result, in the case of a point-like light source, radiance is not conserved anymore along the light path, but in stead also scales with $1/r^2$.

For radiative transfer calculations in the atmosphere, the sun usually can be considered as being infinitely far away, which leads to case (b) above and has the advantage that radiance is conserved along a path and no special treatment is needed. However, on the way from sun to earth, the finite distance between earth and sun has to be considered but the sun can be considered as a point source. The common way to handle this is that the extraterrestrial irradiance E_0 is determined by the $1/r^2$ rule, in particular to consider the earth's eccentricity (Iqbal, 1983). Starting from the top of the atmosphere this irradiance is then used to determine the emitting radiance of the sun, imagined as an infinitely far

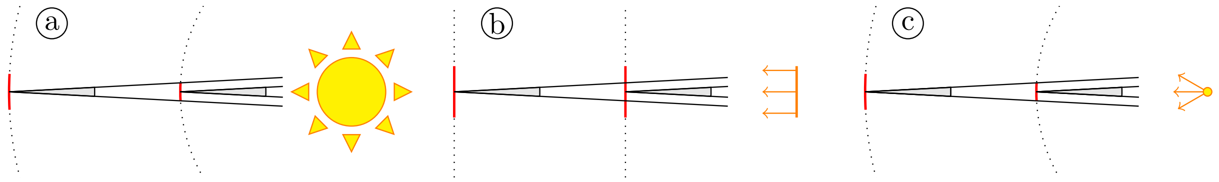

Figure 2.2: Differing behaviour of radiance and irradiance with finite and infinite light sources: (a) shows the usual case of a finite light source observed at different distances, (b) depicts a directional or infinitely far away light source and (c) shows an infinitely small light source at finite distance. Cases (b) and (c) require special treatment of the scaling behavior of radiance and irradiance.

light source.

2.1.2 Radiative Transfer in a Participating Medium

As radiance is usually conserved along an unobstructed light path, the interesting part of radiative transfer must be the case of a light path through a participating medium, e.g. the earth's atmosphere. The relevant processes can be seen by inspecting an infinitesimal chunk dt of such a light path through the medium (Figure 2.3). Let's assume the observer is located at position x. The question is, how much radiance can be observed at location x from a given direction Ω? As dt is small, the observed radiance will be the radiance on the other side of the chunk, modified by a small change: $L(x^-, \Omega) = L(x^+, \Omega) + dL$. Now, dL is determined by three processes which may happen inside the investigated volume. Light can be removed by absorption inside the medium, it can also be added by emission and it can change direction by scattering. For scattering, it is useful to distinguish between out-scattering and in-scattering as these two cases must be handled quite differently.

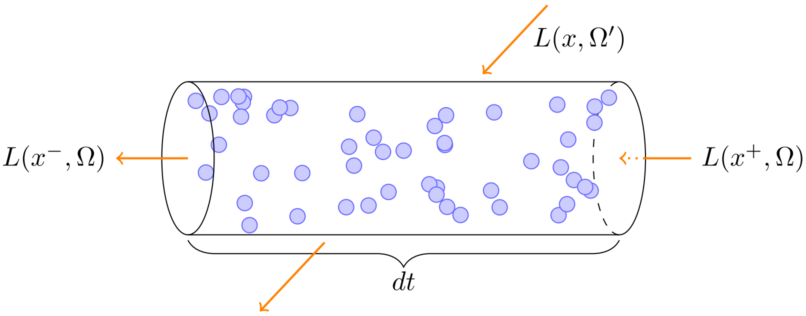

Figure 2.3: Radiative transfer in a participating medium. Radiation incident to a receiver $L(x^-, \Omega)$ is determined by radiance from further along the path $L(x^+, \Omega)$ as well as local emission, scattering and absorption.

Absorption and Out-Scattering

Absorption of light is proportional to the amount of incident light, the amount of absorbing particles and the particles ability to absorb light, described by the volume absorption coefficient k_{abs}, which can vary between different locations:

$$\frac{dL}{dt} = -k_{\text{abs}}(x)L(x,\Omega) \tag{2.6}$$

From the observer's point of view, *out-scattering* behaves much like absorption. This is not a surprise: in the end, light which is scattered out of the light path is not directly visible to the observer any more, so from the observer's point of view, it just disappears. Accordingly, out-scattering can be described just like absorption, but using the volume scattering coefficient k_{sca}:

$$\frac{dL}{dt} = -k_{\text{sca}}(x)L(x,\Omega) \tag{2.7}$$

As absorption and out scattering both reduce the amount of transmitted light in a similar manner, it is sometimes useful to express their combined effect using the extinction coefficient

$$k_{\text{ext}} = k_{\text{abs}} + k_{\text{sca}} \tag{2.8}$$

Additionally, it is customary to introduce the single scattering albedo

$$\omega = \frac{k_{\text{sca}}}{k_{\text{ext}}} \tag{2.9}$$

which describes the fraction of light which is scattered if it has hit a particle. The combined effect of absorption and out-scattering on transported radiance can be described by

$$\frac{dL}{dt} = -k_{\text{ext}}(x)L(x,\Omega) \tag{2.10}$$

which can be solved by integration from the observer at x to the source at $x' = x + d\Omega$, leading to *Bouguer Lambert Beer's Law* which describes the *transmittance* of a medium:

$$T(x' \to x) = e^{-\int_0^d k_{\text{ext}}(x+t\Omega)dt} \tag{2.11}$$

The negative exponent of this integral is called the *optical thickness* τ:

$$\tau(x' \to x) = \int_0^d k_{\text{ext}}(x+t\Omega)dt \tag{2.12}$$

while strictly speaking, τ is a quantity which describes optical properties of some medium on a straight line between two arbitrary points, τ is often meant to describe a vertical integral in meteorological context if not explained any further. Transmittance has two important properties, which follow directly from it's definition. First, is symmetric, so

$$T(x' \to x) = T(x \to x') \tag{2.13}$$

which allows to calculate transmittance between two points in either direction. Second, it is multiplicative, so for any point x'' between x and x'

$$T(x' \to x) = T(x' \to x'')T(x'' \to x) \tag{2.14}$$

which can be used to calculate transmittance for a sequence of finite parts of the atmosphere and later combine these parts to the full transmittance along a longer path.

Transmittance allows to calculate the amount of radiance received at the observer from a distant light source:

$$L(x, \Omega) = T(x + d\Omega \to x)L(x + d\Omega, \Omega) \tag{2.15}$$

As this equation is linear in the radiance of the light source, it allows to handle each light source separately and add the results up at the receiver. This property is also called *superposition principle* and will be used to handle emission and in-scattering, each of which can be treated as some form of light source.

Emission and In-Scattering

Emission is determined by the amount of emitting particles and their ability to emit light, described by the volume emission coefficient k_{em}:

$$\frac{dL}{dt} = k_{\text{em}}(x) \tag{2.16}$$

Using this as a distributed light source in Eq. 2.15 and integrating along the observed path leads to the amount of radiance received at location x from direction Ω due to emission in the atmosphere:

$$L(x, \Omega) = \int_0^d T(x + t\Omega \to x)k_{\text{em}}(x + t\Omega)dt \tag{2.17}$$

In-scattering is where the problem gets three-dimensional: the amount of light received by the observer is not only dependent on quantities along the observed light path, but also on light originating from all other directions, which involves integrating over the sphere around the scattering events happening at x:

$$\frac{dL}{dt} = k_{\text{sca}}(x) \int_{\mathcal{S}^2} \mathcal{P}(x, \Omega', \Omega)L(x, \Omega')d\Omega' \tag{2.18}$$

Here, $\mathcal{P}$ is the scattering phase function, which describes how light changes it's direction during the scattering event and is described in more detail in Section 2.1.3. Inserting in-scattering into Eq. 2.15 and integrating leads to the amount of light received at the observer due to in-scattering:

$$L(x, \Omega) = \int_0^d T(x + t\Omega \to x)k_{\text{sca}}(x + t\Omega) \int_{\mathcal{S}^2} \mathcal{P}(x + t\Omega, \Omega', \Omega)L(x + t\Omega, \Omega')d\Omega'dt \tag{2.19}$$

Combining equations 2.17 and 2.19 and substituting $x' = x + t\Omega$ leads to the radiative transfer equation:

$$L(x,\Omega) = \int_0^d T(x' \to x) \left(k_{\mathrm{em}}(x') + k_{\mathrm{sca}}(x') \int_{\mathcal{S}^2} \mathcal{P}(x',\Omega',\Omega) L(x',\Omega') d\Omega' \right) dt \tag{2.20}$$

2.1.3 Interaction Between Clouds and Radiation

Water clouds consist of many small liquid water droplets, suspended in the atmosphere. As most of such clouds are clearly visible by the human eye, clouds strongly interact with electromagnetic radiation. Clouds can have various different appearances, which is due to their different micro- and macrophysical composition. While some clouds can appear almost transparent, Cumulonimbus clouds can appear like a completely intransparent wall, so the amount of water certainly plays an important role. Furthermore, the amount of light scattered by a single droplet depends on it's scattering cross section and thus the droplet radius.

This thesis is about light in the solar (i.e. visible and near infrared) range of the electromagnetic spectrum. In this spectral range, radiation emitted at terrestrial temperatures can be neglected compared to radiation originating from the sun, so emission in the atmosphere will be ignored ($k_{\mathrm{em}} = 0$) in the following. It remains to describe scattering and absorption of clouds in terms of k_{abs}, k_{sca} and the scattering phase function $\mathcal{P}$ as introduced above, which are commonly called the optical properties of clouds.

Optical properties of small atmospheric volumes

As clouds typically contain 15 to 1300 droplets per cm^3 (Hess et al., 1998) and even high resolution models capable of representing entire clouds have grid resolutions in the order of several meters, is customary to compute and reason using a cloud volume with a droplet size distribution $n(r)$ instead of single droplets. A single spherical droplet is fully described by its radius, consequently the optical properties of all droplets of the same size are equal. Also, for a tiny volume, light will only interact with at most one of it's particles, so the effects of multiple particles will not interact with each other and simply add up (or average in case of $\mathcal{P}$) to the total effect. Accordingly, for an infinitesimal volume with a given size distribution, this allows to compute the optical properties sorted by droplet size, using the absorption (σ_{abs}) and scattering (σ_{sca}) cross sections of the single droplets:

$$k_{\mathrm{abs}} = \int_0^\infty n(r)\sigma_{\mathrm{abs}}(r)dr \tag{2.21}$$

$$k_{\mathrm{sca}} = \int_0^\infty n(r)\sigma_{\mathrm{sca}}(r)dr \tag{2.22}$$

$$\mathcal{P}_{\mathrm{vol}} = \frac{1}{k_{\mathrm{sca}}} \int_0^\infty n(r)\sigma_{\mathrm{sca}}(r)\mathcal{P}(r)dr \tag{2.23}$$

The same reasoning can be applied to the combination of different kinds of (not necessarily spherical) atmospheric constituents. This reduces the problem of finding the optical properties of a cloud volume to finding the optical properties of a single cloud droplet.

Scattering Phase Function

As briefly introduced above, the scattering phase function $\mathcal{P}(x, \Omega', \Omega)$ describes how light changes direction during scattering on a cloud particle. This is encoded by a probability density function, dependent on incident (Ω') and outgoing (Ω) direction. Generally, the phase function will look different for different atmospheric constituents, so there is an additional dependence on the location (x). As a probability density function, $\mathcal{P}$ is normed, both, for the integration over incoming directions (radiance must come from somewhere) and the integration over outgoing directions (radiance must go anywhere):

$$\int_{\mathcal{S}^2} \mathcal{P}(x, \Omega', \Omega) d\Omega = 1 \tag{2.24}$$

$$\int_{\mathcal{S}^2} \mathcal{P}(x, \Omega', \Omega) d\Omega' = 1 \tag{2.25}$$

For many atmospheric constituents[1], the orientation of the particles is not important, either because they are almost spherical, so there is no defined orientation, or because they are so well mixed that on average, they do not show a preferred orientation. In this case, the scattering phase function $\mathcal{P}$ is called isotropic and can also be expressed as function of the cosine of the scattering angle $\mathcal{P}(x, \cos(\Theta_{\text{sca}}))$ with $\cos(\Theta_{\text{sca}}) = \Omega' \cdot \Omega$.

Water clouds, the primary concern of this work, are composed of many little droplets, which are constantly falling relatively to the movement of the surrounding air. The shape of such small droplets can be accurately approximated as spherical (Pruppacher and Pitter, 1971) and consequently their scattering phase function must be isotropic. The size of cloud droplets is at a similar order of magnitude as the wavelength of solar radiation. Accordingly, geometric optics or the radiative transfer equation can not be used to describe the interaction of light and single cloud droplets. In stead the optical properties must either be derived experimentally, or by directly solving Maxwell's equation for the particle at hand. Using astronomical observations, Henyey and Greenstein (1941) experimentally derived a phase function, which is parameterized by an asymmetry parameter g:

$$\mathcal{P}_{\text{HG}}(\cos(\Theta_{\text{sca}})) = \frac{1}{4\pi} \frac{1 - g^2}{\sqrt{1 + g^2 + 2g\, cos(\Theta_{\text{sca}})}^3} \tag{2.26}$$

While this phase function is not entirely accurate for cloud droplets, is is often used for its simplicity.

---

[1] A notable exception are ice clouds, which are composed of ice crystals of many different shapes (Bailey and Hallett, 2009). While falling, these crystals tend to orient themselves in in a preferred direction (Jayaweera and Mason, 1965; Ono, 1969; Platt, 1978), this way, even on average the particle orientation matters.

For the case of spherical particles, a proper solution to Maxwell's equations has been shown by Mie (1908). In fact, while Mie primarily thought about metallic spheres in coloidal solutions, he already anticipated that the method could be applied to water droplets forming a rainbow, if only the arising computational challenges could be solved. Now, more then a century later, these challenges are less of a problem, software implementations are readily available (e.g. Wiscombe, 1980; Mayer and Kylling, 2005).

Figure 2.4 shows the two mentioned kinds of scattering phase functions. The plain Henyey Greenstein (HG) function with positive asymmetry parameter only shows a moderate forward peak (0°) and very few scatterings in backward direction (180°). A slight improvement towards a more realistic representation of scattering is the double HG function, which is the sum of one forward-peaked and one backward-peaked HG function. This function has been used for the illustration in Figure 1.2. Mie functions are parameterized by wavelength and droplet size. As mentioned before, it is customary to calculate Mie functions for a mixture of different droplet sizes within a small volume. The functions shown in Figure 2.4 use the default droplet size distribution from libRadtran. The notable differences between HG and Mie functions are the much steeper forward peak and the presence of additional peaks which form the cloudbow any the glory.

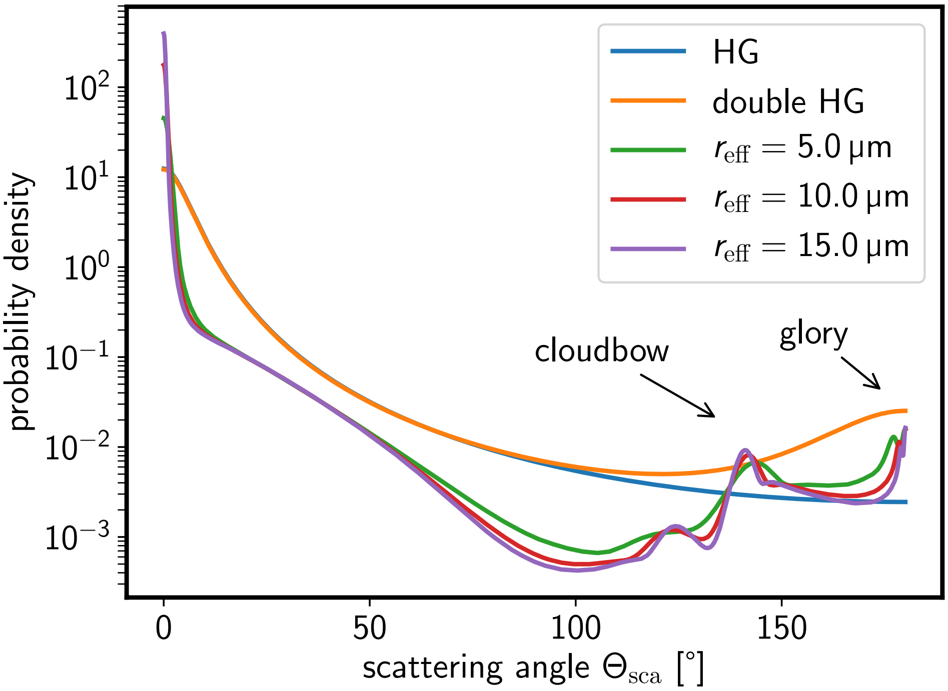

Figure 2.4: Exemplary phase functions derived for a gamma droplet size distribution with parameter $\alpha = 7$ and green light ($\lambda = 550\,\mathrm{nm}$) using the Mie tool from libRadtran (Mayer and Kylling, 2005).

Parameterization of the droplet size distribution

The entire droplet size distribution would be quite bulky, if used to describe the microphysical properties of a cloud. Additionally, the problem of retrieving the droplet size distribution from the measurement of only a few spectral lines would be massively under constrained. Luckily, for the interaction between droplets and radiation, only two parameters are of primary concern. First, as already mentioned above, there is the amount of droplets or water, which can be described by the Liquid Water Content (LWC). Second, as the droplet size mainly affects radiation through it's cross section, most of the remainder of the droplet size distribution is covered by the area weighted radius or "effective radius" r_{eff} (Hansen and Travis, 1974):

$$r_{\text{eff}} = \frac{\int r \pi r^2 n(r) dr}{\int \pi r^2 n(r) dr} \tag{2.27}$$

Hu and Stamnes (1993) created a parameterization scheme for obtaining optical properties without Mie calculations, intended to be used in climate models. During the development of the parameterization, they conducted many Mie computations and also conclude that optical properties are insensitive to the details of the droplet size distribution including shape, skewness, width and modality, as long as the effective radius is known.

Optical Thickness Rule of Thumb

For a quick estimate of optical thickness from microphysical properties, the following rule of thumb is very helpful:

$$\begin{aligned}
\sigma_{\text{e}}(r) &\approx 2\pi r^2 && (2.28)\\
k_{\text{e}} &= \sigma_{\text{e}}(r)\ N && (2.29)\\
\tau &= k_{\text{e}}\ \Delta z && (2.30)\\
N &= \frac{\text{LWC}}{\frac{4}{3}\pi r^3 \rho_{\text{H}_2\text{O}}} && (2.31)
\end{aligned}$$

Combining the equations from above and assuming r_{eff} represents a single droplet size and droplets are distributed isotropically throughout space, the following approximation for the optical thickness τ can be derived:

$$\tau \approx \frac{3}{2} \frac{\text{LWC}}{r_{\text{eff}}\ \rho_{\text{H}_2\text{O}}} \Delta z \tag{2.32}$$

If the density of water is approximated by $\rho_{\text{H}_2\text{O}} = 1000\,\frac{\text{kg}}{\text{m}^3}$ and clever units are chosen, this further simplifies to:

$$\tau \approx \frac{3}{2} \frac{\text{LWC}\left[\frac{\text{g}}{\text{m}^3}\right]}{r_{\text{eff}}\,[\mu\text{m}]} \Delta z\,[\text{m}] \tag{2.33}$$

Visible Cloud Surface

Visibility through a participating medium is an important quantity for example in car or air traffic, as speed limits or safe landing conditions depend critically on the ability to see any obstacles. Thus, it is no surprise that visibility has long been part of intensive studies. Of course, visibility is not only dependent on the medium, but also on the observer and the observed object. Koschmieder (1926) identified a set of useful definitions for the calculation of horizontal visibility and provides the "Koschmieder equation" for the visibility of a black body against the horizon:

$$s_s = \frac{1}{k_{\text{ext}}} \ln \frac{1+\epsilon}{\epsilon} \tag{2.34}$$

where s_s is the visual range and ϵ denotes the minimum detectable contrast. Koschmieder (1926, p.48) suggests a value of $\epsilon = 0.02$, which leads to a visibility in optical thickness:

$$\tau_{\max} = s_s k_{\text{ext}} \approx 3.9 \tag{2.35}$$

This shows that visibility can be expressed most easily in terms of optical thickness, in stead of geometrical distance. Furthermore, the choice of ϵ still depends on the observer and the observed object and has to be considered for the paricular application. So, if the cloud's structure is known in terms of optical thickness, under which conditions can a cloud be seen at all and how far can the observer look into a cloud? This can be checked by the forward simulation of a cloud with changing volume extinction coefficient k_{ext} in its inside. For this simulation, a synthetic cloud of two concentric spheres with $r_1 = 1$ and $r_2 = 2$ has been created. The volume inside r_1 is called core, the volume between r_1 and r_2 is called shell. In the core, the volume scattering coefficient is twice the value of the shell ($k_{\text{sca},1} = 2\, k_{\text{sca},2}$). As for water clouds in the solar spectral range, k_{sca} is much larger than k_{abs}, so k_{abs} has been set to 0. Figure 2.5 shows a series of such simulations. The top row shows how clouds look like without a background (surface albedo $\alpha = 0$), the second row shows how the impression changes if the cloud is seen in front of a slightly reflecting background ($\alpha = 0.1$). The optical thickness τ_2 describes the optical thickness of the shell, measured radially. As the width of the shell is 1, $\tau_2 = k_{\text{sca},2}$.

The method for the determination of a cloud surface as investigated in this thesis relies on brightness contrasts to detect cloud boundaries. The top row of Fig. 2.5 shows that the cloud core is easily detected at low optical thicknesses of the cloud shell and only barely visible at $\tau_2 \approx 3$ and completely gone at about $\tau_2 \approx 5$. With some surface albedo however, the cloud hides in the background at low optical thicknesses and even it's own shadow can produce larger brightness contrasts as the cloud boundaries produce directly. In summary, if cloud boundary structures are visible, the originate from about $\tau = 0.5 \ldots 2$, measured from outside the cloud. This is where the visible cloud boundary is located. As optical thickness of the cloud is defined by the optical properties of the cloud, which in turn are strongly dependent on the observation wavelength, the visible cloud boundary can be located differently, depending on the spectral region of the instrument. For this reason, in

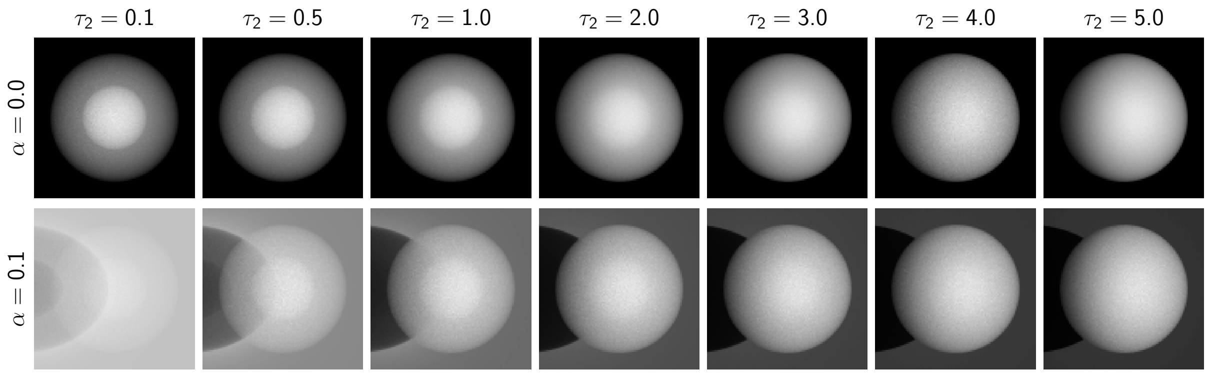

Figure 2.5: Detectability of structures inside a cloud. The images show a spherical cloud consisting of a core with radius 1 and a shell with radius 2. In all cases, the scattering cross section of the core is twice the scattering cross section of the shell. τ_2 denotes the optical thickness from outside the cloud to the boundary of the core. α is the albedo of the surface behind the cloud. The scenes are illuminated from 45° to the right of the observer, as it can be seen by the cloud's shadow on the left. If clouds are observed by a real imager, the exposure time would be adjusted such that the dynamic range is fully utilized. The same is done for these images, which explains that the ground surface in the $\alpha = 0.1$ case seemingly gets darker (in reality, the cloud gets brighter).

.

order to use cloud boundary information to enhance other measurements, it is advisable to use a cloud boundary which has been measured at similar wavelength.

2.2 Geometry

This section covers some basic mathematics as used to express the observation and scene geometries within this work. First, the definitions of points and surfaces are introduced. Following that, computational methods based on these structures are introduced. Finally, some ways to accelerate these computations are shown.

2.2.1 Points

A collection of unstructured data points in space is often called a point cloud. Additional to it's location in space, each point can also carry more information like color, quality indicators, observation direction or estimated surface normals. A typical use case for a point cloud is to represent measured location data which is not yet associated to a connected geometrical structure. Point clouds can for example be obtained using laser scanners or stereographic matching methods. Point clouds can be visualized directly and provide a reasonable impression of the geometrical structure. However, due to the missing structure (i.e. connections between points) it can be difficult to use point cloud data directly in further processing. For example, a viewing ray will most likely not hit any point when traced through a point cloud as each point is infinitesimally small. Surfaces add this missing structure, thus, point clouds are usually only an intermediate step from measurement to surface reconstruction.

2.2.2 Surfaces

A surface describes a two dimensional set of connected points embedded into three dimensional space. There are three common mathematical surface representations: *explicit*, *parametric* and *implicit* (Bronstein et al., 2008). Any of these representations can be used in analytic forms as well as in discretized forms. None of the representations is perfectly suited for every application, so it is valuable to know the advantages and disadvantages of each.

explicit

An explicit surface representation can best be imagined as an elevation map. The elevation or z-level of a surface is given by an explicit formulation:

$$z = f_e(x, y) \tag{2.36}$$

This representation allows to easily compare multiple surfaces (i.e. the upper limit of two surfaces f_e and g_e is simply $\max(f_e, g_e)$). It is also a very natural representation for map data (e.g. surface elevation) or data derived from images. Common meteorological quantities like *cloud top height* or *cloud base height* refer to this concept. A weak spot of this representation is its inability to encode vertical or vertically overlapping surfaces, as for any pair of (x, y) values, only one z value may be present. Holes inside the surface may be defied using a restricted domain on (x, y) values or encoded using a special z-value (i.e. IEEE 754 NaN).

parametric

Defining vertically overlapping surfaces can be achieved by a parametric surface representation. In this case, the surface coordinates are defined by a function $\vec{f_p}$ of two independent variables s and t:

$$\begin{pmatrix} x \\ y \\ z \end{pmatrix} = \vec{f_p}\,(s, t) \tag{2.37}$$

In this representation, it is possible to define for example a sphere ($x = \sin s \cos t; y = \sin s \sin t; z = \cos s$) or a cloud including top, sides and base. A parametric description of a 3D surface can also create a more natural coordinate system on the surface. For the example of the sphere, moving along s and t would correspond to meridional and zonal movement respectively. In computer graphics, this approach is also called uv-mapping.

The major downside of parametric surface descriptions is the difficulty of combining and comparing surfaces. Computing e.g. the intersection or the union of a volume enclosed by a surface will in general require to create a different surface parametrization. For the example of a sphere this quickly becomes evident. As long as one sphere is not fully contained inside the other, it is not possible to describe the intersection of two spheres again as a sphere. Thus the parametrization which has been sufficient for either of the operands becomes insufficient to represent the result. For (the desirable case of) continuous functions $\vec{f_p}$, parametric surfaces are always connected surfaces. As intersections of surfaces can also become disconnected, this states another complication for combining multiple parametric surfaces.

Note that a ray of light, though not a 2D-surface but a 1D half-line, can be represented conveniently in the same manner:

$$\begin{pmatrix} x \\ y \\ z \end{pmatrix} = \vec{o} + t\vec{d} \tag{2.38}$$

with $\vec{o}$ being the ray origin, $\vec{d}$ it's direction and t the traveled distance or time.

implicit

An implicitly defined surface is given as an isosurface of a function of three parameters:

$$f_i(x, y, z) = 0 \tag{2.39}$$

This is also called a *level set*, as it describes the set of all points for which the function produces a certain level (in this case 0). This representation is implicit, as none of the three coordinates x, y, z of points on the surface can be computed directly as a result of some function. In many cases, surfaces describe the boundary of two volumes, one of which is called inside and the other one outside. In these cases, it is customary to use a negative function value for inside regions and a positive function value for outside regions. Furthermore, a common choice is to use the signed distance to the surface as the function value. This way, implicit surfaces conveniently allow to decide if any point in space is inside, on or outside the surface, but opposed to parametric surfaces, it is difficult to generate points which are on the surface. An implicit surface representation allows to describe vertically overlapping surfaces as well as disconnected surfaces. Still, it is very convenient to combine multiple such surfaces. For example, an intersection of two surfaces f_1 and f_2 can be found by $\max(f_1, f_2)$, while the union is given by $\min(f_1, f_2)$. An example is shown in Figure 2.6: two spheres f_1 and f_2 are given by their signed distance functions:

$$\begin{aligned} f'(x,y,z) &= (x-x_c)^2 + (y-y_c)^2 + (z-z_c)^2 - r^2 && (2.40) \\ f(x,y,z) &= \operatorname{sgn}(f')\sqrt{|f'|} && (2.41) \end{aligned}$$

Here, x_c, y_c, z_c denote the center of the sphere and r the radius. sgn is the sign function:

$$\operatorname{sgn}(f) = \begin{cases} +1 & \text{if} f > 0 \\ 0 & \text{if} f = 0 \\ -1 & \text{if} f < 0 \end{cases} \tag{2.42}$$

The function value (top row of Fig. 2.6), for any point, provides the information whether it is inside (< 0, red) or outside (> 0, blue). The bottom row shows the actual surface, which is the 0-isosurface of the function above.

2.2.3 Computation on Surfaces

intersections between surfaces

An interesting combination of parametric and implicit surfaces is the computation of the intersection of two surfaces. The result of the parametric function is precisely the input for the implicit function. Thus combining one parametric and one implicit surface yields an implicit representation for the intersection of both. If for example the xy-plane is given in parametric representation:

$$\vec{f_p}(s,t) = \begin{pmatrix} s \\ t \\ 0 \end{pmatrix} \tag{2.43}$$

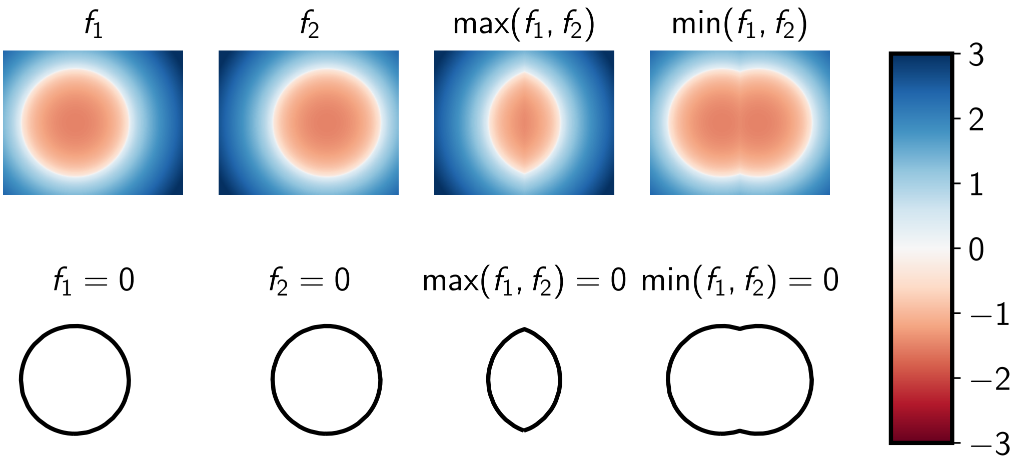

Figure 2.6: These images show a cut through the $z = 0$ plane of two implicitly defined spheres f_1 and f_2 as well as their intersection and union. The top row shows the signed distance function. The bottom row shows the corresponding 0-isosurface.

And the sphere is given by f' from above, the equation for the intersection is immediately given by:

$$0 = f'(\vec{f_p}(s,t)) \tag{2.44}$$

$$0 = (s - x_c)^2 + (t - y_c)^2 + (0 - z_c)^2 - r^2 \tag{2.45}$$

which is an implicit representation for s and t and can be solved. This works equally well for the intersection of a ray and an implicit surface.

conversions between representations

An explicit surface representation f_e is the only representation for which the transformation into the other representations $\vec{f_p}$ and f_i is straight forward:

$$\vec{f_p}(s,t) = \begin{pmatrix} s \\ t \\ f_e(s,t) \end{pmatrix} \tag{2.46}$$

$$f_i(x,y,z) = z - f_e(x,y) \tag{2.47}$$

A conversion into an explicit representation is not possible in general, as the explicit representation can not encode all cases (i.e. vertical overlap) which can be represented using the other representations. Converting from implicit to parametric representation is also not possible in general, as disconnected surfaces are not representable using continuous parametric functions. It is however possible to represent one implicit surface by a set of parametric surfaces. Conversions between parametric and implicit surfaces are more evolved in general and the solutions depend on the specific form of the curves. For polynomial forms, a solution for the transformation in both directions can be found in Sederberg et al. (1984). For typical surface discretizations, specialized conversion methods exists. A common conversion method from a gridded implicit surface to a triangulated (parametric) form is the marching cubes algorithm (Lorensen and Cline, 1987).

discretization

Describing an arbitrary surface using a finite amount of storage requires some form of discretization. As all of the representations are described by functions, the straight forward discretization is to sample the arguments into an equidistant grid and tabulate the function values, leaving a 2D or 3D array respectively. An advantage of this approach is that operations on the surface can be implemented very easily, thus if storage and computation time allows, this is can be the method of choice.

Real world surfaces tend to have areas of high variability and other areas of almost constant or even unknown value. In case of aircraft measurements, due to the aircrafts velocity, the domain is large. There are various flight patters, which are intended to sample a certain measurement volume well, but will in general show large unobserved areas between flight legs. This leaves a large volume of 3D space uncovered by measurements and offers a possibility of reducing data in areas without measurements. This idea can further be extended by reducing the sampling resolution in areas of little data variability. Quite few such optimized discretizations have been developed over time, some of which are outlined as follows, sorted by surface representation:

Explicit surfaces As the typical application of explicit surface representations are maps, geodesy drives the development in this area and digital elevation models (DEM) are a common usage example. In this case, the straight forward discretization is also known as 2D raster map. Which also is the typical form in which satellite based datasets can be obtained. Apart from raster maps, Triangulated Irregular Networks (TIN) (Peucker et al., 1976) are common as well. TINs are based on a flat two-dimensional arrangement of points, which are connected by triangles. These triangles are arranged in a space-filling and non-overlapping way, as it can be provided by the method by Delaunay (1934). The points are then associated with an elevation value. This way, the triangles remain non-overlapping and for every point in the horizontal plane, only one elevation value exists. By arranging the points such that many points are in relevant areas and fewer points are at slowly varying regions, storage requirements can be reduced as compared to raster maps while allowing for a high level of detail where needed. On the other hand, evaluating $f_e(x, y)$ requires to first find the corresponding triangle before the result can be computed. Apart from linear search, this can be accelerated using optimized data structures (Sec. 2.2.4).

Parametric surfaces The parametric surface representation is rarely stored in a straight forward discretized way. More commonly, parametrized analytic formulas are used for selected geometric primitives (e.g. sphere, cylinder, pyramid, plane). An interesting primitive is a triangle which is defined by its three corner points. A TIN can thus be re-interpreted as a collection of many such parametrized triangles forming a triangular surface mesh. Evaluating $\vec{f}_p$ is also not complicated anymore as the parameters s and t can be chosen freely and thus might encode the triangle-id as well as the location on the triangle. For each triangle, the location on the triangle can be expressed by s and t according to Figure 2.7. Due to the limited range of values of s and t between 0 and 1, in principle, the integral part of either of those two variables could encode the triangle-id. In practise it is however often easier to separate the triangle-id into a separate variable.

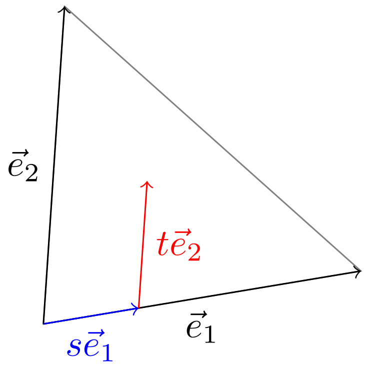

Figure 2.7: Parametric triangle: locations inside a triangle can be expressed using s and t, constrained by $s \geq 0$, $t \geq 0$ and $s + t \leq 1$.

In parametric representation, the requirement of non-overlapping triangles can be lifted to non-intersecting triangles or even to arbitrary triangles, which then allows to define arbitrary shapes which may overlap vertically. While not used in this thesis, Non-uniform rational B-splines (NURBS) are another common parametric surface representation. NURBS are based on b-Splines and as such allow to represent smooth surfaces in a generic way using only a few control points (Piegl and Tiller, 1995).

Implicit surfaces For the implicit representation, it is again important to quickly identify the storage cell for a given location x, y, z. This makes unstructured or irregular meshes less desirable, however a regular grid quickly becomes prohibitively large. As an example, a typical flight pattern during ther NARVAL-II field campaign consisted of a circular flight track with about 100 km radius. For a reasonable flight altitude of 10 km and a grid size of 50 m, this would result in about 3.2×10^9 grid cells. Nonetheless, most of the area is not observed and thus should not require storage space. This is a typical case for an axis aligned tree structure like the classical k-d tree or octree structures (Sec. 2.2.4). Optimizing this problem is still part of current research. A rather new and interesting development is OpenVDB (Museth, 2013), which internally is a fixed-depth tree with large branching factor, allowing for $\mathcal{O}(1)$ random access on average for insertion, reading, and removal. The user facing interface however is close to a regular 3D array interface, which facilitates usage considerably.

2.2.4 Acceleration Structures

The core of any ray tracing algorithm is to quickly calculate the intersection between a ray (i.e. half-line) and the closest primitive surface, which may be a physical surface or the boundary of two volumes with differing physical properties. Despite of very regular structures (e.g. Cartesian grids) which allow to directly compute a small set of candidates for the closest surface, finding the closest surface requires to calculate the intersections between the ray and every surface in order to determine the location of the closest intersection. For a large number of surfaces in the scene, this quickly becomes the largest computational load in a ray tracing algorithm. To overcome this limitation, several *acceleration structures* haven been developed, generally with the goal of reducing the set of candidate surfaces for the closest surface without explicitly computing intersections with the actual surfaces.

A basic building block for such acceleration structures is the idea that if a geometrical structure is fully inside of another structure, a ray can only intersect with the inner structure, if it also intersects with the outer structure. While in general, many outer structures can be used for this purpose, rectangular boxes are a very common choice as intersections between rays and boxes can be computed quickly. This is especially true for axis aligned boxes, which also can be arranged easily in a space-filling manner. This leads to the axis aligned bounding box (AABB). Arranging such boxes in a way which quickly allows to order them along the ray path allows to efficiently prune most of the surfaces and the closest intersection can be found more quickly. This can be achieved by a tree structure of boxes of different sizes which recursively include each other. The two common possibilities for constructing such trees are

- *Bounding Volume Hierarchies*: recursively adding larger bounding boxes around the surfaces, grouping them by adjacency
- *Binary Space Partitioning*: recursively dividing the space into smaller disjoint partitions

Bounding Volume Hierarchies

A bounding volume hierarchy (BVH) is built by recursively grouping primitive elements (e.g. surfaces, volumes) into larger sets of primitives. To allow efficient removal of many primitives from the ray intersection search, this grouping must be done in a way which favours compact group boundaries. Thus closer primitives will be combined first and more distant primitives later. Figure 2.8 shows three primitives which have been grouped into a hierarchy of bounding boxes.

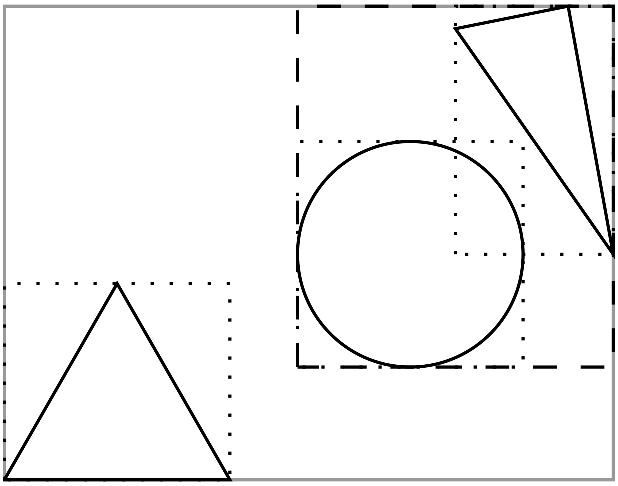

Figure 2.8: Bounding Volume Hierarchy: recursive set of boxes including each other. The resulting boxes may overlap but any primitive geometry is only part of one leaf box. There are no empty boxes.

An advantage of bounding volume hierarchies is that each primitive is only contained in a single leaf node. As a consequence, the total amount of memory required to store a BVH is limited. Also, the construction of a BVH tends to be quicker than the construction of a BSP (Pharr et al., 2017). On the other hand, the same volume may be included in multiple leafs of the tree.

Binary Space Partitioning

Binary space partitioning (BSP) approaches the problem the other way around. The tree is not constructed by recursively grouping primitives into larger sets, but by dividing the whole space recursively into smaller, disjoint regions (Fig. 2.9). This way, each volume has to be checked only once, but as primitives may end up in multiple volumes, each primitive may be checked multiple times for intersections. The fact that primitives can be included in many (in principle unbounded) leaf nodes also leads to a theoretically unbounded amount of memory consumption. As it is possible to stop the tree generation at any level (potentially creating a less optimal tree), memory consumption can be limited in practice.

A typical example of a BSP is a k-d tree, which is build by recursively splitting the space into two subspaces along an (n-1) dimensional axis aligned subspace (n being the dimensionality of the space). In three dimensional space, this corresponds to splitting

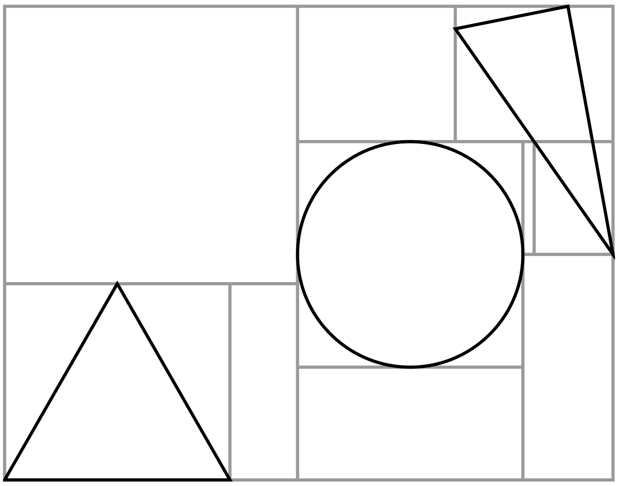

Figure 2.9: Binary Space Partitioning, in this case a k-d tree: space is subdivided into disjoint regions. There are no overlapping boxes but primitive geometries can be part of multiple leaf nodes. Boxes may also become empty.

along an axis aligned plane. The axes to which the split is aligned can be changed for each split. Depending on the intended use of the tree, the optimal choice of the splits may be different, so many different strategies to build such a tree have evolved. In this work, k-d trees are used both, to accelerate ray-tracing and to accelerate nearest neighbor point look-ups.

For the point look-ups, the *cKDTree* from *scipy* is used, which builds the tree based on the *sliding-midpoint* rule (Maneewongvatana and Mount, 1999). The idea is that for nearest neighbor look ups, cells should be compact, so splitting is always done across the center of the longest dimension. However, if any volume is empty, the size of that empty volume is increased as much as possible.

For ray intersection tests, the surface area heuristic (SAH) delivers better results (MacDonald and Booth, 1990). The idea is to optimize a probabilistic cost function C which estimates the cost of tracing a ray through a volume which has been split into two sub volumes A and B:

$$C = c_{\text{trav}} + p_A \sum_{i=1}^{N_A} c_{\text{int}}(a_i) + p_B \sum_{i=1}^{N_B} c_{\text{int}}(b_i) \tag{2.48}$$

With c_{trav} being the computational cost of traversing on tree level, c_{int} the cost of computing the intersection with one primitive (a_i or b_i) and p_A and p_B the probability of hitting the sub volume A or B after the total volume was hit by a ray. MacDonald and Booth (1990) show that a good estimate for p_A and p_B is the ratio of the surface area of the sub volume to the surface area of the total volume. c_{trav} and c_{int} can be optimized by empirically to match the properties of the algorithm implementation. If the primitive surfaces are all of the same kind, it is usually sufficient to provide only one constant c_{int} for all primitives. As useful splits are only at the edges of any primitive surface along each dimension, the potential splits can be enumerated and the cost function can be computed for every potential split. According to Pharr et al. (2017), k-d-trees tend to have longer build times, but produce slightly faster ray intersection tests than what is possible with BVHs.

Chapter 3

Methods

3.1 Radiative Transfer Calculations

Within this work, several different methods for radiative transfer calculation have been used. The basis is provided by the libRadtran software package, which contains a large variety of radiative transfer solvers as well as a collection of cloud optical properties. For some specialized calculations, a custom radiative transfer solver (RayLi) has been built.

3.1.1 Library for Radiative Transfer – libRadtran

Most of the radiative transfer simulations have been done using the libRadtran library for radiative transfer (Mayer and Kylling, 2005; Emde et al., 2016). The package contains several solvers for the radiative transfer equation. Additionally, it contains a series of parameterizations for the optical properties of the atmospheric constituents, which are required as input for any radiative transfer calculation. From libRadtran, this work uses the DISORT solver for 1D radiative transfer and MYSTIC for 3D radiative transfer as well as scattering phase functions computed with the *mie* tool.

1D radiative transfer – DISORT

The DIScrete ORdinate Radiative Transfer method is a deterministic solution to the radiative transfer equation in one dimensional geometry, able to compute radiance, irradiance and actinic flux. The method has been developed by Chandrasekhar (1960) and Stamnes et al. (1988). In this work, the DISORT method is used to compute look-up tables for the retrieval of r_{eff} and LWC from pairs of measured radiance values. The implementation used for this work is by Buras et al. (2011) and contained in libRadtran.

3D radiative transfer – MYSTIC

MYSTIC is the fully three-dimensional Monte Carlo code for the physically correct tracing of photons in cloudy atmospheres (Mayer, 2009). It is a well tested radiative transfer solver with a large set of features. MYSTIC can either operate in Cartesian or spherical mode with circular boundary conditions. The model allows to define arbitrary clouds on a grid which is equidistant in the horizontal plane and allows variables spacing along the vertical axis. Clouds defined this way can be integrated into a scene with background atmosphere and planetary surface. In this work, MYSTIC is used to calculate a series of artificial cloud scenes to study the applicability of dual wavelength cloud microphysical retrieval methods in the presence of 3D cloud structures. The scenes have been computed using the Variance Reduction "Optimal Options" Method (VROOM) enabled within MYSTIC (Buras and Mayer, 2011).

3.1.2 Composable Radiative Transfer – RayLi

RayLi is a framework for the computation of ray based light transport which has been developed as a side project to this thesis. RayLi is neither a full featured software for radiative transfer in the atmosphere, nor a single program which provides a radiative transfer solution for a given input file. In stead, it is a set of composable parts, which can be combined into a problem specific radiative transfer solver by the user. A key design idea is to strongly separate the definitions of problem geometry from the solver of the radiative transfer equation as well as the generation of optical properties.

RayLi has also been used to generate synthetic test cases for the investigated cloud property retrieval. Here, the possibility to define arbitrary grid shapes without influencing the solver allows to directly define non-rectangular cloud surfaces, sidestepping the need of an accurate discretization into rectangular volumes. On the retrieval side, RayLi is used to compute cloud surface location, orientation and geometric shadow masks for the spectral cameras from triangulated surfaces.

Tracing on arbitrary irregular grids

Independent of the implementation of the interaction between radiance and atmosphere, the ray-tracing approach requires a specific pattern of accessing the data describing the atmosphere. Starting at an arbitrary point, all atmospheric properties along a half-line pointing into an arbitrary direction must be fetched until some condition terminates the walk along the line. If volume properties are defined homogeneously within bounded regions, this can be interpreted as a *gird* of atmospheric properties. Independent of the dimensionality and organization of the atmospheric grid, the result of this walk is a one-dimensional listing consisting of a series of volume-like and surface-like elements. Figure 3.1 shows this behaviour exemplarily for a ray passing a cuboidal and a triangular grid. Passed volume elements are indicated by colors while surface elements are the black lines. The lower row shows the same setup, but from the perspective of the ray passing through the volume. Independent of the shape of the grid, the ray only sees a sequence of volume and surface properties. Apart from an *id*, which can be used later to obtain optical properties, the volume elements additionally carry information about the geometrical distance which the ray passed in the specific volume. The surface elements carry an *id* and information about the surface orientation and curvature instead.

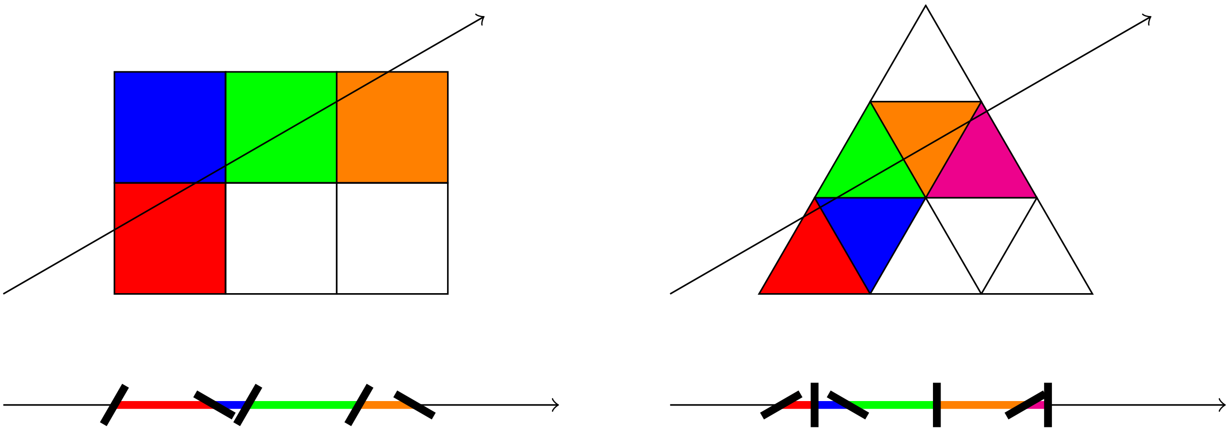

Figure 3.1: Ray tracing on arbitrary grids. Independent of the shape of a grid, tracing a ray through it will always yield a sequence of volume-like and surface-like elements.

This observation allows to define a generic interface between grid and radiative transfer solver. The interface consists of the WALK($ray.\vec{o}, ray.\vec{d}$) method, which any grid must implement. Conceptually, this method returns the aforementioned sequence of volume and surface elements (subsequently called a *path*), starting from the ray origin $\vec{o}$ into its direction $\vec{d}$. In fact, this path is not implemented as a list or array, but as a generator in stead, which efficiently allows to abort the computation of the sequence early in case the light is scattered out of the current path.

The use of this interface in a radiative transfer solver which is based on ray tracing is illustrated in Alg. 1. The WALK method must know how the grid is organized internally and thus must be implemented for each grid individually. Otherwise the algorithm can perform ray-tracing on arbitrarily organized atmospheric data, without a change in the code. In particular, the PROCESSVOLUME and PROCESSSURFACE methods can act locally, needing only information about the volume or surface element s they act on. To obtain microphysical properties of the element s, the user must provide two functions, one for volumes and another for surfaces, which compute microphysical properties from the volume or surface *id* respectively. This function can either be an array-lookup for tabulated microphysical properties, or an actual function which computes the properties on the fly. The latter is especially useful either if the computed optical properties would use to much memory to store, or if the optical properties should be computed from the result of

Algorithm 1 Ray walking

```
$grid \leftarrow$ geometry of atmospheric properties
$ray.\vec{o} \leftarrow$ origin
$ray.\vec{d} \leftarrow$ initial direction
while $ray$ is alive do
    for $s \leftarrow grid.\textsc{Walk}(ray.\vec{o}, ray.\vec{d})$ do
        if $s$ is volume then
            ProcessVolume($s$)
        else if $s$ is surface then
            ProcessSurface($s$)
        end if
        if change direction then
            $ray.\vec{o} \leftarrow$ new origin
            $ray.\vec{d} \leftarrow$ new direction
            break
        end if
    end for
end while
```

other lookup functions, because different atmospheric constituents are mixed.

This separation of grid structure and implementation of physical processes allows to adjust the data grid to the problem at hand. In this thesis, the effect of cloud surface orientation on radiative transfer is investigated. In order to represent tilted or curved surfaces at arbitrary precision, the grid on which the data is defined must be able to adapt to the surface orientation. Otherwise, it is difficult to distinguish between true effects of surface orientation and false effects of unresolved structure.

Up to now, a small series of grids have been implemented and used within this work. The implemented grids may be split into *physical grids*, which represent actual geometry and *grid wrappers*, which use existing grids and combine or modify them for added functionality.

physical grids

Physical grids are defined in terms of specific geometric shapes. The shapes may be of infinite size in one or more dimensions. Currently implemented examples of these include the spherical grid, the Cartesian grid, the convex polyhedral grid and the triangular surface grid. The spherical grid is a collection of concentric spheres (see Fig. 2.5) for an example). The grid is more of theoretical concern, but allows to compute spherical clouds very efficiently. The Cartesian grid is a collection of axis aligned cuboids in a dense regular pattern. This grid is very useful, as model output often comes in this form and tracing a ray through such a regular pattern can be implemented very efficiently.

The convex polyhedral grid is a convenient generalization of the Cartesian grid. Instead of a regular collection of cuboids, it contains an irregular collection of convex polyhedra. Convex polyhedra, which are just the 3D version of convex polytopes, are a compact convex set of points with a finite number of extreme points (i.e. the corners) (Grünbaum, 2003). Convex polyhedra can be represented as the intersection of half spaces, i.e. a plane with designated sides for what is inside and what is outside. As a convex set, a polyhedron contains every point which is between two arbitrary points of the set. As a consequence, the intersection of a ray and the boundary of a convex polyhedron can be computed very easily by the intersection of the ray with a set of planes defining the half spaces. The first intersection point is the furthest intersection with a plane crossed from outside to inside and the second intersection point is the closest intersection with a plane crossed from inside to outside. If the first intersection point is further than the second, the polyhedron is missed. For the implementation of the $\textsc{Walk}(ray.\vec{o}, ray.\vec{d})$ method, it is necessary to quickly find the polyhedron which is intersected first. This can be accomplished by using an acceleration structure, in this case a k-d tree has been used (Sec. 2.2.4).

The triangular surface grid represents a triangulated surface mesh and contains no volume elements. While computing the intersection of a ray and a triangle seems simple, care must be taken that numerical inaccuracies of floating point numbers don't lead to holes in the surface mesh. To prevent such unintended holes, the method by Woop et al. (2013) is used. Computing the intersection with the closes triangle is again accelerated by the use of a k-d tree.

grid wrappers

Grid wrappers are grids which use one or more other grid as a basis to create a new grid. Currently, the *cyclic grid* and the *add grid* fall into this category. The cyclic grid can be used to define cyclic boundary conditions in one or more dimensions over another grid, by defining a bounding box around the inner grid, which is repeated along its finite-sized dimensions. The add grid is used to combine two other grids into one. An example of this method is shown in Figure 1.2. As the only thing a grid must provide is the $\textsc{Walk}(ray.\vec{o}, ray.\vec{d})$ method, this can be accomplished by taking the two paths returned by the two inner grids and join them together into a new path. This merge merge may involve splitting volume elements of one grid at the location of surface elements of the other grid. Furthermore, the surface and volume ids of the inner grids may refer to different microphysical properties and need to be transformed into a new, common id-space. This is accomplished by user defined functions.

combining atmospheric constituents

For radiative transfer calculations, it is convenient to only consider volumes with a single set of homogeneously distributed optical properties. In reality, any atmospheric volume consists of many different kinds of scatterers and absorbers. Some examples would be molecules, aerosols and cloud particles. There can also be different kinds of each of these. As introduced in Sec. 2.1.3, the optical properties of a small atmospheric volume can be obtained from its constituents by integrating or summing over the different parts. Furthermore, all of $k_{\text{abs}}, k_{\text{sca}}, \mathcal{P}$ are linear in the number of constituents of the same type. This allows to interpret the optical properties (i.e. the combination of $k_{\text{abs}}, k_{\text{sca}}, \mathcal{P}$) as a mathematical vector with according definitions of vector addition and scalar multiplication with a real number. Accordingly the combination of two sets of optical properties is simply their addition and the amount of scattering material can be scaled by scalar multiplication. This is especially useful in combination with the *add grid*, as it allows to define a background atmosphere on a different grid than for example a cloud without the need to interpolate optical properties to a common grid in advance.

3.2 Instrument Development and Field Campaigns

In order to actually derive cloud geometry and microphysical properties from passive remote sensing, a suitable measurement system is required. The ideal measurement geometry for bi-spectral retrieval methods of cloud microphysical properties and for the reconstruction of cloud boundary surfaces is to have the visible cloud surface directly illuminated by the sun. This geometry can be achieved by operating the sensors on an aircraft, looking downwards. An additional benefit of this setup is that large cloudy areas can be observed in a relatively short period of time. As part of this thesis, the previously existing specMACS hyperspectral imaging system (Ewald et al., 2016) has been integrated into the High Altitude and Long Range Research Aircraft HALO (Krautstrunk and Giez, 2012) for the operation in nadir perspective as part of HALO's cloud observatory configuration (Stevens et al., 2019). The development of the adapted setup includes the addition of 2D imaging cameras, a robust casing including environmental control system and improved automation of the whole measurement process. The setup has been operated on a series of field campaigns and has been incrementally improved in between.

3.2.1 Hyperspectral Imaging System specMACS

Previous Work

The hyperspectral imaging system specMACS has been established at the LMU Munich in 2012. The basis of the specMACS system is formed by two hyperspectral cameras: a SPECIM SP-PFD-CL-65-V10E for the visible and near-infrared range (VNIR, 400 nm to 1000 nm) and a SPECIM SP-SWIR-LVDS-100-N25E for the short-wave infrared range (SWIR, 1000 nm to 2500 nm). The cameras operate as line cameras in a push broom fashion, which allows to use a grating (G in Fig. 3.2) to spread the spectrum of each line pixel across the second dimension of a CMOS sensor and thereby record the full spectrum for each observed pixel. The combined spectral range of 400 nm to 2500 nm covers most of the solar spectral range and allows to experiment with a variety of passive remote sensing methods. In the beginning, the specMACS system has been used as a ground based remote sensing system on the roof of the meteorological institute (Fig. 3.3) as well as in several field campaigns. During this period, initial shortcomings of the system have been identified and subsequently addressed by partial hardware replacement, full software replacement and a thorough system characterization by Kölling (2015) and Ewald et al. (2016).

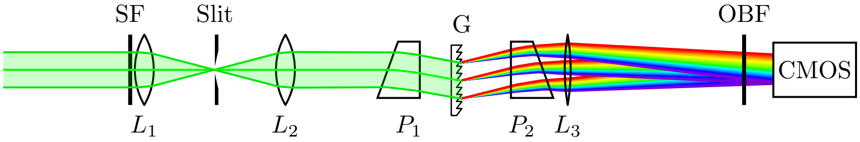

Figure 3.2: Optical system of the specMACS spectral imagers (Ewald et al., 2016)

Figure 3.3: specMACS VNIR and SWIR sensors on the roof of the meteorological institute in Munich (Ewald et al., 2016)

After upgrading the system, it was adapted to participate in its first airborne field campaign ACRIDICON-CHUVA, taking part in 2014 in Manaus, Amazonia, Brazil (see Section 3.2.2 for more information about field campaigns). As part of a mixed remote-sensing and in-situ instrumentation, specMACS was placed inside the aircraft cabin, observing vertical cloud structure through a side-window (Ewald et al., 2016; Ewald, 2016; Zinner et al., 2019). Additional to spectral measurements from the two hyperspectral line cameras, first experiments leading to the stereographic method presented in this thesis have been performed using a GoPro camera which was mounted behind a window, observing clouds in parallel with specMACS (Schwarz, 2016; Jäkel et al., 2017).

specMACS in Nadir Perspective

In order to advance the airborne cloud observatory configuration of the HALO research aircraft, specMACS was integrated in downward-looking perspective (Stevens et al., 2019). This way, a hyperspectral imager complemented the remote sensing payload which already consisted of HAMP – Halo Microwave Package (Mech et al., 2014), WALES – WAter-vapour Lidar Experiment in Space (Wirth et al., 2009), SMART albedometer (Wendisch et al., 2001, 2016) and an AVAPS dropsonde system.

During the previous field campaign (ACRIDICON-CHUVA), the GoPro camera provided valuable visual information about the surroundings of the measurement area. Furthermore, its data has been used for first stereographic distance measurements (Schwarz, 2016; Jäkel et al., 2017). Within these studies, also some insufficiencies of that solution became evident: the clock of the camera can not be automatically synchronized to the aircraft time. Recorded video data only stores one time stamp and the intended image frequency. Data is compressed using lossy compression which hides details important to quantitative analysis. The built in automatic image stabilization hides movements which are captured by the aircraft's basic data acquisition system. Exposure time is not recorded continuously.

Resulting from this experience, an industrial camera has been added to this specMACS configuration. The camera is a Basler acA2040-180kc camera with Kowa LM8HC objective, which captures 2000 px × 2000 px RGB images at 1 Hz. Next to providing images of the surroundings of the measurement region, this setup provides well defined data for automatic stereographic distance estimation.

For this deployment, specMACS had to be installed in the rear end of the aircraft fuselage, in the so-called "boiler room", outside of the pressurized cabin. In order to protect the sensors and to ensure stable measurement conditions, a pressurized, temperature stabilized, and humidity controlled enclosure has been developed together with enviscope GmbH (Fig. 3.4).

specMACS Power Supply

The specMACS boiler room assembly is powered through two independent power buses:

- essential bus: powered from 115 V three-phase AC current, converted via a Transformer Rectifier Unit (TRU) to 28 V DC
- measurement bus: 28 V DC, directly from aircraft mission power

The essential bus powers temperature control, Ethernet switch and the specMACS Life Support system (SLS), which are the minimal set of components to be operational such that the specMACS system stays within the safe operating conditions of the sensors and the state of the system can be monitored by the operator in the cabin or, via the aircraft

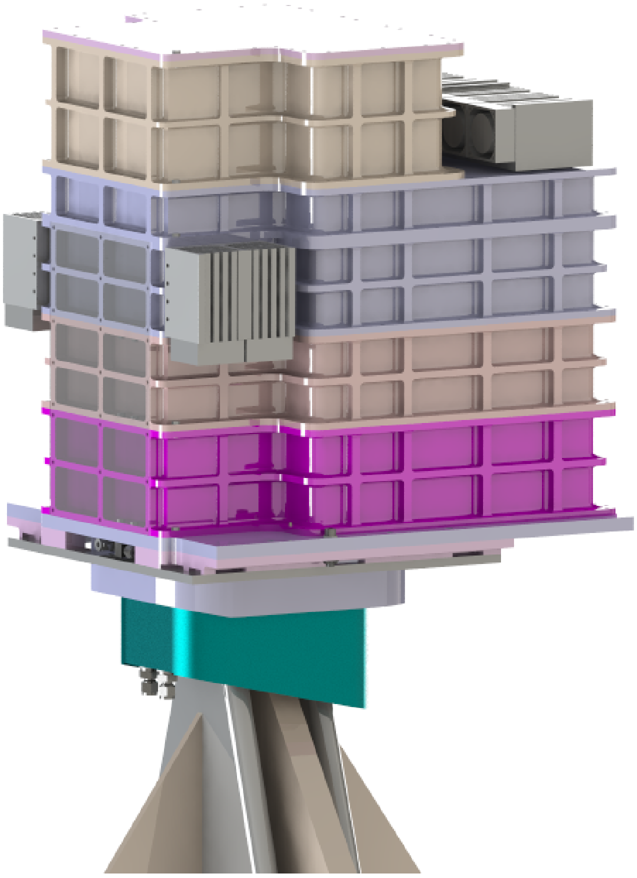

Figure 3.4: Rendering of specMACS enclosure in boiler room. Image: enviscope GmbH

satellite communication link, on ground. The measurement bus provides additional power, which is required to perform the actual measurements. The measurement bus power is distributed via the SLS, which allows to switch different parts of the measurement system on and off separately.

specMACS Life Support Controller (SLS)

Due to the sealed installation in the boiler room, no manual access to the system components is possible after the integration into the aircraft. To keep the system in an appropriate temperature and pressure range and to be able to power-cycle the system components independently, it is still necessary to provide access to some electrical switches and to communicate with the temperature controllers. Complicating this requirement, only an Ethernet connection is available between cabin and boiler room, which has to accommodate for all information exchange. It was decided to build the specMACS live support system (SLS) as a single micro controller based circuit board (Fig. 3.5). The SLS features

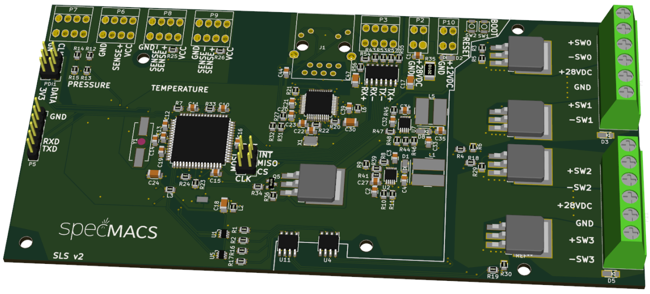

Figure 3.5: specMACS Life Support Controller

the following hardware interfaces:

- Two analog inputs for pressure sensors (absolute ambient pressure in compartment and relative pressure in a nitrogen bottle, which can be used to refill the compartment in case of small leakages)
- Two analog inputs for temperature sensors
- One digital output for a magnetic valve, connected to the nitrogen bottle
- Four high power switch outputs (with galvanic separation) for fans, computer, VNIR and SWIR, operating on the measurement bus
- One RS-422 interface for communication with temperature controllers
- One Ethernet interface for communication to the aircraft cabin
- Wide-range 6 V to 34 V DC power input

The SLS operates on a minimal software stack without operating system and is powered from the essential bus. This way, the system remains controllable independently of the measurement computer and by switching off the measurement bus, only minimal power is consumed inside the compartment, easing thermal management in case of trouble. The SLS is controlled via an HTTP REST interface and optionally by a JavaScript based web fronted. The implementation of such a control interface is relatively simple and is compatible with all current computer operating systems. This way, an operator can use the SLS without installing further software on his or her computer, which increases flexibility during field campaigns. Apart from providing remote control and monitoring to the operator, the SLS is also responsible for controlling the compartment pressure, by re-pressurizing the compartment from an auxiliary nitrogen bottle in case of pressure loss. This is done automatically, without operator intervention.

Thermal Management

During the campaign operation, the specMACS system is exposed to a wide external temperature range. The specMACS VNIR and SWIR sensors are specified for storage temperatures from −20 °C to 50 °C and operation temperatures from 5 °C to 40 °C. At the Grantley Adams International Airport in Barbados, where the operation base of the NARVAL-II field campaign was located, surface temperatures frequently could reach 30 °C and above, while air temperature at the maximum operating altitude of HALO could drop down to −80 °C. At the airport, no hangar space was available for HALO, so the aircraft frequently was placed outside and in direct sunlight, which raises inside temperatures well above the outside air temperature. In these conditions, the cameras could easily be outside their safe operating range. Furthermore, a relatively constant temperature is desirable during measurement periods in order to ensure a consistent dataset (mainly because of the temperature dependence of the SWIR sensor, see Ewald et al. (2016) for details).

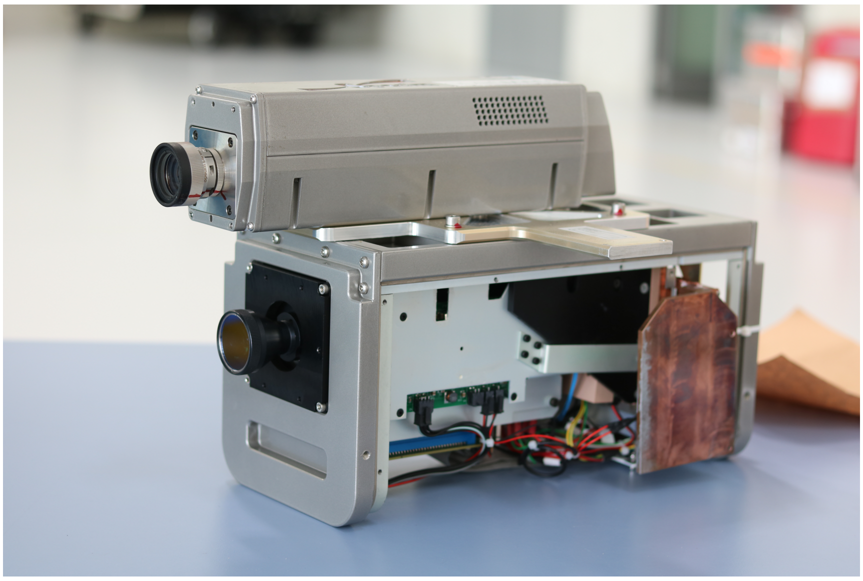

Figure 3.6: specMACS VNIR and SWIR sensors before integration into the boiler room compartment. The SWIR sensor has been equipped with solid copper plates (on both sides of the sensor), which provide thermal connection to the compartment hull.

To reduce thermal noise in the SWIR, its sensor is kept at a temperature of 200 K by a stack of five differently sized Thermo Electric Coolers (TEC). While being able to provide the necessary high temperature gradient in the order of 100 K, these devices produce up to 200 W of additional heat emission inside the camera housing (Fig. 3.6, lower camera). In order to be able to remove the heat from the specMACS compartment (Fig. 3.4) in a controlled and effective manner, the SWIR camera is directly connected to the compartment hull via a solid copper connection. Outside of the hull, these connections head into an ETC-288-14-06-E TEC element each. These elements are connected to a heat sink and provide a maximum cooling power of 340 W each, which can be transfered out of or into the compartment. Two additional such TEC elements are placed on top of the compartment with heat sinks attached inside and outside, to regulate the air temperature of the compartment directly. Each of these four TEC elements is driven and controlled by a head electronics TEC16-24 High Power TEC Driver, which are in turn controlled by the SLS via its RS-422 interface.

Humidity Control and Anti-Frosting

Due to the wide temperature range faced by the instrument, humidity must also be properly controlled. To keep the compartment approximately at surface level pressure during the whole flight, it is sealed airtight. Accordingly, the amount of water inside the compartment stays fixed during the flight. In the flight preparation phase, the compartment can be flushed with nitrogen in order to dry the compartment. This however is limited to about 5 % to 10 % of relative humidity to protect the inside electronics: at low values of relative humidity, less static electricity is removed by leakage currents and more charge can accumulate resulting in potentially harmful electrostatic discharge (Trost, 1995). During one flight (NARVAL-II RF06 on 19 Aug 2016), the data acquisition computer occasionally became unresponsive, which most likely can be attributed to the low humidity inside the compartment. On that particular day, nitrogen flushing during flight preparation had been done most thoroughly, thus, the compartment had been dried to the lowest values of all flights.

WMO (2017, Annex 4.B) recommends formulas for the calculation of the saturation vapor pressure of water and ice. In an airtight and temperature stabilized system, the partial pressure of water vapour stays constant. For a given initial compartment humidity and temperature, this allows to calculate the temperature at which icing will happen. For a worst case assumption of 10 % relative humidity at 30 °C when closing compartment at ground level, the inner window surface must be kept above −4 °C to prevent icing. If the compartment would be closed at 5 % relative humidity and 20 °C, this number gets lowered to −18 °C. At outside temperatures down to −70 °C, which is common for tropical flight legs, this requires a constant heating of the inner window surface. As these temperatures could not be sustained for high flight altitudes during NARVAL-II, two additional *EBM Pabst 8414 N* axial fans, each delivering up to 69 $\frac{\mathrm{m}^3}{\mathrm{h}}$ air flow have been installed prior to the NAWDEX field campaign. The forced airflow onto the window surface increases the heat flow into the window and thereby raises the temperature at the internal window surface to a level which prevents icing.

Redundant Data Storage

Due to the airtight construction of the instrument compartment, and the concept of drying the inside atmosphere by flushing with nitrogen, it is not feasible to open the compartment after each flight for data download. In order to retrieve the captured data quickly after each flight, a secondary computer had to be installed inside the cabin (Fig. 3.7), which is connected to the boiler room compartment via 10 $\frac{\text{Gbit}}{\text{s}}$ fiber Ethernet. Inside the cabin unit, four removable bays for solid state disks are installed. Data is written onto the removable solid state disks during flight, such that data ”download” is possible within seconds after landing, simply by removing the disks, irrespective of the amount of data captured during the flight.

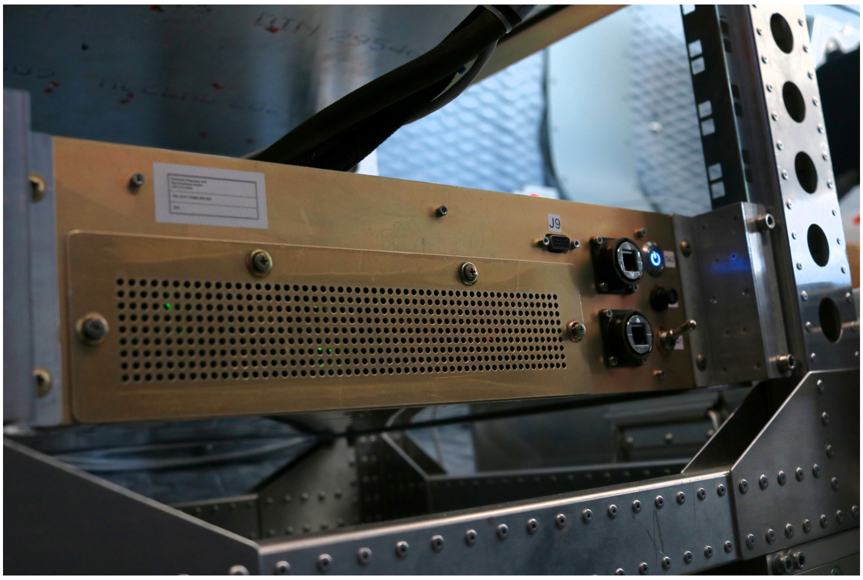

Figure 3.7: specMACS storage system in cabin. The front panel features from right to left: power switches and circuit breaker for the storage system, one Ethernet port to connect directly to the boiler room computer or the cabin computer respectively, one VGA connector for connecting a monitor for debugging and a metal plate which can be removed by four screws to reveal four bays for removable solid state drives and two USB ports.

Polarization Upgrade

For the EUREC^{4}A field campaign, which will take place in 2020, the 2D RGB camera has been replaced by two polarization resolving LUCID Vision Phoenix 5.0 MP cameras (Fig. 3.8). The primary objective of this upgrade is to provide a simultaneous measurement of four polarization directions in addition to RGB colors, which will allow accurate measurements of cloud droplet size (Mayer et al., 2004; Weber, 2019; Pörtge, 2019). During this upgrade, the exposure control of the camera system has been revisited and improved, which substantially improved 3D cloud geometry retrieval quality, as has been verified during the EUREC^{4}A test flights in May 2019.

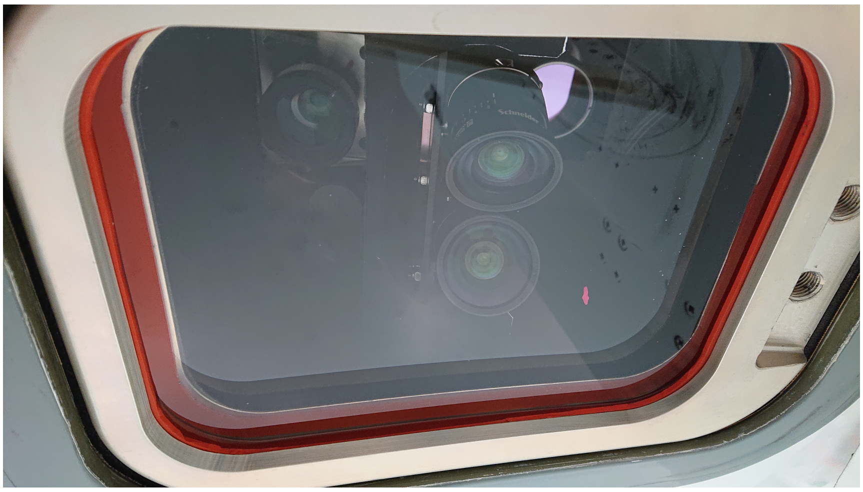

Figure 3.8: The four specMACS lenses in EUREC^{4}A configuration. The foreground shows the two tilted lenses of the polarization resolving cameras, in the background the VNIR and SWIR sensors are visible.

3.2.2 Field Campaigns

The specMACS system has been and will be deployed to several airborne field campaigns on board the HALO aircraft. The following section gives a short overview about the field campaigns and relevant for this thesis.

ACRIDICON-CHUVA

The ACRIDICON-CHUVA field campaign took place in September 2014 and was based in Manaus, Amazonia, Brazil (Wendisch et al., 2016). The goal of the field campaign was to study the influence of anthropogenic aerosols on the cloud life cycle and precipitation formation processes. Cloud droplet formation and growth is dependent on the availability of cloud condensation nuclei (CCN) which can be generated from anthropogenic sources like industry or forest fires. Next to the suite of in-situ sensors for atmospheric chemistry, the VNIR and SWIR sensors of specMACS have been installed looking sideways (Ewald et al., 2016). The specMACS instrument has been used to derive height dependence of cloud thermodynamic phase and droplet size (Jäkel et al., 2017; Ewald et al., 2019). ACRIDICON-CHUVA has been the first airborne field campaign for the specMACS instrument system and a 2D imaging system was not yet part of the specMACS system. For the field campaign, a GoPro camera (type: Hero HD3+3660-023 Full-HD) has been installed observing the same area as the spectral cameras. Jäkel et al. (2017) used images from this camera to manually derive cloud surface locations in order to derive vertical profiles of cloud thermodynamic phase. Schwarz (2016) did some first work towards automating the process of deriving cloud surface locations.

NARVAL-II

The Next-Generation Aircraft Remote Sensing for Validation (NARVAL) field campaigns aimed at establishing the HALO aircraft as an airborne cloud observatory (Stevens et al., 2019). The specMACS instrument was part of the NARVAL-II field campaign, which took place in August 2016 and was based in Barbados. As a cloud observatory, used for validation studies, the goal was to capture cloud structure, cloud development and the surrounding environment in order to generate test cases to validate climate models. While NARVAL-II has been to a large extent instrument and method driven, the upcoming EUREC^{4}A field campaign (see below) will focus more on the scientific part. The NARVAL-II field campaign marks an important upgrade for the specMACS instrument system: it was modified to look downwards in accordance to the accompanying remote sensing payload. Within this modification, a 2D imager became permanent part of the specMACS system. This imager has been used for the development of the stereographic cloud surface retrieval as described in this work and in Kölling et al. (2019).

NAWDEX

Numerical weather prediction was revolutionized in recent years with the introduction of ensemble prediction systems, capable of computing forecasting uncertainty (Bauer et al., 2015). Still, short-term prediction of high-impact weather presents challenges to current forecasting systems and the lack of understanding in the role of diabatic processes has been identified as an important part of this challenge. The purpose of the North Atlantic Waveguide and Downstream Impact Experiment (NAWDEX) field campaign was to investigate the importance of such diabatic processes for midlatitude weather (Schäfler et al., 2018). The experiment followed two weeks after NARVAL-II during September and October 2016 and was based in Iceland. During the campaign operations, observations over the North Atlantic have been conducted using multiple aircraft and ground-based stations. HALO has been part of the aircraft observations and was again configured as cloud observatory. Due to the close timing between the two studies, apart from small instrument repairs, the payload of HALO has not been changed between NARVAL-II and NAWDEX. However, for specMACS two fans have been been added which effectively protected the window from icing (Sec. 3.2.1). With the focus on larger cloud formations, data derived during this campaign also yields valuable information for the validation of the stereographic cloud surface retrieval described in this work.

EUREC^{4}A

The Elucidating the role of clouds-circulation coupling in climate (EUREC^{4}A) field campaign will take place in January to February 2020 in the Atlantic ocean east of Barbados (Bony et al., 2017). The study is in support of the World Climate Research Programme's Grand Science Challenge on Clouds, Circulation and Climate Sensitivity and accordingly aims at advancing the understanding of the interplay between clouds, convection and circulation and their role in climate change. Barbados offers a perfect operation base, as it is the first landmass the airmass will encounter after a long undisturbed travel across the Atlantic. Since Barbados is located in the tropics, and the tropics cover half of the Earth's surface, the kinds of clouds observable in this area are the most common clouds across the globe. EUREC^{4}A is a follow up of the NARVAL-II campaign but has grown considerably. The HALO aircraft will be accompanied by a still growing set of aircraft and ship, which will provide a unique setting for the further development and verification of the methods described in this thesis. Relevant for this work is the HALO EUREC^{4}A pretest campaign, which took place in May 2019 based in Oberpfaffenhofen. During this period, the upgraded specMACS payload using polarization resolving cameras had its first chance to fly. The improved data quality obtained from the new camera system already shows important quality improvements for the stereo retrieval method presented in this thesis.

3.3 Observation Geometry

The specMACS imaging system consists of multiple separate cameras as introduced in Section 3.2.1 and is operated on a fast moving aircraft. The stereographic cloud surface reconstruction, which will be introduced in Section 3.4, relies on precise measurements of observation angles and location. This requires to properly account for camera intrinsics including projection and lens distortion, as well as inter-camera alignment and aircraft motion. The characterization of the spectral cameras VNIR and SWIR, which is required to transfer the retrieved cloud surface geometry to microphysical retrievals can be found in Ewald et al. (2016). The characterization of the intrinsics of the 2D imagers, the relation between multiple cameras and the motion of a camera between different time steps is shown below.

3.3.1 Geometric Camera Calibration

This section contains work which has already been published in Atmospheric Measurement Techniques (AMT) by Kölling et al. (2019).

As the distance between aircraft and observed clouds is typically much larger than the flight distance between two images, the 3D reconstruction method relies on precise measurements of camera viewing angles. The observed clouds should not move or change too much between subsequent captured images, thus frame rates of about 1 Hz are required. At that frame rate, a change in distance between cloud and aircraft of 100 m at a distance of 10 km results in approximately 0.01° difference of the relative viewing angle or about 1/3 px. Consequently, achieving accuracies in the order of 100 m or below requires both, to average over many measurements in order to get sub-pixel accuracy and to remove any systematic error in the geometric calibration to less than 1/3 px. This is only possible if distortions in the cameras optical path are quantified and corrected.

Camera Model

The camera model uses methods provided by the OpenCV library (Bradski, 2000), the notation is chosen accordingly. Geometric camera calibration is done by defining a parameterized model which describes how points in world coordinates are projected onto the image plane including all distortions along the optical path. Generally, such a model includes extrinsic parameters which describe the location and rotation of the camera in world space and intrinsic parameters which describe processes inside the camera's optical path. Extrinsic parameters can differ between each captured image while intrinsic parameters are constant as long as the optical path of the camera is not modified. After evaluation of various options for the camera model, we decided to use the following:

$$\begin{pmatrix} x \\ y \\ z \end{pmatrix} = R \begin{pmatrix} X \\ Y \\ Z \end{pmatrix} + \vec{t} \tag{3.1}$$

$$x' = x/z \tag{3.2}$$

$$y' = y/z \tag{3.3}$$

Where X, Y, Z are the world coordinates of the observed object, R and $\vec{t}$ the rotation and translation from world coordinates in camera centric coordinates and x, y, z are the object location in camera coordinates. x' and y' are the projection of the object points onto a plane at unit distance in front of the camera. The distortion induced by the lenses and the window in front of the camera is accounted for by adjusting x' and y' to x'' and y'':

$$r^2 = x'^2 + y'^2 \tag{3.4}$$

$$x'' = x'(1 + k_1 r^2 + k_2 r^4 + k_3 r^6) + s_1 r^2 + s_2 r^4 \tag{3.5}$$

$$y'' = y'(1 + k_1 r^2 + k_2 r^4 + k_3 r^6) + s_3 r^2 + s_4 r^4 \tag{3.6}$$

Here k_1 to k_3 describe radial lens distortion and s_1 to s_4 add a small directed component according to the thin prism model. During evaluation of other options provided by OpenCV, no significant improvement of the calibration result was found using more parameters. Finally, the pixel coordinates can be calculated by a linear transformation, which is often called "camera matrix" (e.g. Bradski and Kaehler, 2008):

$$u = f_x x'' + c_x \tag{3.7}$$

$$v = f_y y'' + c_y \tag{3.8}$$

Here, f_x and f_y describe the focal lengths and c_x and c_y describe the principal point of the optical system. In this model, there are 6 extrinsic parameters (rotation matrix R and displacement vector $\vec{t}$) and 11 intrinsic parameters $(k_1 ... k_3, s_1 ... s_4, f_x, f_y, c_x, c_y)$.

Chessboard Method

We use the chessboard calibration method (based on Zhang, 2000) to calibrate this model. The basic idea is to relate a known arrangement of points in 3D world space to their corresponding locations on the 2D image plane by a model as described above and solve for the parameters by fitting it to a set of sample images. The internal corners of a rectangular chessboard provide a good set of such points as they are defined at intersections of easily and automatically recognizable straight lines. Furthermore, the intersection of two lines can be determined to sub-pixel accuracy which improves the calibration performance substantially. While the extrinsic parameters have to be fitted independently for every image, the intrinsic parameters must be the same for each image and can be determined reliably if enough sample images covering the whole sensor are considered.

To evaluate the success of the calibration, the reprojection error can be used as a first quality measure. The reprojection error is defined as the difference of the calculated pixel position using the calibrated projection model and the measured pixel position on the image sensor. To calculate the pixel position, the extrinsic parameters (R and $\vec{t}$) have to be known, thus the images which have been used for calibration are used to calculate the reprojection error as well. This makes this test susceptible to return good results, even in case of a bad calibration, due to an overfitted model. We use many more images (of which each provide multiple constraints to the fit) than parameters to counter this issue. Additionally, the stereo method (which includes the calibration) has been validated against other sensors to ensure that the calibration is indeed of good quality. Nonetheless, a high reprojection error would indicate a problem in the chosen camera model.

We have taken 62 images of a 9 by 6 squares chessboard pattern with 65 mm by 65 mm square size on an aluminium composite panel using the system assembled in aircraft configuration. The images have been taken such that the chessboard corners are spread over the whole sensor area, Figure 3.9 shows the pixel locations of all captured chessboard corners. After previous experiments with calibration targets made from paper and cardboard, it became clear that small ripples which inevitably appeared on the cardboard targets render the reprojection errors unusable high. Using the rigid aluminium composite material for the calibration target let the average reprojection error drop by an order of magnitude to a very low value of approximately 0.15 pixels, which should be enough to reduce systematic errors across the camera to less than 50 m. The per pixel reprojection error is shown in Figure 3.10 for every chessboard corner captured.

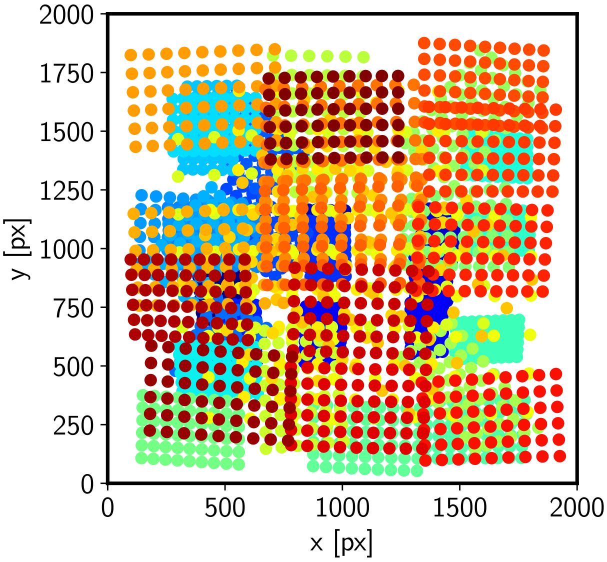

Figure 3.9: Locations of each chessboard corner during calibration on the image sensor plane.

The calibration used for this work has been performed using gray scale versions of the captured chessboard images. To assess effects of spectral aberrations, the procedure has been repeated separately for each channel. A comparison shows that observed viewing angle differences vary up to the order of $1 - 2$ ‰ when switching between different calibration data. For the example used in the beginning of this section, this translates into cloud height differences of about 10 m, which is considerably lower than the total errors achievable by this calibration method. Due to effectively using fewer pixels when doing the camera calibration procedure on a single channel image, the reprojection error is increased accordingly. For these reasons, and in order to facilitate data handling, only one set of calibration data is used. Effects of spectral aberrations within one color channel have not been assessed, but are assumed to be smaller than effects between color channels.

Geo Referencing

The HALO aircraft provides reliable aircraft position and attitude information from a GPS-referenced inertial navigation unit with an output data rate of 100 Hz. This data is quality checked and post processed by the group for sensor techniques of the DLR flight experiments department in Oberpfaffenhofen. Thus, after obtaining the intrinsic camera parameters by the chessboard calibration method, the missing link is the position and orientation of the cameras with respect to the airframe. The design documents of the measurement system provide an initial guess for the exact mounting position inside the

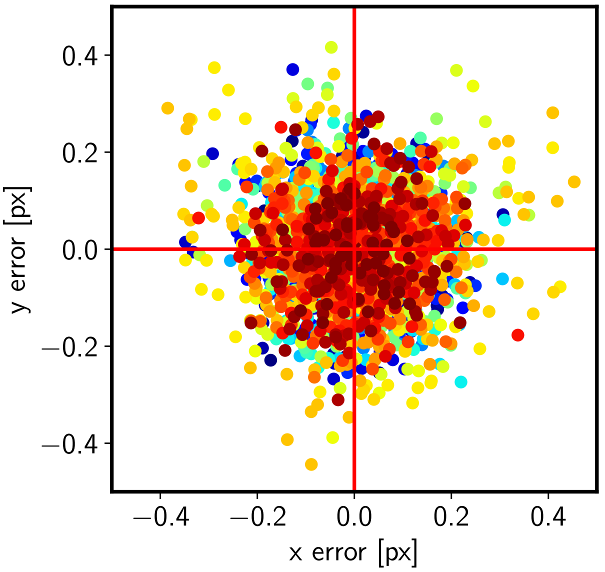

Figure 3.10: Reprojection error: Difference between the actual position of the chessboard corners and the calculated positions of the chessboard corners after applying the camera calibration. The average reprojection error is about 0.15 pixels. Note that the actual chessboard corner locations can be found far into sub-pixel accuracy by following the lines along the edges of the squares.

airframe, but due to mounting tolerances and missing knowledge about the exact internal construction of the cameras, the exact alignment has to be obtained after installing the sensors in the airframe. While the sensors are mounted, their location inside the airframe does not change anymore. Thus it is sufficient to determine the orientation once per field campaign. In order to do so, a mounttree (Sec. 3.3.2) for the field campaign is pre-filled with an initial guess about the location and orientation of all sensors. This information is then used to project a few images from the sensor onto the earth's surface. This is done by undistorting each image and annotating the resulting image with WGS84 coordinates of the corners using a KML file. The images are then overlaid on satellite imagery in Google Earth. If the images do not match up with the satellite data, the initial guess of the mount tree can be adjusted manually until an optimal result is achieved. Figure 3.11 shows two images aligned in this manner. For the final adjustment, several images from different flight altitudes have been used.

In order to calculate the WGS84 coordinates of the four image corners, additional information about the earth surface is required. In particular this is the geoid undulation (i.e. difference between ellipsoid and mean sea level) and, if the observed scene is not on sea level, a digital elevation model (i.e. difference between mean sea level and terrain). As a model for the geoid undulation EGM2008 is used via GeographicLib (Karney, 2009). The terrain elevation may not be assumed as constant across the observed scene and it is

Figure 3.11: An example for the finished alignment procedure of the 2D camera during takeoff at the Grantley Adams International Airport on Barbados: the images have been aligned according to the procedure described in Section 3.3.1, both using the same final mounttree. The left image has been projected using the runway elevation as terrain height, while the right image has been projected using 0 (i.e. sea level) as terrain height. As there is a difference of about 50 m in elevation, only the runway or the shoreline match up in the reprojection respectively.

important to use a terrain height consistent with the presentation of the satellite images. Thus the user interface of Google Earth is used to obtain the terrain elevation at the exact location of the features used to align the projected images.

3.3.2 Related Coordinate Frames – Mounttree

When working with measurement data from multiple sensors on a moving platform (or multiple platforms), many different coordinate frames arise naturally. While the relation between these coordinate frames is described just by translations and rotations, the precise definition and order of these transformations quickly can become hard to manage. Furthermore, when collaborating with coworkers, a formal definition of the coordinate frames used and their interrelation helps to minimize errors. The goals of the developed mounttree system are:

- to provide a textual representation of all relevant coordinate frames including a name and it's relation to other frames
- to provide a simple interface to obtain a transformation from any defined coordinate frame into any other coordinate frame
- The textual representation should be human readable and should interact well with version control systems, so that changes in the definition of the coordinate frames can be documented reliably.
- As the aircraft moves over time, the relation between aircraft coordinates and ground based coordinates must be changeable using placeholder variables.
- While Cartesian coordinate frames are preferred as they allow simple treatment of straight lines, curved coordinate frames must be representable as well, such that WGS84 can be handled.
- The system should be small, easy to understand and easy to implement such that it will actually be used.

Evaluated Alternatives

PROJ (2019) is a well known and robust library and notation for the treatment of cartographic projections, but it is mainly focussed on non-moving coordinate systems treating the earth's surface. As moving coordinate systems and the description of locations in the earth's atmosphere are the primary concern, PROJ is not applicable for this purpose. SensorML (2014) seems to be a solid standard for the description of moving and non-moving sensors, their measurement principles, data streams, calibration procedures and more. This is far more than currently needed and as the standard document is about 200 pages long, it also does not qualify as small or easy anymore, thus is has not been considered furthermore. If a major redesign of the data processing chain will be done in future, it might however be worth to revisit Sensor ML as an alternative again.

Design

The core concept of the mounttree is a single-rooted tree of Cartesian coordinate frames. The root usually is the earth and the children are arbitrary defined coordinate frames, which are related by a translation and a rotation to the parent coordinate frame. Figure 3.12 shows the corresponding geometry with 3 coordinate frames. In this example, the x, y, z frame would be a global reference frame, in the center of the earth. N, E, D denotes a coordinate frame on the surface which is oriented northwards, like a local map coordinate frame. Finally, x', y', z' would be an aircraft frame. Further coordinate frames for the sensors could then be defined in relation to the aircraft frame in the same manner. The direct relations between these coordinate frames are shown by dashed lines. By searching for a series of direct relations between two frames further apart, an indirect relation can be established. The possibility of indirect relations allows to update all sensor locations and orientations automatically as soon as the aircraft location is updated.

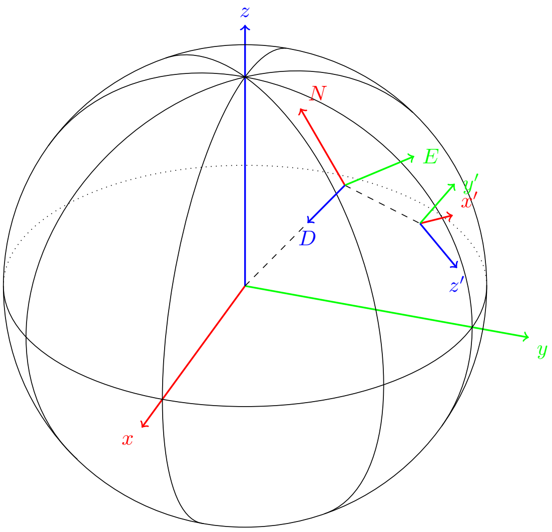

Figure 3.12: Three related coordinated frames: the root coordinate frame is the x, y, z frame, which is located in the center of the earth. The two other coordinate frames are defined in relation to the root frame (indicated by the dashed lines). The x', y', z' frame is defined in relation to the N, E, D frame, thus changing the latter will also influence the former.

A relation between two coordinate frames can either be expressed through constant numbers, corresponding to a fixed mount, or by variable names, corresponding to a moving relation. As indicated in the Fig. 3.12, a Cartesian coordinate frame can further be overlaid by a curved "natural" coordinate frame. This is used to represent the WGS84 system of the earth. If no natural coordinate frame is defined, the natural frame is assumed to be identical to the Cartesian frame.

The tree structure and the transformations between the coordinate systems are written manually in a YAML file (Ben-Kiki et al., 2009) and can be read and processed by the mounttree library, which is currently available in Python and C++. A simplified YAML example for the mounttree used for the NARVAL-II field campaign can be seen below:

```
mounttree:
  framename: EARTH                                  ❶
  framespec: WGS-84                                 ❷
  subframes:                                        ❸
  - framename: local horizon
    position: [lat, lon, height]                    ❹
    rotation: [0, 0, 0]                             ❺
    subframes:
    - framename: HALO
      position:                                     ❻
      rotation: [roll, pitch, yaw]                  ❼
      subframes:
      - framename: containment
        position: [-23, 0, 0]                       ❽
        rotation: Rx(-2.5deg)*Rz(-90deg)            ❾
        subframes:
        - framename: VNIR
          position: [0, 0, -0.3]
          rotation:                                 ❿
        - framename: SWIR
          position: [0, 0, -0.2]
          rotation: Rz(180deg)
        - framename: 2DCAM
          position: [0, 0, -0.35]
          rotation:
  - framename: reference
    rotation:
    position: [19, -49, 0]
```

---

❶A coordinate frame has a name.

❷Optionally, it can refer to a predefined frame specification.

❸A coordinate frame may have any number of sub frames.

❹Position is given in natural coordinates of the parent frame. Variable names can be used.

❺Rotation can be given in euler angles.

❻If the coordinate frame is at the same origin as the parent, position may be ommited.

❼Euler angles may also come from variables.

❽Position may also be given as constant values.

❾Alternatively, rotation can be given as a requence of rotation matrices.

❿As with position, if the frame is not rotated relative to the parent, rotation may be ommitted.

The root frame "EARTH" defines the *framespec* attribute to "WGS-84", this changes its natural coordinates to latitude, longitude and height according to the WGS84 reference ellipsoid. Coordinate frames, which are defined as *subframes* define a *position* and *rotation* according to the natural coordinates of the parent frame. Inside the *position* and *rotation* attributes, either constant values or variable names can be used. For convenience, rotation can either be specified as $[roll, pitch, yaw]$ tuples or as a product of rotation matrices about one of the three coordinate axes.

The mounttree library can load such a definition file and basically provides two methods to the user, GET_TRANSFORMATION(from, to, variables) and GET_FRAME(name).

- The GET_TRANSFORMATION(from, to, variables) method returns a transformation object, able to convert between two named coordinate frames if the user provides values for all variables in the mounttree definition. The resulting transformation object offers again two methods, one to transform position vectors and one to transform directional vectors. These methods only operate on Cartesian coordinates.
- The GET_FRAME(name) method returns a coordinate frame object, which allows to transform between Cartesian and natural coordinates of that frame.

Thus a full transformation using natural coordinates would first go from natural to Cartesian in the source frame, then transform between two frames and finally go back to natural coordinates in the final frame.

Usage

The mounttree shown in the previous section shows the typical layout used for the field campaigns as described in this thesis. Additional to the obvious solid objects (EARTH, HALO, VNIR, SWIR and 2DCAM), three additional coordinate frames are defined to aid adjustment and some calculations.

- local horizon: a coordinate frame which is located at the aircraft's location but oriented horizontal and its x-axis towards local north. This allows to easily define a down-direction and, as this definition is quite common in atmospheric physics, to interface with libraries operating on locations on the earth's surface (e.g. some sun position algorithms).
- reference: a coordinate frame which is tangential to the earth's surface and fixed at a per-campaign defined location. This frame allows to relate measurements from multiple measurement locations, most ray tracing and stereographic calculations are performed in this frame.
- containment: a helper frame corresponding to the box which contains the cameras. This allows to adjust the absolute orientation of all cameras once the relation between the cameras has been found.

Depending on the application, additional frames have been defined. An example would be an additional reference frame, which is tailored to a small section of the flight. This allows to define a local coordinate frame, which corresponds to a smaller modelling domain, which is aligned to the mean flight direction instead of the north direction for computational simplicity.

3.4 Stereographic 3D Reconstruction

The idea of the stereographic 3D cloud surface reconstruction method is to find visible structures which indicate points on a cloud surface and re-identify them in following images. Aircraft location and camera calibration allows to triangulate the location of these points. The cloud surface is then reconstructed from the resulting points.

In order to identify points on the cloud surface and to re-identify the same points in another image, the cloud surface region is required to show a pronounced contrast and to look similar in the subsequent image. This requires to first capture well exposed images, which is taken care of by the automatic exposure control system. Due to resulting changes in exposure time, equal brightness in consecutive images then does not necessarily result in equal numerical values anymore. To fix this, the images need to be preprocessed prior to point identification.

3.4.1 Image Preconditioning

In order to establish pronounced contrasts in the captured images and to ensure consecutive images of the same parts of the clouds are represented by similar numerical values, the captured image data are preprocessed prior to the actual 3D reconstruction. First, the raw image data is converted to floating point values, so that values from 0 to 1 represent the full dynamic range of the sensor. The resulting values are rescaled by the gain and exposure time of the captured image. In this way, two images of the same scene using different exposure times will be mapped to similar resulting values.

The following tracking algorithm uses finite length sequences of subsequent images encoded as unsigned 8-bit integers. These sequences are first cut out of the stream of floating point images and each sequence is rescaled individually to fully utilize the value range between 0 and 1. At this stage, a brightness transformation, e.g. gamma correction, can be inserted into the preprocessing in order to enhance contrast of specific parts of the image. For the tracking of clouds, which usually are the brightest parts of the image, the identity function is usually fine. Depending on the scene, this adjustment point can nonetheless be valuable. Finally, the images of the sequence are scaled to values of 0 to 255 and converted to 8 bit unsigned integers for further processing.

3.4.2 From Images to Points

This section contains work which has already been published in Atmospheric Measurement Techniques (AMT) by Kölling et al. (2019).

The goal of the 3D reconstruction method is to find georeferenced points which are part of a cloud surface at a specific time in an automated manner. Input data are geometrically calibrated images from a 2D camera fixed to the aircraft. As the aircraft flies, pictures taken at successive points in time show the same clouds from different perspectives. A schematic of this geometry is shown in Fig. 3.13. The geometric calibration of the camera and the rigid mounting on the aircraft allows to associate each sensor pixel with a viewing direction in the aircraft's frame of reference. Using the aircraft's navigation system, all relevant distances and directions can be transformed into a geocentric reference frame in which most of the following calculations are performed.

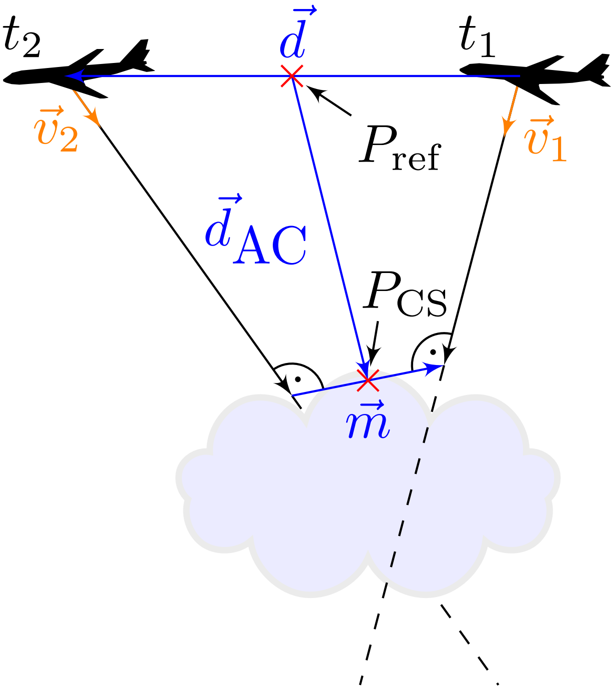

Figure 3.13: Schematic drawing of the stereographic geometry. Images of clouds are taken at two different times from a fast moving aircraft. Using aircraft location and viewing geometry, a point P_{CS} on the clouds surface can be calculated. Note that the drawing is not to scale: $\vec{d}$ is typically around 200 m, $\vec{d}_{\text{AC}}$ in the order of 5 km and $\vec{m}$ is a description of mis-pointing and in the order of only a few meters.

In order to perform a stereo positioning, a location on a cloud must be identified in multiple successive images. A location outside of a cloud is invisible to the camera, as it contains clear air, which barely interacts with radiation in the observed spectral range.

Locations enclosed by the cloud surface do not produce strong contrasts in the image, as the observed radiation is likely scattered again before reaching the sensor. Thus, a visible contrast on a cloud is very likely originating from a location on or close to the cloud surface as defined in the introduction. This method starts by identifying such contrasts. If such a contrast is only present in one direction of the image (basically, we observe a line), this pattern is not suitable for tracking to the next image due to the aperture problem (Wallach, 1935). We thus search one image for pixels of which the surroundings show a strong contrast in two independent directions. This corresponds to two large eigenvalues (λ_1 and λ_2) of the Hessian matrix of the image intensity. This approach has already been formulated by Shi and Tomasi (1994): interesting points are defined as points with $\min(\lambda_1, \lambda_2) > \lambda$ with λ being some threshold. We use a slightly different variant and interpret $\min(\lambda_1, \lambda_2)$ as a quality measure for each pixel. In order to obtain a more homogeneous distribution of tracking points over the image, candidate points are sorted by quality. Points which have better candidates at a distance of less then r_{min} are removed from the list and the remaining best N_{points} are taken. For these initial points, matches in the following image are sought using the optical flow algorithm described by Lucas and Kanade (1981). In particular, we use a pyramidal implementation of this algorithm as introduced by Bouguet (2000). If no match can be found, the point is rejected.

The locations of the two matching pixels define the viewing directions $\vec{v}_1$ and $\vec{v}_2$ in Fig. 3.13. The distance travelled by the aircraft between two images is indicated by $\vec{d}$. Under the assumption that the aircraft travels much faster than the observed clouds, an equation system for the position of the point on the cloud's surface P_{CS} can be found. In principle, P_{CS} is located at the intersection of the two viewing rays along $\vec{v}_1$ and $\vec{v}_2$, but as opposed to 2D space in 3D space there is not necessarily an intersection, especially in presence of inevitable alignment errors. We relax this condition by searching for the shortest distance between the viewing rays. The shortest distance between two lines can be found by introducing a line segment which is perpendicular to both lines. This is the mis-pointing vector $\vec{m}$. The point on the cloud's surface P_{CS} is now defined at the center of this vector. If for further processing a single point for the observer location is needed, the point P_{ref} at the center of both aircraft locations is used.

This way, many points potentially located on a cloud's surface are found. Still, these points contain a number of false correspondences between two images. During turbulent parts of the flight, errors in synchronization between aircraft navigation system and camera will lead to errors in calculated viewing directions. To reject these errors, a set of filtering criteria is applied (the threshold values can be found in Tab. 3.1). Based on features of a single P_{CS}, the following points are removed:

- P_{CS} position is behind the camera or below ground
- absolute mis-pointing $|\vec{m}| > m_{\text{abs}}$
- relative mis-pointing $|\vec{m}|/|\vec{d}_{\text{AC}}| > m_{\text{rel}}$

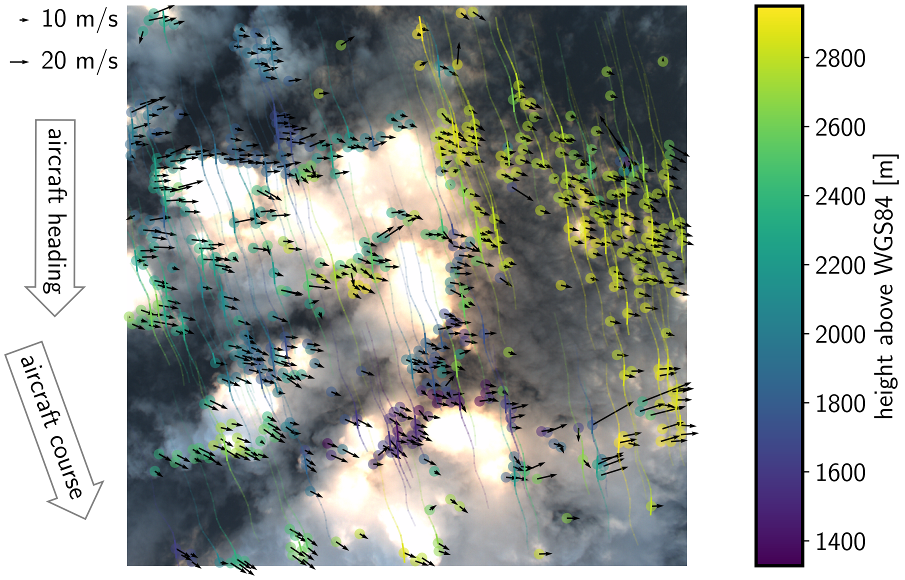

Figure 3.14: Image point tracking, every line in this image represents a cloud feature which has been tracked along up to 30 images. The images used have been taken on the NAWDEX flight RF07 (2016-10-06 09:32:15 UTC, location indicated in figure 4.16) in an interval of 1 s. Transparency of the tracks indicates time difference to the image. Color indicates retrieved height above WGS84, revealing that the larger clouds on the left belong to a lower layer than the thin clouds on the right. The arrows indicate estimated cloud movement. Due to the wind speed at the aircraft location, it's course differs significantly from the heading and the tracks are tilted accordingly. The number of points shown has been reduced to include at maximum 1 point per 20 px radius in the image. Tracks are only shown for every 5th point.

Figure 3.14 shows long tracks corresponding to a location on the cloud surface. These tracks follow the relative cloud position through up to 30 captured images. The tracks are generated from image pairs by repeated tracking steps originating at the t_2 pixel position of the previous image pair. Using these tracks, additional physics based filtering criteria can be defined.

Each of these tracks contains many P_{CS} points which should all describe the same part of the cloud. As clouds move with the wind, the points P_{CS} do not necessarily have to refer to the same geocentric location, but should be transported with the local cloud motion. For successfully tracked points, it can indeed be observed that the displacement of the P_{CS} points in a 3D geocentric coordinate system roughly follows a preferred direction in stead of jumping around randomly, which would be expected if the apparent movement would just be caused by measurement errors. The arrows in figure 3.14 show the average movement of the P_{CS} of each track, reprojected into camera coordinates.

For the observation period (up to 30 s) it is assumed that the wind moves parts of a cloud on almost straight lines at a relatively constant velocity (which may be different for different parts of the cloud). Then, sets of P_{CS} can be filtered for unphysical movements. The filtering criteria are

- *velocity jumps*: the fraction of maximum to median velocity of a track must be less than v_{jump}
- *count*: the number of calculated P_{CS} in a track must be above a given minimum N_{min}
- *distance uncertainty*: the distance $\vec{d}_{\mathrm{AC}}$ between aircraft and cloud may not vary more than d_{abs} or the relative distance variation with respect to the average distance of a track must be less than d_{rel}

Table 3.1: Filter thresholds

name	value
N_{points}	1000
r_{min}	5 px
m_{abs}	20 m
m_{rel}	1.5×10^{-3}
v_{jump}	3
N_{min}	5
d_{abs}	250 m
d_{rel}	7×10^{-2}

During measurements close to the equator, typical during the NARVAL-II campaign, the sun is frequently located close to the zenith. In this case, specular reflection of the sunlight at the sea surface produces bright spots, known as sunglint and illustrated in figure 3.15. Due to waves on the ocean surface, these regions of the image also produce strong contrasts. It turns out that such contrasts are preferred by the Shi and Tomasi algorithm for feature selection, but are useless in order to estimate the cloud surface geometry. To prevent the algorithm from tracking these points, the image area in which bright sunglint is to be expected is estimated using the bidirectional reflectance distribution function (BRDF) by Cox and Munk (1954) included in the libRadtran package (Mayer and Kylling, 2005; Emde et al., 2016). The resulting area (indicated by a red line in fig. 3.15) is masked out of all images before any tracking is performed. Masking out such a large area from the camera image seems to be a wasteful approach. In fact it is acceptable, because due to the large viewing angle of the camera, all masked-out clouds are almost certainly visible at a different time in another part of the image. Therefore, these clouds can still be tracked in the presence of sunglint.

After filtering, a final mean cloud surface point $\bar{P}_{\mathrm{CS}}$ is derived from each track as the centroid of all contributing cloud surface points. The collection of all $\bar{P}_{\mathrm{CS}}$ form a point

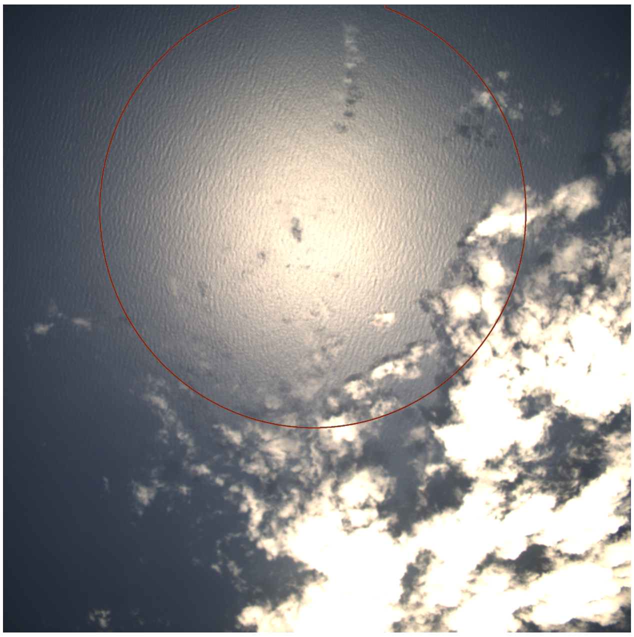

Figure 3.15: At low latitudes, close to the local noon as on the NARVAL-II flight RF07 (2016-08-19 15:06:13 UTC), the specular reflection of the sun on the ocean surface (sunglint) produces bright spots and high contrasts on the waves tails. While the bright spots can visually hide clouds, the contrasts create useless initial tracking points. The latter are mitigated by calculating the region of a potential sunglint (shown as red contour) and masking that region before the images are processed.

cloud in a Cartesian 3D reference coordinate frame which is defined relative to a point on the earth's surface (figure 3.16). This point cloud can be used on its own, serve as a reference for other distance measurement techniques (e.g. oxygen absorption methods (Zinner et al., 2019), distances derived by a method according to Barker et al. (2011)) or allow for a 3D surface reconstruction.

3.4.3 From Points to Surfaces

The process of converting a point cloud into connected surface data is called surface reconstruction. As described by Bolitho et al. (2009), surface reconstruction methods are typically divided into two categories:

Computational Geometry: The general idea of computational geometry is to connect most or all points of the input point cloud by some means of triangulation. Typical methods are Delaunay triangulation or alpha shapes. Computational geometry methods can be seen as a direct construction of a mesh of parametric surfaces as defined in Section 2.2.3. The problem of computational geometry methods is the fact that these methods interpolate

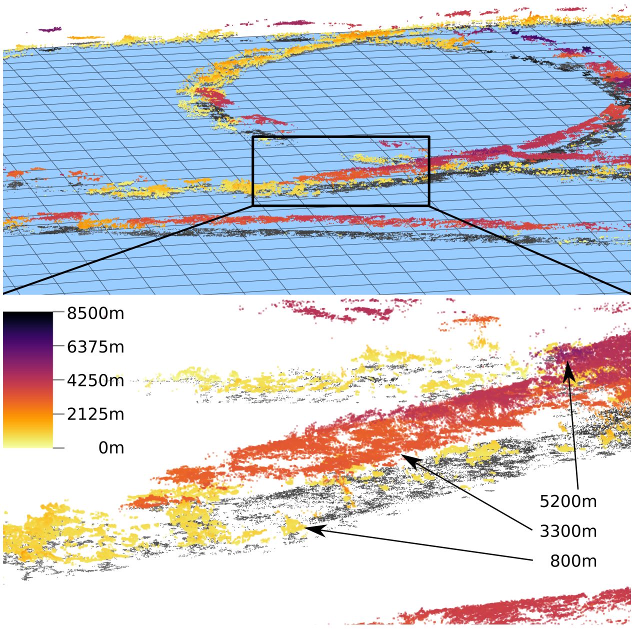

Figure 3.16: The collection of all $\bar{P}_{\mathrm{CS}}$ form a point cloud. Here, a scene from the second half of the NARVAL-II flight RF07 is shown. The colors indicate the points height above the WGS84 reference ellipsoid (indicated as blue surface). Below, a part of the scene is shown magnified, displaying two main cloud layers: one at about 800 m in yellow and the other at about 3200 m in orange. On the left, a small patch of even higher clouds is visible at 5200 m. The gray dots are a projection of the points onto the surface to improve visual perception.

between all or many of the source points, which makes the algorithms very susceptible to noise. As a plus, computational geometry typically does not need any information about surface normals at the point locations.

Function Fitting: Function fitting methods approach the problem from the perspective of implicit surfaces (Sec. 2.2.3). Accordingly, these methods estimate a continuous function $f(x, y, z)$ which should be zero-valued on the surface to be estimated. According to Section 2.2.2, the function will be chosen to have a negative value in "inside" regions and a positive value in "outside" regions. Furthermore, methods with *global* and *local* support can be distinguished. If the function value at a specific point in space depends on all input data, the method is called a *global fitting* method. If the value at a specific point depends only on input data in its vicinity, the method is called a *local fitting* method. While global methods generally provide smoother and more optimal solutions, for large input datasets, the computational effort can quickly become too large and numerically unstable. Depending on the size of the local neighborhood, local methods can provide a good compromise between quality of the solution and feasibility of the computation.

In this work, for the transformation of point clouds into surface meshes, Poisson surface reconstruction is used, which is based on the latter of the above categories. This form of surface reconstruction requires an estimate for surface normal vectors on each input point, so surface normal estimation is a prerequisite to the actual surface reconstruction

Normal Estimation

An useful intermediate step from points to surfaces, are surface normal vectors. This might seem to be contradictory as surface normal vectors are obviously a property of their surfaces. However, given a point and some points in its local neighborhood, it is possible to locally fit a plane surface (Rusu, 2009, chap. 4.3). This fitted surface yield an estimate for the surface normal vector at the point's location. However, the normal resulting from the fit alone is ambiguous, as it can point to either side of the resulting plane. The points obtained from the stereographic method as described above also carry information about the location of their observer ($\vec{P}_{\mathrm{ref}}$). This information can be used to orient each estimated normal towards the observer (i.e. such that $(\vec{P}_{\mathrm{ref}} - \vec{P}_{\mathrm{CS}}) \cdot \vec{n} \geq 0$). As the observer can only observe cloud borders while being outside of a cloud, this oriented surface normal estimate is guaranteed to point towards the outside of any cloud.

Poisson Surface Reconstruction

Poisson surface reconstruction uses surface normal estimates to construct the implicit surface function. Kazhdan et al. (2006) describes this method very well, the nomenclature is however slightly different from this thesis. The implicit surface is described by an indicator function $\mathcal{X}_M$, which is defined as 1 inside the surface and 0 outside of the surface. Points equipped with normal vectors are called oriented points and are, in this case, oriented inwards. These oriented points form a vector field $\vec{V}$ and are used as an approximation for the gradient $\nabla \mathcal{X}_M$ of the indicator function. These fields are illustrated in Figure 3.17.

Finding the implicit surface $\mathcal{X}_M$ can now be seen as

$$\min_{\mathcal{X}_M} ||\nabla \mathcal{X}_M - \vec{V}|| \tag{3.9}$$

which transforms into Poisson's equation by applying ∇:

$$\begin{aligned} \nabla\nabla \mathcal{X}_M - \nabla \vec{V} &= 0 \qquad (3.10) \\ \Delta \mathcal{X}_M &= \nabla \vec{V} \qquad (3.11) \end{aligned}$$

Poisson's equation is well studied and many solvers have been developed. In this work, the implementation by Rusu and Cousins (2011) is used, which in turn is based on Kazhdan et al. (2006); Kazhdan and Hoppe (2013). This implementation solves the equation on

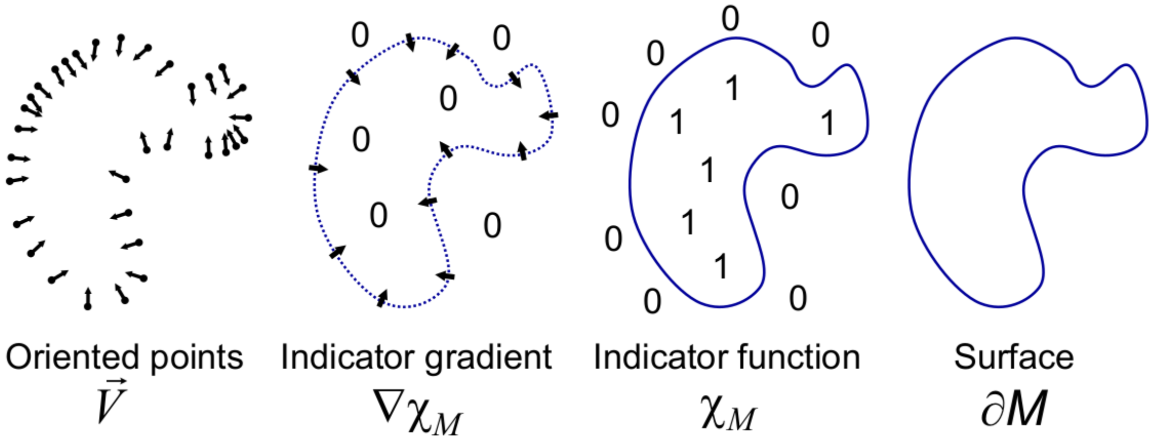

Figure 3.17: Poisson surface estimation: Oriented points are used to approximate the gradient of the implicitly defined surface $\mathcal{X}_M$. (From Kazhdan et al. (2006))

an octree based grid, which adapts its resolution to the amount of detail available in the source points. While Poisson based surface reconstruction offers the in general desirable property of always generating closed surfaces, this can not be exploited fully for the datasets generated using the stereographic method from one aircraft alone. Due to the view from above, no surface points below the clouds can be generated, and thus the point sets are naturally open on the bottom side of the clouds. In this case, the Poisson solution often chooses to connect all clouds with a rubber sheet like structure. As for current applications, the lower cloud boundary is not as important as the upper cloud boundary, vertices of the resulting mesh are simply cut if they are more then a configurable distance threshold away from any source point.

3.5 Applications of Cloud Surface Location Data

The availability of cloud surface location data and in particular the reconstructed cloud surface mesh enables further methods to evaluate the data from the specMACS instrument. Using ray tracing from the sensor locations into the geometric model of the observed scene allows to derive if sensor pixels have observed shadowed or directly illuminated regions of the scene. Additionally, a similar process allows to accurately project data between the coordinate systems of different sensors in a way which implicitly accounts for differences in sensor orientation and measurement timestamps. Finally, the cloud surface orientation, which can also be derived from the surface mesh, can be used as an additional input to bi-spectral cloud microphysics retrievals.

3.5.1 Geometric Shadow Mask

Cloud microphysics retrievals based on one-dimensional simulations of reflected spectral radiance generally assume mostly direct illumination by sunlight. While methods based on pixel brightness exist (Jäkel et al., 2017; Ewald et al., 2019), the cut-offs of such methods usually correlate with cloud water content and droplet effective radius and thus may selectively exclude some otherwise valid retrieval results. Using the reconstructed cloud surface, another approach to shadow detection becomes available. Using e.g. the RayLi ray tracing code, it is possible to virtually cast viewing rays from the spectral cameras onto the cloud's surface and then back to the sun. In radiative transfer terms, this second ray is often called "local estimate", however in this case, the computer graphics term "shadow ray" is somewhat more appropriate and thus used here. If this shadow ray intersects with any other cloud, the origin of the shadow ray is shadowed and should be excluded from the microphysical retrieval. As the goal of this shadow mask is to identify pixels which are safe to use in a microphysical retrieval, it is better to overestimate the size of the shadowed region than to underestimate it. This allows to add a little modification to this approach in order to represent the fuzzy cloud border: the shadow ray is not intersected with the original cloud surface, but with an elevated surface, which is defined by a parallel shift of the cloud boundaries outwards by a distance d_{elev}. Additionally, a keep out zone around the intersection point of the primary ray is defined, in which intersections with the elevated surface are not counted. By choosing the size of the keep out zone as $r = d_{\mathrm{elev}} / \cos \Theta_{\max}$, very slanted incoming light paths can be excluded as well.

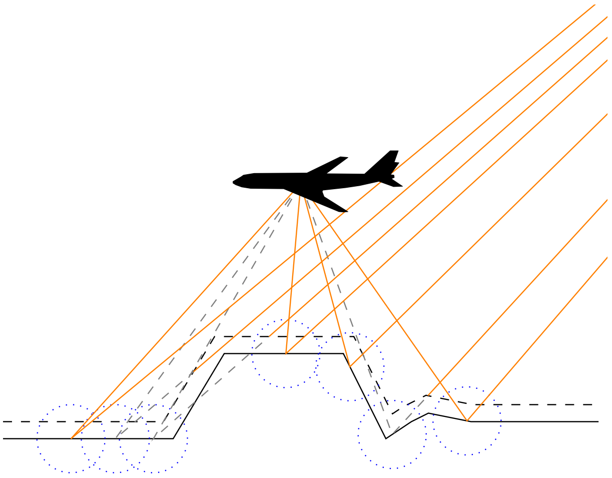

Figure 3.18: For each pixel of the airborne sensor, a ray is traced onto the cloud surface (solid black line). The shadow ray is then traced from the intersection point to the sun. If this shadow ray hits the elevated cloud (dashed line) outside of the keep out zone (dotted blue circles), the pixel is marked as shadowed (dashed gray viewing lines).

3.5.2 3D Image Reprojection

The specMACS measurement system uses a combination of multiple imaging sensors, which operate at different resolutions, sampling rates and sensor orientations and which are moving at high velocity. Combining the data from all of these sensors requires to project between the coordinate frames of the individual sensors on to a common data grid. If the pixels of the individual sensors do not point exactly in the same direction, they still might observe the same clouds, but maybe at slightly different points in time. This is especially true for the line cameras (e.g. VNIR and SWIR), but also applies for the two dimensional sensors, if a certain viewing geometry (e.g. glory, cloudbow, sunglint) should be used for the observation. The problem becomes a lot easier if it is solved in 3D space and if it can be assumed that the observed scene does not change substantially between the individual observations. If a georeferenced surface mesh of the observed scene is available, a ray from each sensor pixel can be traced into the scene and the first intersection is recorded as the effective observation location of the pixel. Now, the association of pixels from different sensors is simply a nearest-neighbor search in 3D space. This method implicitly covers all aspects of lens distortion, sensor movement and timing issues.

3.5.3 Bi-Spectral Cloud Property Retrieval

As outlined in Section 2.1.3, most of the interaction between clouds and radiance can be explained by the amount of water inside a cloud, expressed by the liquid water path LWP and the effective droplet radius r_{eff}. The cloud optical thickness at a given wavelength τ_λ can be calculated from LWP and r_{eff}. Also, LWP can be calculated from τ_λ and r_{eff}. In the solar spectral range, the optical thickness does not change very much between different wavelengths, so this dependence is sometimes omitted and LWP and τ_λ can be used almost interchangeably with respect to a cloud property retrieval. However, this study generally uses LWP to escape this ambiguity.

The two important effects determining radiative transfer in clouds are scattering and absorption (Sec. 2.1.2). Light scattering on particles is mostly determined by the particle cross section and absorption is mostly determined by the particle mass. Accordingly, if absorption and scattering can be observed independently, or at least in a separable fashion, it should be possible to learn something about particle size and particle mass.

Nakajima and King (1990) show how this can be used to retrieve optical thickness and effective droplet radius from radiance measurements at two different wavelengths. They use radiance measurements at one wavelength (0.75 µm), where water has a very low absorption cross section and measurements at another wavelength (2.16 µm), at which water has a comparably large absorption cross section. This way, changes in cloud optical thickness and changes in droplet effective radius affect the reflected radiance in different ways, which allows to build a table for the look up of the values of τ and r_{eff} for a given pair of radiance measurements.

Look-Up Table

Through forward radiative transfer simulations depending on liquid water content and droplet effective radius, the radiance which is expected to be received at the sensor can be calculated. This pre-calculated table can subsequently be used to obtain a pair of LWP and r_{eff} from a pair of measured radiances. The choice of the exact tabulated quantities offers some freedom. As the distance between earth and sun varies throughout the year (e.g. Iqbal, 1983), the radiant flux arriving at the earth (extraterrestrial irradiance, E_0) changes accordingly. This is of course irrelevant to the retrieval of microphysical properties of clouds and can be accounted for by normalizing the tabulated radiance by the extraterrestrial irradiance. Nakajima and King (1990) assume a one-dimensional setting with a horizontal cloud layer. In this setting, is is useful to picture the cloud surface as a solid surface with given albedo, which motivates their definition of the reflection function:

$$R(\tau, r_{\text{eff}}; \mu, \mu_0, \Phi_\Delta) = \frac{\pi L(-\mu, \Phi_\Delta)}{\mu_0 E_0} \tag{3.12}$$

Here, μ and μ_0 are the cosines of the viewing and solar zenith angle and Φ_Δ the relative azimuth between sun and viewing direction. The simulated scene is rotationally symmetric about the cloud surface normal, so only the relative azimuth is relevant for the retrieval. If the cloud surface would reflect isotropically, Eq. 3.12 would match the surface albedo, hence the choice of the weighting.

This weighting is useful for the plane-parallel setting, where cloud surface normal and zenith direction coincide. For three dimensional clouds, the cloud surface normal and the zenith direction diverge. That way and in particular with respect to the upcoming tilted retrieval approach, it becomes less evident, which angle would be the sensible angle to use for the cosine weighting and the weighting is not key to the retrieval approach. Therefore, the look-up tables used in this work do not show the same reflection function, but just use normalized radiance in stead:

$$L_{\text{norm}}(\text{LWP}, r_{\text{eff}}; \Theta_{\text{v}}, \Theta_{\text{s}}, \Phi_\Delta) = \frac{L(\Omega)}{L_0(\Omega_0)} \tag{3.13}$$

Additionally, these look-up tables directly refer to liquid water path LWP and express the viewing (Θ_{v}) and sun (Θ_{s}) directions as angles in stead of cosines. Here, Ω is used to denote direction as introduced in Sec. 2.1, Ω and Ω_0 can be calculated from Θ_{v}, Θ_{s} and Φ_Δ. The solar radiance is explicitly considered as radiance L_0 to emphasize the importance of the incident direction of the solar radiation. A typical look-up table entry is shown in Figure 3.19.

These examples of the look-up table already illustrate important characteristics of this kind of dual wavelength cloud property retrievals. Clouds can not reflect more light than they receive from the sun. Consequently, there is an upper limit for the observable radiance, reflected from the cloud surface. Clouds with large values of liquid water content

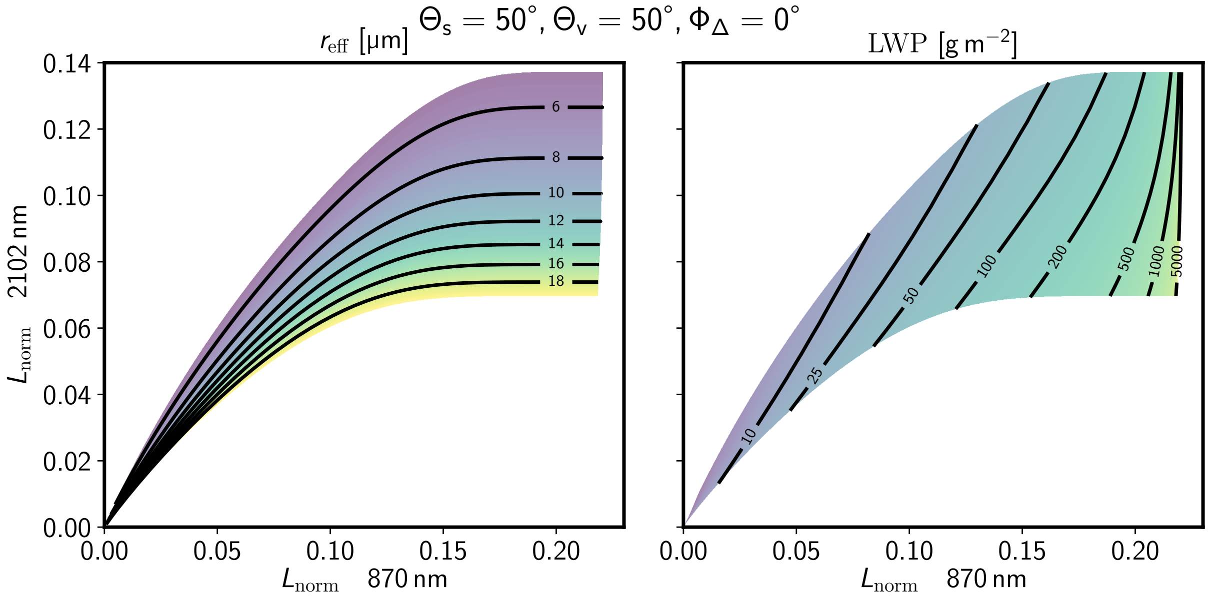

Figure 3.19: Typical dual wavelength cloud property look-up table for plane-parallel clouds. The left panel shows how the effective radius mostly affects radiance at the wavelength with larger absorption cross section, while the right panel shows that liquid water path primarily affects the wavelength with lower absorption cross section. For a large liquid water path, radiance becomes saturated and a retrieval becomes less sensitive to LWP.

approximate this limit for L_{norm} at 870 nm closely. In these cases, retrievals become insensitive to liquid water path. On the other hand, L_{norm} at 2102 nm splits up cleanly for different r_{eff} values, thus retrievals should be sensitive to effective radius for thick clouds. For small values of LWP, the reflected radiance becomes small for all wavelengths, because the cloud becomes transparent (Fig. 2.5). Accordingly, the measured radiance will depend more on the radiance of the background and less on the physical properties of the cloud, which limits sensitivity to LWP and r_{eff} for thin clouds.

The particular look up table used in this thesis has been calculated with 1D DISORT simulations. The results are tabulated for all combinations of 75 effective radii (5 μm to 20 μm), 200 liquid water paths ($1\,\frac{\mathrm{g}}{\mathrm{m}^2}$ to $10\,000\,\frac{\mathrm{g}}{\mathrm{m}^2}$, logarithmic), 23 solar zenith angles (0° to 90°), 23 viewing zenith angles (0° to 90°), and 16 differential azimuths (0° to 180°).

Tilted Bi-Spectral Retrieval

This section presents an approach to correct for non plane-parallel cloud geometry, but still using the tabulated values of LWP, r_{eff} and radiance provided as described before. If, as stated by Ewald et al. (2019), cloud surface orientation is able to explain a large amount of retrieval error in Nakajima-King type retrievals, the availability of cloud surface orientation allows to extend the classical Nakajima-King approach without moving to a full

3D retrieval method. If instead of the actual zenith direction, the cloud surface normal is interpreted as if it is the zenith direction, the cloud surface orientation can be incorporated into the retrieval. To this end, in the given plane-parallel lookup-table only the choice of Θ_v, Θ_s and Φ_Δ have to be adapted to better match the observed geometry.

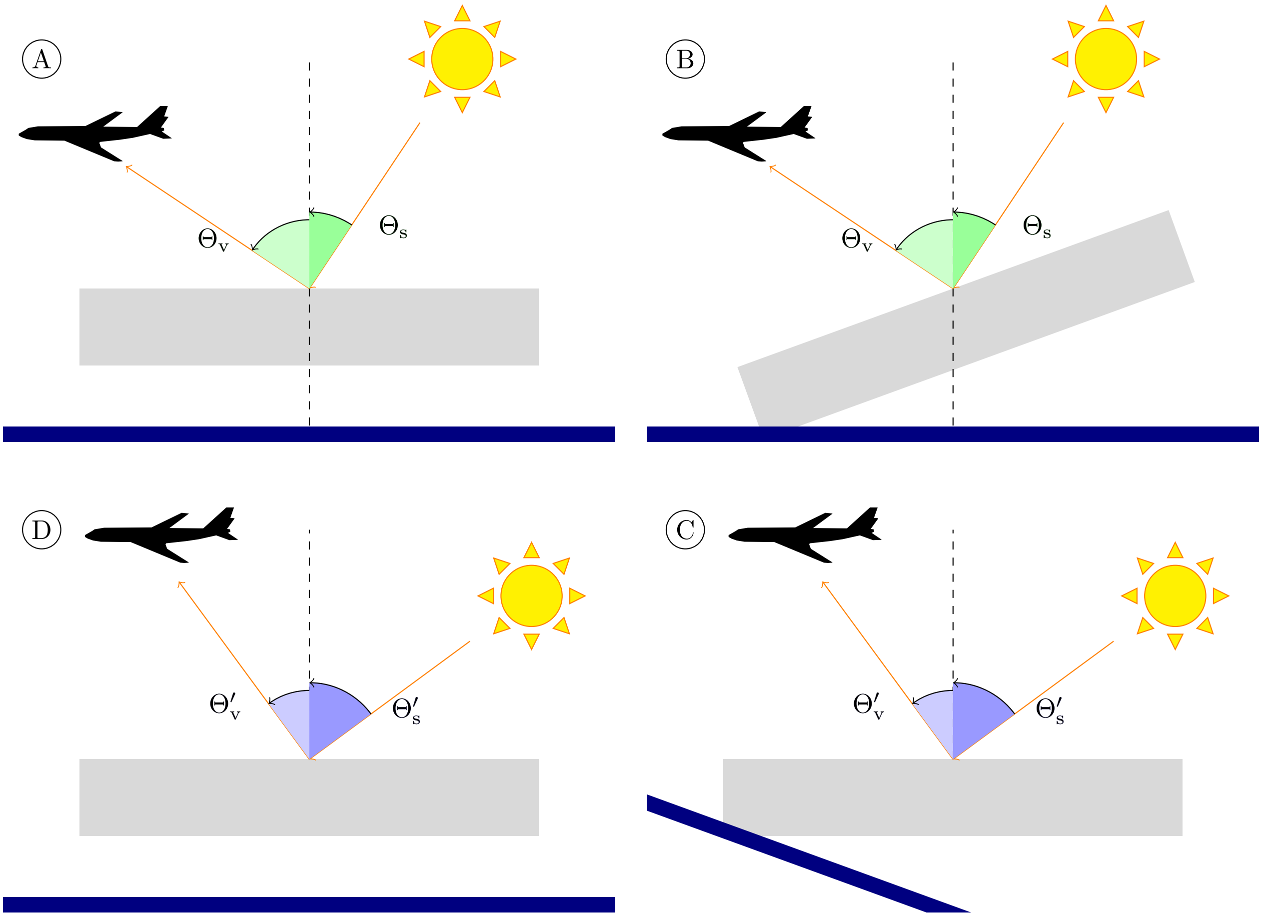

Figure 3.20: Nakajima-King geometry. A: classical plane-parallel geometry, B: actual geometry while having a tilted cloud surface, C: the same tilted geometry but in a rotated frame of reference, D: the actual setup for 1D radiative transfer calculations. The rotation of the frame of reference causes the solar and viewing zenith angles to refer to the cloud surface normal instead of the real zenith, hence they become primed values.

This idea is illustrated in Figure 3.20. Panel A shows the ideal geometry of a flat cloud surface. Θ_s denotes the solar zenith angle and Θ_v the viewing zenith angle. Stepping through the drawings in clockwise direction, B shows the actual geometry: the cloud is not flat but tilted, in this case towards the instrument. In C, the coordinate frame is rotated, such that the cloud is again horizontal, however the solar zenith angle Θ'_s and viewing zenith angle Θ'_v now refer to the local cloud surface normal and therefore are marked with a $'$. D finally shows the actual approximation: if the surface is sufficiently dark compared to the cloud, it's orientation does not matter anymore, so a surface which is flat in the new coordinate frame will do equally well. Not shown is the differential azimuth angle Φ_Δ between sun and viewing direction, on which the same transformation applies. This setup is now formally equal to the original setup A, so the look-up table calculated using the standard Nakajima-King approach can be reused. During the retrieval, the actual angles $\Theta_\mathrm{s}, \Theta_\mathrm{v}, \Phi_\Delta$ must be transformed to $\Theta'_\mathrm{s}, \Theta'_\mathrm{v}, \Phi'_\Delta$ in a preprocessing step.

Chapter 4

Results

This chapter summarizes the results of the theoretical and experimental studies of the thesis. In the first part, several 3D radiative transfer simulations of artificial clouds are performed, indicating under which circumstances bi-spectral cloud microphysics retrieval methods may work. The theoretical experiment is conducted with a particular focus on differences between the classical plane-parallel retrieval approach and the tilted approach which takes cloud surface geometry into account. The second part shows how the stereographic cloud surface retrieval method has been verified using measurements from the NARVAL-II and NAWDEX field campaigns. The chapter closes by showing how the data quality has been improved significantly with the instrument update for the EUREC^{4}A field campaign. The updated setup could be tested during a pretest campaign in May 2019 and the resulting high-resolution data allows for the reconstruction of closed cloud surface meshes which are then used in the tilted bi-spectral retrieval method for cloud microphysical properties.

4.1 When do Nakajima-King Type Retrievals Work?

The difficulty in real-world measurements is the curvature of a cloud surface and influences by neighboring clouds (Várnai and Marshak, 2003; Zinner and Mayer, 2006). Additionally, in cases of fine-structured clouds the local surface orientation is not necessarily representative for all effects on measured radiance. This section investigates to what extent a Nakajima-King like retrieval is still applicable to structured clouds.

In it's original form, a Nakajima-King (NK) type retrieval assumes a horizontal stratiform cloud layer which is observed from above. Real clouds are not perfectly homogeneous and horizontal. Cumulus clouds have finite extent and stratiform layers will always have some modulated cloud surface. To assess the applicability of NK type retrievals to more realistic clouds, several specially crafted simulated cloud scenes are investigated. Simulations are done with the 3D Monte-Carlo solvers MYSTIC and RayLi to obtain the true observable radiance values as well as with DISORT to obtain look up tables for the retrieval method. In all cases, cloud optical properties have been derived using the Mie tool of libRadtran. Cloud surface geometry is derived directly from the definition of the input data. The investigation compares both, the classical approach of a homogeneous cloud surface as well as the tilted approach (Sec. 3.5.3) using the known local cloud surface orientation. The study starts with a simple axis aligned box cloud, which is used to check basic effects of finite cloud extent. Additionally, the box cloud is rotated about a horizontal axis in order to test if the tilted retrieval approach is generally possible and consistently implemented. Afterwards, the spherical cloud example of Ewald (2016); Ewald et al. (2019) is revisited, showing a non-trivial application of the tilted bi-spectral retrieval. The section is finished by looking at a stratiform cloud with a wave on top, which adds concave cloud structures to the picture.

4.1.1 General Simulation Setup

In order to focus solely on geometrical effects, the simulations are set up in an evacuated world, i.e. without atmosphere and ground surface. The water clouds are described as homogeneous clouds of a single effective radius and binary liquid water content distribution (either 0 or a scenario dependent fixed value). The true effective radius r_{eff} is chosen to be 10 µm, which corresponds to a typical natural value, which also is well inside the bounds where the Nakajima-King approach generally works best. The cloud liquid water content is chosen to match typical values for maritime cumulus clouds, in particular also the clouds of the NARVAL-II field campaign. Following Jacob et al. (2019), the average liquid water path (LWP) during NARVAL-II of clouds was $40\,\frac{\text{g}}{\text{m}^2}$. In more than 90 % of the observed cloud area LWP has been below $100\,\frac{\text{g}}{\text{m}^2}$ and in 95 % of the observed cloud area below $200\,\frac{\text{g}}{\text{m}^2}$ (Fig. 4.1). Hess et al. (1998) state $0.44\,\frac{\text{g}}{\text{m}^3}$ for marine cumulus clouds, which would agree with an example of a raining cloud in Jacob et al. (2019, Fig. 10) during the NARVAL-I field campaign.

For the numeric experiment, the scenarios in Table 4.1 have been defined. The optical thickness τ in this table is calculated using the formulas from Section 2.1.3. These numbers indicate that the spherical cloud used by Ewald et al. (2019) will rarely be occurring in the tropical Atlantic and a lower optical thickness might be more appropriate for this region.

Table 4.1: Typical cloud water content (LWP) and the corresponding optical thickness (τ) for different cloud scenarios.

scenario	LWP $[\frac{\text{g}}{\text{m}^2}]$	τ ($r_{\text{eff}} = 10\,\mu\text{m}$)
thin cloud	20	3
average cloud	40	6
thick cloud	200	30
very thick cloud	1000	150
Ewald et al. (2019)	3333	500

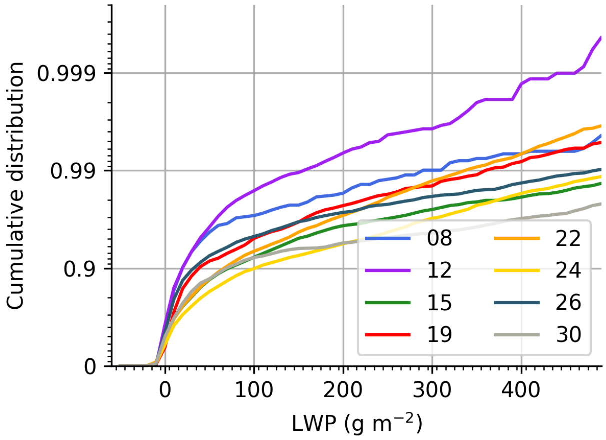

Figure 4.1: Cumulative distribution of cloud liquid water path of each flight of the NARVAL-II field campaign. Figure by Marek Jacob, personal communication, supplementary to Jacob et al. (2019).

Within this thesis, the look-up table introduced in Section 3.5.3 is used. This table is used to compare 3D and 1D forward simulations, while it also builds the basis for the NK retrievals. As the classical and the tilted retrieval differ only in the used observation angles, the table can be used for both methods.

4.1.2 Box Cloud

The most obvious difference between theoretical one dimensional clouds and real world clouds is their finite size. In order to investigate in which ways clouds of finite horizontal extent behave differently from clouds with infinite horizontal extent, a set of single box clouds has been simulated. The setup is illustrated in Figure 4.2. In this setup, only radiance from the horizontal cloud top surface is investigated, so in this case, no distinction between the classical and the tilted retrieval approach is necessary. Conceptually, if a cloud has finite horizontal extent, radiance can be lost or gained through the side faces. However, the horizontal transport is not considered by 1D models. Accordingly, the expectation is that larger clouds are explained better by 1D theory than smaller clouds. This leads to the question what the actual meaning of "large" would be in this case. In order to investigate this further, the aspect ratio $a = w/h$ of the cloud has been modified between 0.1 and 10. The vertical liquid water path is varied according to Table 4.1.

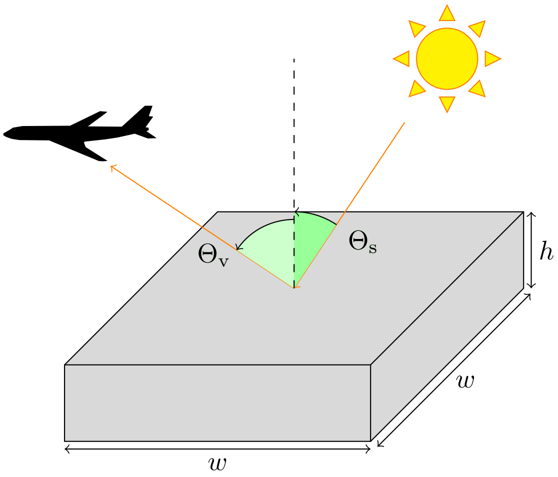

Figure 4.2: The setup for the box cloud test case. Θ_s is the solar zenith angle, and Θ_v is the viewing zenith angle. The cloud is cuboidal and has a horizontally aligned square base face with edge length w. Its aspect ratio is defined as $a = w/h$. Only radiance from the central point of the upper cloud surface is observed.

The setup contains a notable detail: the geometric extent of the cloud is not relevant for the simulation. However, an increase of liquid water path can equally well be interpreted as an increase of liquid water content or as an increase of the overall cloud dimensions. As for all investigated cases, only radiance from the central point of the upper cloud surface is observed, it might be expected that an increase in overall cloud dimensions corresponds to less influence of the cloud sides. This would correspond to a reduced influence of the finite cloud extent with increasing liquid water path. This theory is however not supported by the simulation results.

Figure 4.3 shows the simulation results for this case. The retrieval of effective radius is largely unaffected by a change in liquid water content as well as by a change in aspect ratio. For high values of LWP, the retrieval of liquid water path generally produces large errors. This can be expected as in this region, changes in LWP produce only very small changes in radiance (see Figure 3.19). Apart form this, the retrieval of LWP shows an interesting behaviour. For a cloud aspect ratio of less than about 4, the retrieval underestimates the true LWP considerably. This can be expected, as LWP is mainly derived from observed cloud brightness. As demonstrated in Figure 1.2, a cloud of finite extent appears darker than a cloud of infinite extent as it is loosing radiance through it's side faces. However, the amount of underestimation is largely unaffected by the true liquid water path of the cloud and the effect is even reduced for very small values of true LWP. This contradicts the intuition stated in the beginning that clouds of large geometrical extent are less affected by effects of finite cloud extent. In stead, it is really the cloud aspect ratio, which determines the influence of finite cloud extent on the retrieval result.

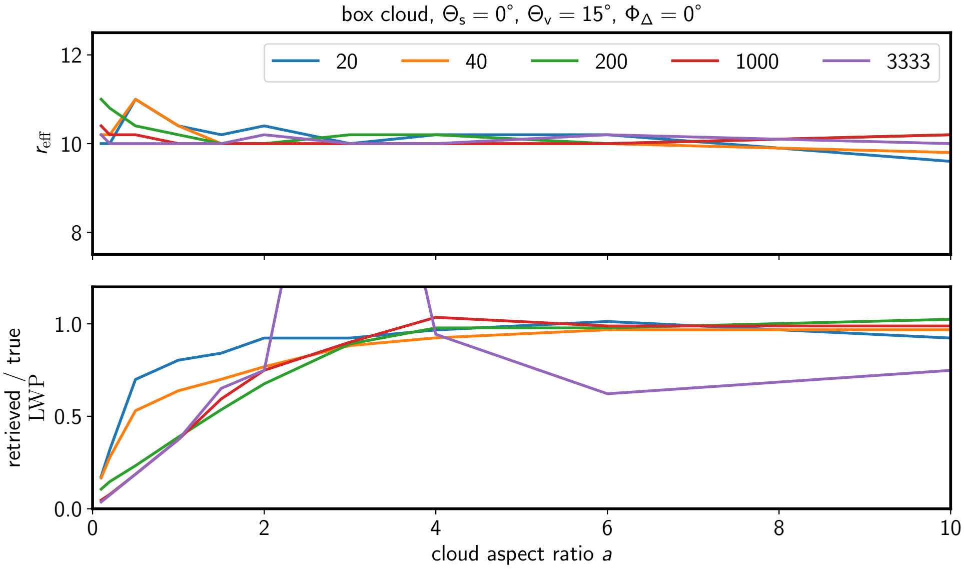

Figure 4.3: Simulated effective radius and LWP in the box cloud experiment for one sensor-sun geometry (solar zenith angle $\Theta_s = 0$, viewing zenith angle $\Theta_v = 15°$, azimuth angle difference $\Phi_\Delta = 0°$). Colored lines correspond to the true LWP values of different cloud scenarios listed in Table 4.1.

The declining influence of cloud aspect ratio for very low values of true LWP can be explained by the amount of scattering events. For low solar zenith angles and low viewing zenith angles, the finite cloud extent can only affect light paths with more than one scattering as otherwise no horizontal radiance transport will occur. For low LWP, the amount of scatterings is low as well and the fraction of light paths with only one scattering is increased correspondingly.

4.1.3 Tilted Box Cloud: Consistency check of Tilted Nakajima-King Retrieval

In order to actually investigate the tilted retrieval approach introduces in Section 3.5.3, the following examples will also contain cloud surfaces which are not axis-aligned. As baseline case, a consistency check between 3D Monte-Carlo simulations of a rotated cloud and the look-up table has been done. The cloud is again defined as cuboid with square base face and horizontal to vertical aspect ratio $a = w/h$, but in this case, it is rotated about the horizontal axis with angle α. The setup is illustrated in Figure 4.4 and is equivalent to the setup discussed in Figure 3.20.

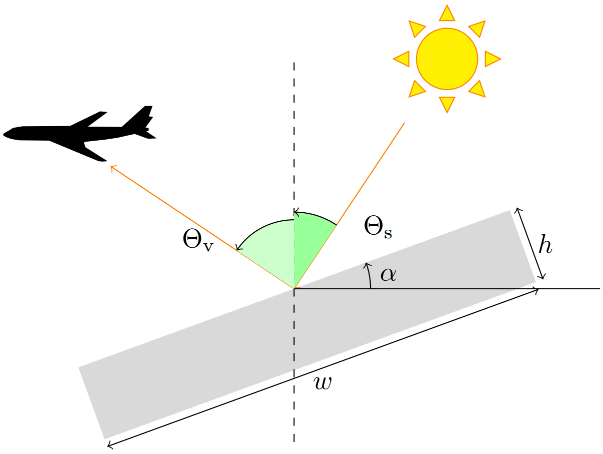

Figure 4.4: The setup for the tilted Nakajima-King retrieval consistency check. Θ_s is the solar zenith angle, Θ_v is the viewing zenith angle, and α is the surface tilt angle. The cloud is cuboidal and has a square base face (along w and perpendicular to the drawing plane). Its aspect ratio is defined as $a = w/h$.

As this setup is intended to verify the consistency between 3D simulations, the look-up table and the assumptions of the tilted retrieval, finite cloud extend is not considered and accordingly the aspect ratio a has been set to a large value of 1000. The results have been computed using the RayLi solver with the cloud set up using the convex polyhedral grid. MYSTIC has been used to verify that the setup works as intended by computing a reduced number of examples with the tilted surface approximated by a voxelized version. Viewing zenith angle Θ_v, solar zenith angle Θ_s, surface tilt angle α and liquid water path LWP have been varied between simulations as indicated by the x-axes in Figure 4.5. Cases in which the cloud would be illuminated from behind have not been examined.

The figure shows the retrieved effective radius and the fraction of retrieved to true liquid water path for each simulated scene. As expected, the tilted retrieval approach performs much better than the plane parallel assumption. In the base case ($\alpha = 0$), the simulated cloud actually is horizontal and both retrieval methods are equivalent and consequently

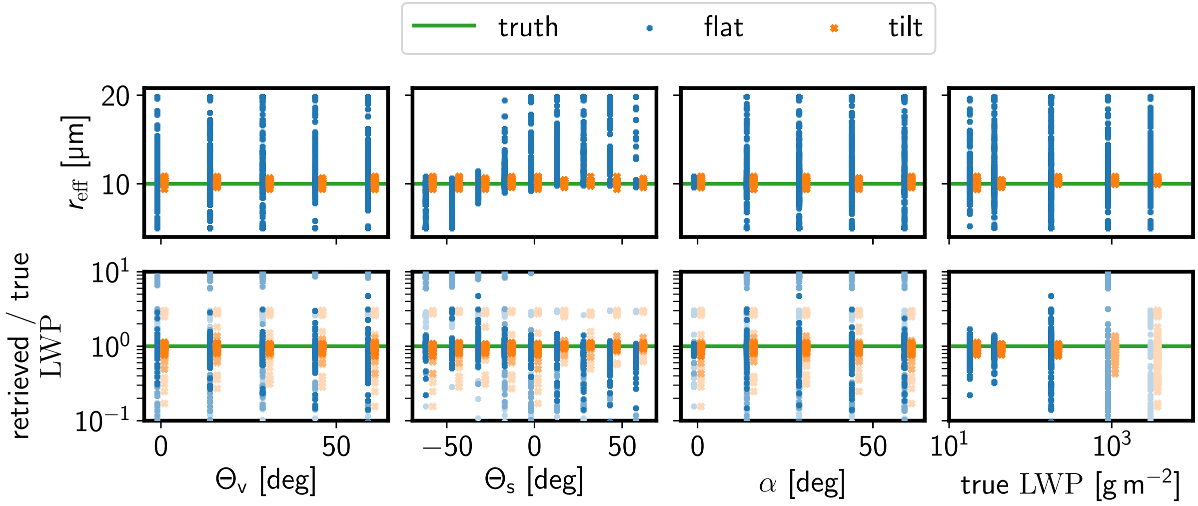

Figure 4.5: r_{eff} and LWP retrieval results for various different runs of the tilted cloud example. Blue shows the classical retrieval, orange shows the tilted retrieval. The results have been dithered aroud the true parameter value along the x-axis, to improve visibility of both retrieval methods. Due to the density of the look-up table at high values of LWP (Sec. 3.5.3), the LWP retrieval is expected to fail for large values of LWP, thus the results for LWP $\geq 1000\,\frac{\mathrm{g}}{\mathrm{m}^2}$ have been shaded.

return equal results. Even is this case, some scatter is left in the retrieval results. This scatter can be observed in the results of both Monte-Carlo models and is not due to simulation noise. This is supported by computing an estimate of the standard deviation of the simulated radiance. The differences originate from slightly different results between forward simulations using the DISORT method and Monte-Carlo results. These differences are however not of practical concern, as they are smaller than the expected measurement uncertainties of the specMACS instrument.

As shown in Section 3.5.3, due to the saturation in radiance values for clouds with large liquid water path, the retrieval approach can not work for large values of LWP. This expected behaviour is also clearly visible for the LWC $= 1000\,\frac{\mathrm{g}}{\mathrm{m}^2}$ and LWC $= 3333\,\frac{\mathrm{g}}{\mathrm{m}^2}$ cases, which have been shaded for this reason. Also, as expected the retrieval stays sensitive for r_{eff}, even at large values of LWP.

For clouds which are actually tilted, the retrieval results of the *flat* and *tilt* cases separate. The classical plane parallel retrieval essentially becomes insensitive to effective radius and much less sensitive to liquid water path. Figure 4.6 shows that even for moderate and known values of $\Theta_v = 15°$ and $\Theta_s = 15°$, a variation in surface tilt angle can lead to large errors in the retrieved quantities. The retrieval of r_{eff} is biased towards smaller values if the surface is tilted towards the sun ($\Theta_s < 0$) and biased towards larger values if the surface is tilted away from the sun ($\Theta_s > 0$).

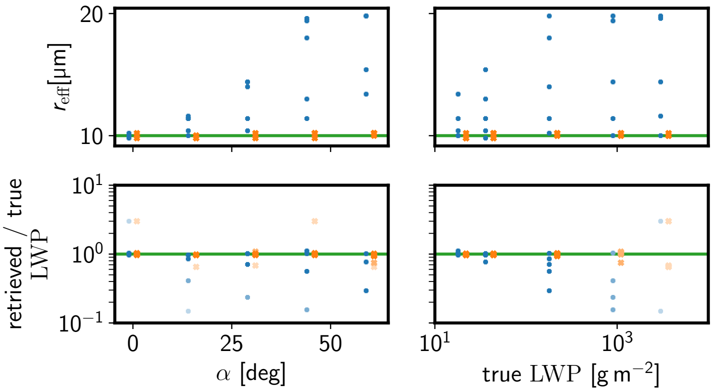

Figure 4.6: Subset of Figure 4.5: The cloud surface tilt angle is varied for fixed values of $\Theta_\mathrm{v} = 15°$ and $\Theta_\mathrm{s} = 15°$.

Overall, these results are as expected. In the end, apart from implementation and numerical details, for these cases the tilted retrieval method is only a cyclic series of radiative transfer calculations and coordinate transformations and should return perfect results, while for the flat retrieval method, this could be called comparing apples and oranges and of course should return worse results. But this consistency check shows that knowledge of the surface orientation can in principle lead to fundamental improvements of a dual wavelength cloud property retrieval and that the different simulations have been set up consistently.

4.1.4 Spherical Cloud

The spherical cloud provides a useful case to study clouds with varying surface orientations. A similar case has already been investigated by Ewald et al. (2019), which supports the idea to use cloud surface orientation to aid the bi-spectral retrieval methods. In order to further simplify the setup, the liquid water content at the cloud cloud boundary is not gradually reduced as described in Ewald (2016, Fig. 4.8), but shows a step change from full to zero LWC. The geometry for the setup is illustrated in Figure 4.7. In this case, due to the symmetry of the setup, the viewing zenith angle Θ_v is not needed. In order to study the behaviour across the various locations on the cloud surface, the location of the observer is varied along the x-axis.

While the step change creates an unambiguously defined cloud surface, it also requires a geometrically well resolved cloud boundary. The basic Cartesian MYSTIC grid can not resolve the cloud boundary in great detail as an unrealistic high amount of memory would be needed. Instead, the spherical model of MYSTIC is used. In this mode, the Earth is simulated as a sphere surrounded by an atmosphere. If the earth is defined as a very small sphere (0.01 m in this case), a 1D cloud from surface to top of atmosphere is as good as a 3D spherical cloud in vacuum. By alternating the surface albedo between 0 and 1, it

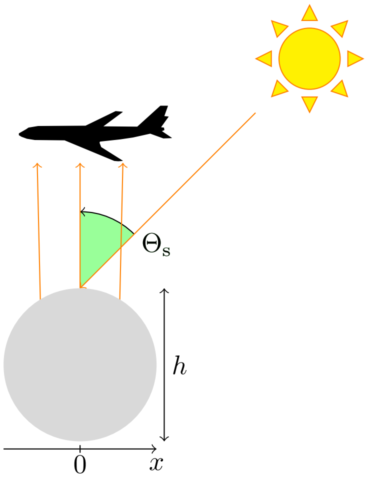

Figure 4.7: The setup for the spherical cloud test case. Θ_s is the solar zenith angle. The cloud is spherical with diameter h. The reference $\mathrm{LWP}_\mathrm{ref}$ is measured vertically through the center of the sphere. Accordingly $\mathrm{LWC} = \mathrm{LWP}_\mathrm{ref}/h$.

was verified that the little solid sphere has virtually no impact on the radiative properties of the simulated cloud. RayLi implements a spherical grid, so it is possible to directly simulate spherical clouds as well.

Figure 4.8 shows the results of retrieving r_eff and LWP from selected synthetic spherical clouds. The left side of each plot (negative x values) shows parts of the cloud which are tilted away from the sun, the right side of each plot (positive x values) shows parts of the cloud which are tilted towards the sun. The upper two rows show the retrieval results for the classic "flat" retrieval approach and the tiled approach. The bottom row additionally shows the simulated normalized radiance values.

As already shown by Ewald et al. (2019), the measured radiance is brightest at the surface location which is oriented directly towards the sun. For r_eff, the classical retrieval approach works well at this location. At other surface locations, which are tilted away from the sun, radiance decays faster at the wavelength with stronger absorption (2102 nm) compared to 870 nm, leading to an overestimation of the effective radius in the classical retrieval approach. The results also show that this effect can largely be compensated by the tilted Nakajima-King approach, which results in very accurate retrievals of effective radius at most locations over the simulated scene. At some locations, the flat retrieval approach returns slightly better results than the tilted approach, but the differences are small compared to the errors of the flat retrieval at larger cloud surface tilt angles. On the far left side ($x \approx -1$), the tilted retrieval approach ceases to work. At these locations, the sun is located almost perpendicular to the cloud surface normal, such that large fractions of the measured radiance actually originate from transmission through the cloud in stead of reflection at the cloud surface. As the transmission regime is not considered by the

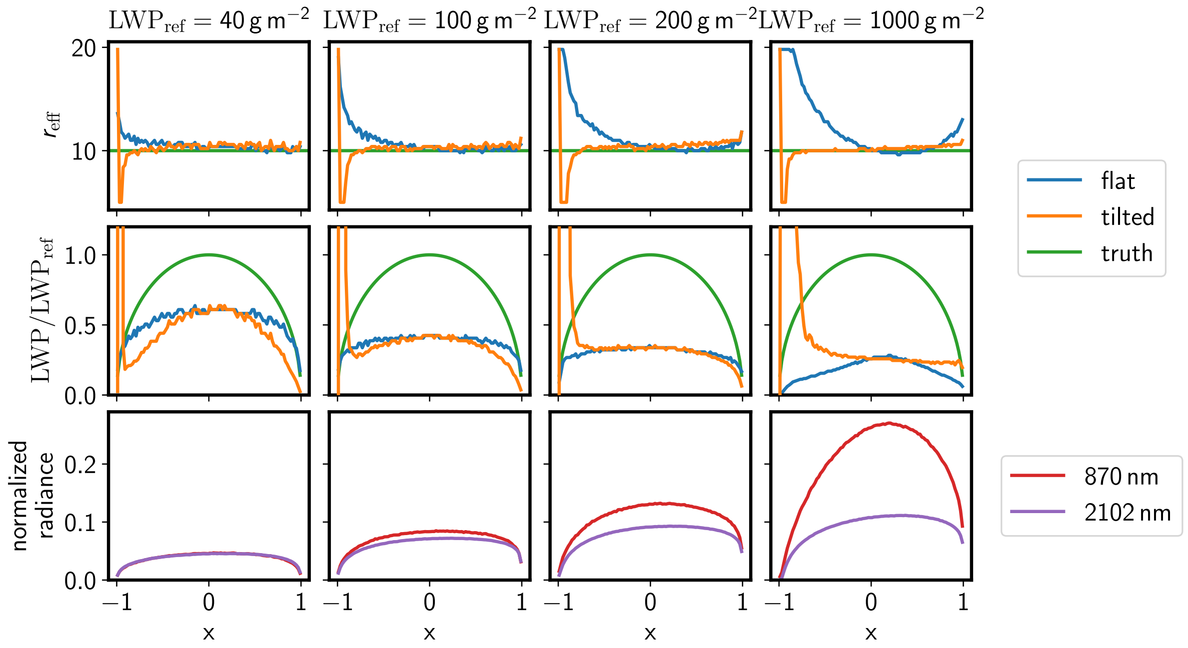

Figure 4.8: Retrieval results for spherical cloud case. The top row shows retrieval results for the effective radius r_eff, the middle row shows results for liquid water path LWP and the bottom row shows the simulated normalized radiance for reference.

simulations for the look-up table, the retrieval can not be expected to work properly in these cases. Due to the keep out zone of the shadow mask (Section 3.5.1), that mask does not only flag actually shadowed cases (sun behind the cloud surface), but also cases in which the sun enter the cloud at very shallow angles. Thus, the cases in which the tilted retrieval approach fails can be flagged and excluded from retrieval results of real measurement data.

The retrieval of liquid water path shows a different picture. As already discussed using the box cloud (Section 4.1.2), the finite cloud extent mostly affects the retrieval of liquid water path. In the particular case of a spherical cloud, the aspect ratio is 1, so according to the results of the box cloud experiment, the LWP is expected to be underestimated to values between 0.3 and 0.6, depending on the true liquid water path of the cloud, with stronger underestimation at larger LWP. The findings from the box cloud case are generally reproduced by the spherical cloud. Apart from that, no universal improvement can be found by the application of the tilted retrieval approach. Furthermore, the breakdown of the tilted retrieval approach for shadowed and almost shadowed parts of the clouds is present in the liquid water path retrieval as well, such that it becomes even more important do exclude these zones from a retrieval on real measurement data.

4.1.5 Wave Cloud

The goal of the wave cloud model is to investigate the scale at which cloud surface orientation is relevant to the retrieval of cloud droplet size. To do so, the synthetic cloud should have a constant slope at the observed location but should transform smoothly from an almost flat cloud to a tilted cloud only by changing scale. The first derivative of the Gaussian is a model which fits this purpose very well:

$$g'(x) = -\frac{x}{\sqrt{2\pi\sigma^3}} e^{-\frac{x^2}{2\sigma^2}} \tag{4.1}$$

Using this analytic expression, the upper cloud surface can be modified in a continuous way, allowing for a change between a perfectly flat cloud and a tilted part of the cloud. Using normalization and scaling, the parameters of this function are changed such that they are more physically understandable:

$$f_{h,\alpha}(x) = -\frac{x}{\tan\alpha} e^{-\frac{x^2}{2eh^2\tan^2\alpha}} \tag{4.2}$$

In this form, the height h and the angle α of the wave can be set independently. Figure 4.9 shows the schematic setup of this experiment. Additional to the parameters h and α of the wave, H and w determine the overall cloud size. In all investigated cases, the cloud extent perpendicular to the drawing plane has also been set to w, creating a square cloud base. For the experiments, w has been set to a large value of $1000H$, such that effects of finite horizontal cloud extent are negligible.

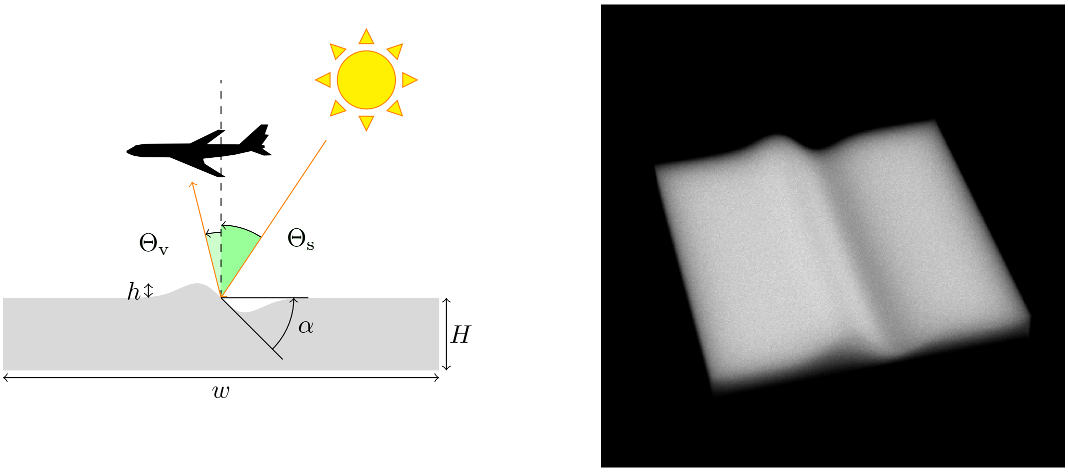

Figure 4.9: Wave cloud experiment setup. The left panel shows a schematic of the scene, including its most important parameters. The right panel shows a synthetic photo of the setup. Even though all parts of the upper cloud surface are illuminated, differences in cloud surface brightness are visible. For illustrative purposes and unlike the other simulations, the horizontal extent w of the pictured cloud has been set to a small value.

In order to study the influence of surface orientation, the surface orientation has to be represented accurately in the model. However, explicit intersection code for the Gaussian derivative is neither fast nor reusable, so in stead the convex polyhedral grid is used again. The cloud volume is split into columnar boxes with tilted tops as shown in Figure 4.10. In order to reduce the number of required boxes, an optimization algorithm based on Ramer (1972) and Douglas and Peucker (1973) is used. Using this optimization it is possible to represent the cloud top with a maximum vertical error of $10^{-5}H$ using only 1113 boxes. This resolution is well below the size of one optical thickness, even for the thickest investigated clouds.

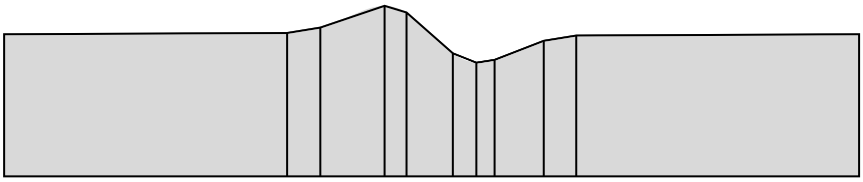

Figure 4.10: Wave Cloud using polyhedral grid: The idealized wave cloud (gray) can be used in a radiative transfer simulation by discretization into a polyhedral grid. For the illustration, a relatively coarse grid, optimized to $0.1H$ is used. Even though, differences between the gray shape and the black line are barely visible.

Figure 4.11 shows the characteristic features of the wave on top of the simulated cloud for a series of different wave heights h. For $h = 0$, the wave cloud converges to a horizontal cloud, while for $h \to \infty$, that wave cloud becomes a tilted cloud with tilt angle α. The slope of the cloud at location A stays constant during this transition. The following discussion focusses on simulated observations at points A and B. While A is located at the same position for every cloud scale, B is moved between the simulations, such that it always points at the location where the cloud top is elevated to $h/2$.

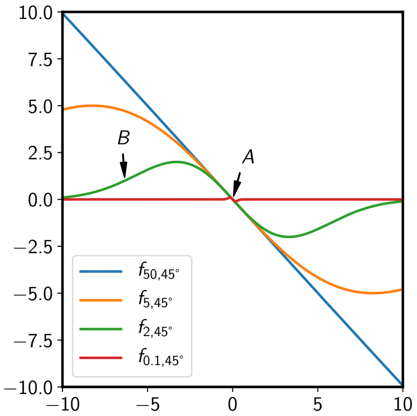

Figure 4.11: Illustration of the wave cloud top shape including observation locations A and B. The extremal cases $f_{0.1,45°}$ and $f_{50,45°}$ appear almost as a straight line.

The experiment is intended to test the influence of the size of a wave on microphysical retrieval results. The expectation of the outcome is that a very small wave should not affect the plane-parallel assumption and thus, a flat retrieval will return best results, while a large wave behaves as a tilted cloud, so the tilted retrieval will return best results in that case. In order to test this assumption, the angle α is kept constant while the scale, described by the relative wave height h/H, is changed corresponding to the different colored lines in Figure 4.11. The simulated observer is pointed at the point indicated as A, at which the local surface tilt angle is always α, independent of the scale of the wave. Retrievals are again performed for the assumption of a flat cloud and a cloud tilted to the angle of α.

Figure 4.12 shows results for the observer at location A. Depending on the solar zenith angle, the results of this experiment show a qualitatively different behaviour. Two prominent cases are illustrated using the Θ_s angles 0° and 45°. In both cases, the behavior of r_{eff} is qualitatively as expected. For a small wave, the simulated cloud is essentially flat and, accordingly, a retrieval assuming a flat cloud perfectly retrieves the correct value of 10 µm. For larger wave scales, the flat retrieval approach diverges from the true result while the tilted retrieval approach converges towards the correct solution. However, independent of the solar zenith angle, the tilted retrieval underestimates the true effective radius slightly. This may be explained by additional radiance which is reflected from the rising slope, present to the right of the observed location. The retrieval of LWP performs very differently comparing the two identified Θ_s cases. For $\Theta_s = 0°$, the flat retrieval approach always performs better than the tilted approach. This particularly interesting as the retrievals of r_{eff} and LWC are coupled and the tilted approach performs reasonably well for the effective radius. Nonetheless, an overestimation of liquid water path is consistent with the possibility to receive additional radiance form the rising slope as argued for r_{eff}. The situation is reversed for $\Theta_s = 45°$, where the flat retrieval quickly diverges, but the tilted retrieval performs very well, except for the larges LWP value.

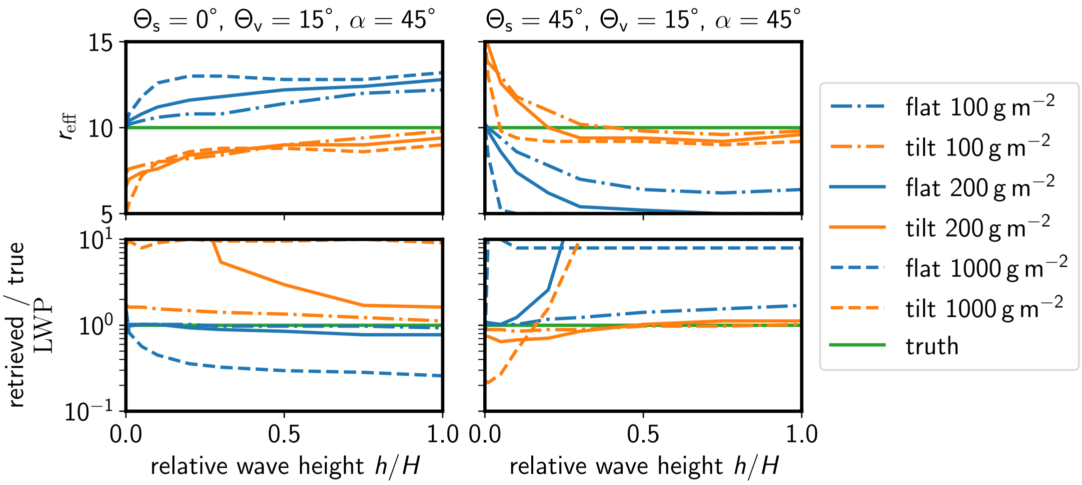

Figure 4.12: Wave cloud retrieval results for an observer at location A.

Figure 4.13 shows the same experiment repeated for an observer at location B. This case is also set up in a way which keeps the local slope of the cloud surface constant. The notable difference is the lack of the opposing slope, which supposedly is responsible for the errors discussed in the previous case. In this case, these differences are indeed missing, which confirms the argument.

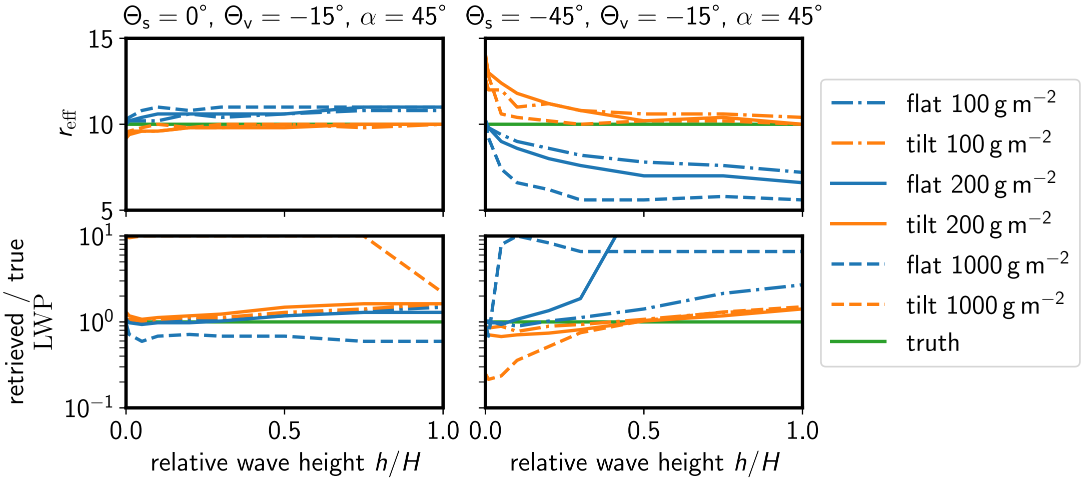

Figure 4.13: Wave cloud retrieval results for an observer at location B.

4.1.6 Conclusions on Retrieval Applicability

This section covered a series of theoretical experiments investigating the performance of bi-spectral retrievals for different geometric situations. The focus is solely on the influence of cloud and observation geometry, leaving out other important possible error sources, including ground surface albedo or other atmospheric constituents like aerosols or trace gases. The initial box cloud experiment shows that finite cloud geometry in general can severely influence the retrieval of liquid water path, while at least in the central part of the observed cloud, the retrieved effective radius remains largely unaffected. The following experiment shows that a tilted cloud surface can lead to very large errors for the classical flat retrieval approach, both in the retrieval of r_{eff} and LWP. If the cloud surface orientation is known, these errors can be corrected. The spherical cloud experiment shows that it is possible to transfer the retrieval correction from planar to curved cloud surfaces successfully, confirming the initial experiment by Ewald et al. (2019), which lead to the development of the tilted retrieval approach. However, this only helps in the retrieval of r_{eff} as the finite cloud extent affects the retrieval of LWP in similar ways as in the first case. The wave cloud experiment embeds the structured cloud surface into a larger surrounding and demonstrates that it is not possible to fully correct for three dimensional effects based on the local surface orientation. The situation becomes even more complicated if the surface is illuminated indirectly. A remarkable result of the last experiment is that for low solar zenith angles, the application of the tilted retrieval approach can reduce the LWP retrieval accuracy for stratiform clouds. For a lower standing sun, the effect is reversed and the tilted retrieval generally improves the accuracy.

The application of one dimensional approximations in bi-spectral retrievals remains a challenging topic. This investigation shows that the use of surface orientation may improve retrieval results in some cases. For more complicated cloud scenes, the tilted approach may lead to unintuitive results and has to be applied with care.

4.2 Verification of the Stereo Method

This section contains work which has already been published in Atmospheric Measurement Techniques (AMT) by Kölling et al. (2019).

In order to verify the accuracy of the stereographic cloud geometry retrieval, several experiments have been made. Sensor missalignment or remainig lens distortion would lead to tilted or curved average retrieved cloud top heights. The experiment of Section 4.2.1 shows that this is barely the case. In Section 4.2.2, the mean absolute accuracy is assesed using cloud top heitgs derived from a proven lidar system. As an interesting side product, cloud movement has been retrieved and used for quality assurance during the stereographic retrieval. Section 4.2.3 compares the retrieved cloud movement with an ECMWF reanalysis of the horizontal wind.

4.2.1 Across Track Stability and Signal Spread

Errors in the sensor calibration could lead to systematic errors in the retrieved cloud height with respect to lateral horizontal distance relative to the aircraft (perpendicular to flight track). In order to assess these errors, data from a stratiform cloud deck observed between 09:01:25 and 09:09:00 UTC during NAWDEX flight RF11 on 2016 Oct 14 has been sorted by the average across track pixel position. While the cloud deck features a lot of small scale variation, it is expected to be almost horizontal on average. As explained in Section 3.3.1, the orientation of the camera with respect to the aircraft has been determined independently using landmarks. Deviations from the assumption of a horizontal cloud deck should thus be visible in the retrieved data and are counted as additional retrieval uncertainty in this analysis. During the investigated time frame, 260360 data points have been collected using the stereo method. The vertical standard deviation of all points is 47.3 m, which includes small scale cloud height variation and measurement error. Figure 4.14 shows a 2D histogram of all collected data points. From visual inspection of the histogram, apart from about 50 px at the sensor's borders, no significant trend can be observed. To further investigate the errors, a 2$^{\text{nd}}$-order polynomial has been fitted to the retrieved heights. This polynomial is chosen to cover the most likely effect of sensor mis-alignment which should contribute to a linear term and distortions in the optical path which should contribute to a quadratic term. The difference between left and right side of the sensor of 21 m corresponds to less than 0.1° of absolute camera misalignment and the curvature of the fit is also small compared to the overall dimensions of the observed clouds.

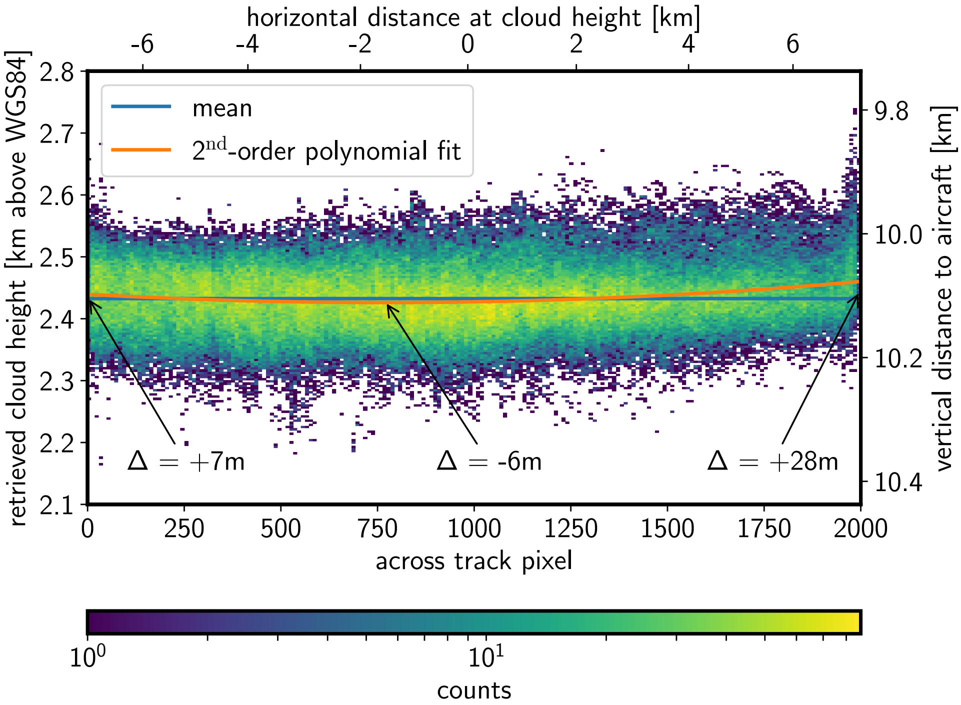

Figure 4.14: In the time from 09:01:25 to 09:09:00 UTC during NAWDEX flight RF11 on 2016 Oct 14, a stratiform cloud deck has been observed. The parabolic fit shows that a small systematic variation can be found beneath the noise (which is due to small scale cloud height variations and measurement uncertainties). Compared to the overall dimensions of the observed cloud (≈ 14 km) and the uncertainty of the method, these variations are small. It may still be noted, that data from the edges of the sensor (≈ 50 px on each side) should be taken with care.

4.2.2 Lidar Comparison

Cloud top height information derived from the WALES lidar (Wirth et al., 2009) is used to verify the bias of the described method. While the stereo method provides P_{CS} at arbitrary positions in space, the lidar data is defined on a fixed grid ("curtain") beneath the aircraft. To match lidar measurements to related stereo data points, we collect all stereo points which are horizontally close to a lidar measurement. This can be accomplished by defining a vertical cylinder around the lidar beam with 150 m radius. Every stereo derived point which falls into this cylinder with a time difference of less than 10 s is considered as stereo

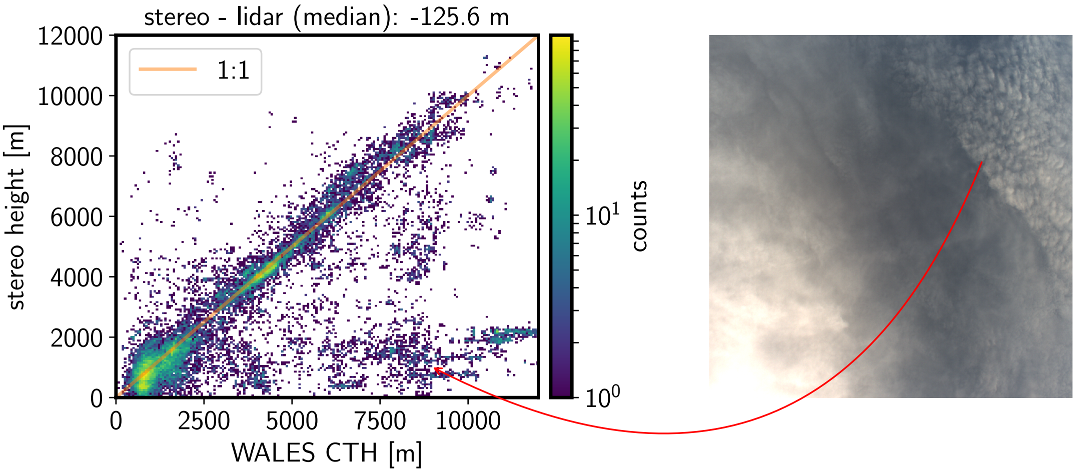

Figure 4.15: Comparison of cloud top height, measured with the WALES lidar and the stereo method. The most prominent outliers, present in the region of high lidar CTH and low stereo height can be attributed to thin, mostly transparent cirrus layers and cumulus clouds below, illustrated by a scene from NAWDEX RF10 (2016-10-13 10:32:10 UTC). While the lidar detects the ice clouds, the stereo method retrieves the height of the cumulus layer below.

point related to the lidar measurement. As the (almost) nadir pointing lidar is observing cloud top heights only, we use the highest stereo point inside the collection cylinder. The size of the cylinder is rather arbitrary but the particular choice has reasons: the aircraft moves at a speed of approximately 200 $\frac{\text{m}}{\text{s}}$ and the data of the lidar system is available at 1 Hz and averaged over this period. Any comparison between both systems should therefore be in the order of 200 m horizontal resolution. Furthermore, data derived from the stereo method is only available where the method is confident that it worked. Thus not every lidar data point has a corresponding stereo data point. Increasing the size of the cylinder increases the count of data pairs, but also increases false correspondences. The general picture however remains unchanged.

Figure 4.15 compares the measured cloud top height from the WALES lidar and the stereo method, visually showing a good agreement. However its quantification in an automated manner and without manual (potentially biased) filtering proves to be difficult. Part of this difficulty is due to the cloud fraction problem, which is explained by (Stevens et al., 2019), basically stating that different measurement methods or resolutions will always detect different clouds. This is also indicated in Figure 4.15 on the right: the stereo method detects the lower cumulus cloud layer due to larger contrasts while the lidar observes the higher cirrus layer, leading to wrong cloud height correspondences while both methods are supposedly correct. Filtering the data for high lidar cloud top height and low stereo height, reveals that the lower right part of the comparison can be attributed almost exclusively to similar scenes. Further comparison difficulties arise from collecting corresponding stereo points out of a volume which might in fact include multiple (small) clouds. Considering all these sources of inconsistency, only a very conservative estimate of the deviation of lidar and stereo values can be derived from this unfiltered comparison. The median bias between lidar and stereo method is approximately 126 m for all compared flights, indicating lower heights for the stereo method. As the lidar detects cloud top heights with high sensitivity and the stereo method relies on image contrast which is predominantly present at cloud sides, this direction is expected.

Further manual filtering indicates that the real median offset is likely in the order of 50 m to 80 m, however this cannot be shown reliably. Quantifying the spread between lidar and stereo method yields no meaningful results for the same reasons.

4.2.3 Wind Data Comparison

An important criteria that we use to identify reliable tracking points is based on the assumption that the observed movement of the points can be explained by a smooth transport due to a background wind field. The thresholds for this test are very tolerant, so the requirements for the accuracy of the retrieved wind field are rather low. However, a clear positive correlation between the observed point motion and the actual background wind would underpin this assumption substantially. In order to do so, we compare the stereo wind against an ECMWF reanalysis in a layer in which many stereo points have been found.

In the following, the displacement vectors of every track have been binned in time intervals of 1 min along the flight track and 200 m bin in the vertical. To reduce the amount of outliers, bins with less than 100 entries have been discarded. Inside the bins, the upper and lower 20 % of the wind vectors (counted by magnitude) have been dropped. All remaining data has been averaged to produce one mean wind vector per bin. In Figure 4.16 the horizontal component of these vectors is compared to ECMWF reanalysis data at about 2000 m above ground with horizontal sampling of 0.5°. The comparison shows overall good agreement according to our goal to consider a quantity in the stereo matching process which roughly behaves like the wind. The general features of wind direction and magnitude are captured. Deviations may originate from multiple sources including the time difference between reanalysis and measurement, representativity errors and uncertainties of the measurement principle. These results corroborate the assumption that the observed point motion is related to the background wind and filtering criteria based on this assumption can be applied.

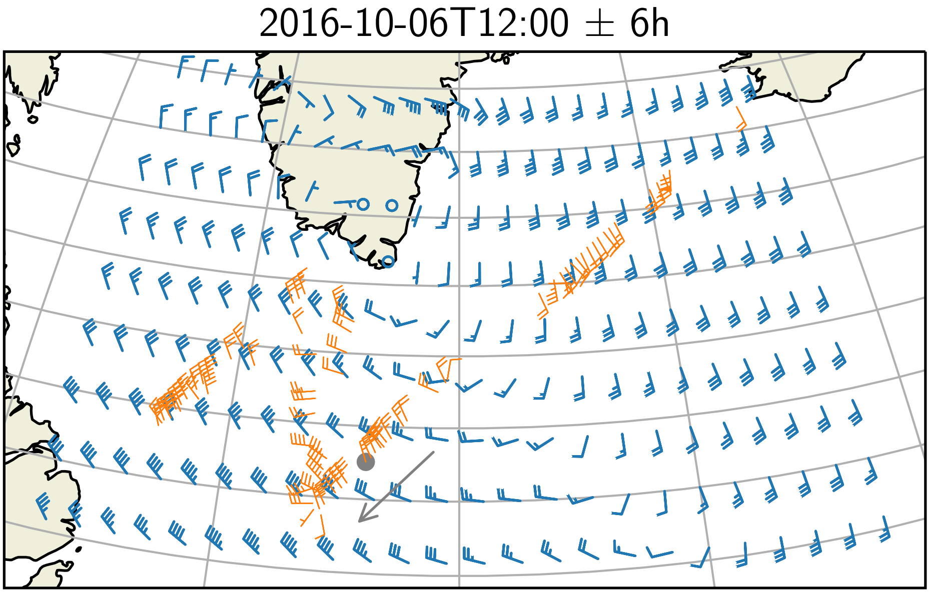

Figure 4.16: Horizontal wind at about 2000 m above ground. Comparison between ECMWF reanalysis (blue) and stereo derived wind (orange). Comparing grid points with co-located stereo data, the mean horizontal wind magnitude is $15.1\,\frac{\mathrm{m}}{\mathrm{s}}$ in ECMWF and $13.4\,\frac{\mathrm{m}}{\mathrm{s}}$ in the stereo dataset. This amounts to a difference of $(1.7 \pm 4.5)\,\frac{\mathrm{m}}{\mathrm{s}}$ in magnitude and $(6.0 \pm 33.0)^{\circ}$ in direction. The shown deviations are standard deviations over all grid points with co-located data. The gray dot and arrow mark the location and flight course corresponding to Figure 3.14.

4.3 Improved Data Quality During EUREC^{4}A Pretest

While measurements during the NARVAL-II and NAWDEX field campaigns provided valuable test data for the development of the presented stereographic method, the image quality was suboptimal. In preparation to the EUREC^{4}A field campaign, which will take place in early 2020, some test flights have been performed in May 2019 with the updated instrument payload. The campaign was the first opportunity for the specMACS system to test the polarization resolving cameras, including an upgraded exposure control system.

The first subsection briefly gives and overview about the performed flights and the corresponding cloud situation. Afterwards, it is shown how the stereographic cloud surface retrieval quality has been improved using the updated measurement system. Finally, the tilted bi-spectral retrieval approach is tested on this dataset.

4.3.1 Flights and Cloud Situation

Day time flights have been performed on 14, 16 and 17 of May 2019. An overview on the cloud situation during these days is given in Figure 4.17. The flight on May 14 was intended to check electromagnetic compatibility of the instrument and aircraft setup. As such, flight routing was to a restricted airspace in southern Germany, where a series of triangles has been flown. On that day, the sky was covered with many small cumulus clouds, which are ideal to test the cloud surface reconstruction method and additionally allowed to find some fix points on the ground for absolute camera attitude calibration (by Weber, 2019). Approximately the first half of the flight has been used to optimize the automatic exposure control system of the newly installed polarization resolving cameras. During the second half, the system worked stably and generated valuable test data for cloud surface reconstruction. The flight on May 16 was intended to check the scientific instrumentation and lead towards the North Sea and back. On that day, almost all of Germany has been overcast with a large stratocumulus deck, partly covered with some cirrus clouds in the mid to north eastern part of the country. Thus, especially on the more westerly track back to Oberpfaffenhofen, the test flight provided stable measurement conditions for cloud microphysics retrievals including the bi-spectral method as well as methods based on glory and cloudbow. Finally, the aim of the flight on May 17 has been an Aeolus satellite underpass. As the southern part of Germany was mostly cloud free, that day has also been used to obtain further ground reference points for absolute camera attitude calibration.

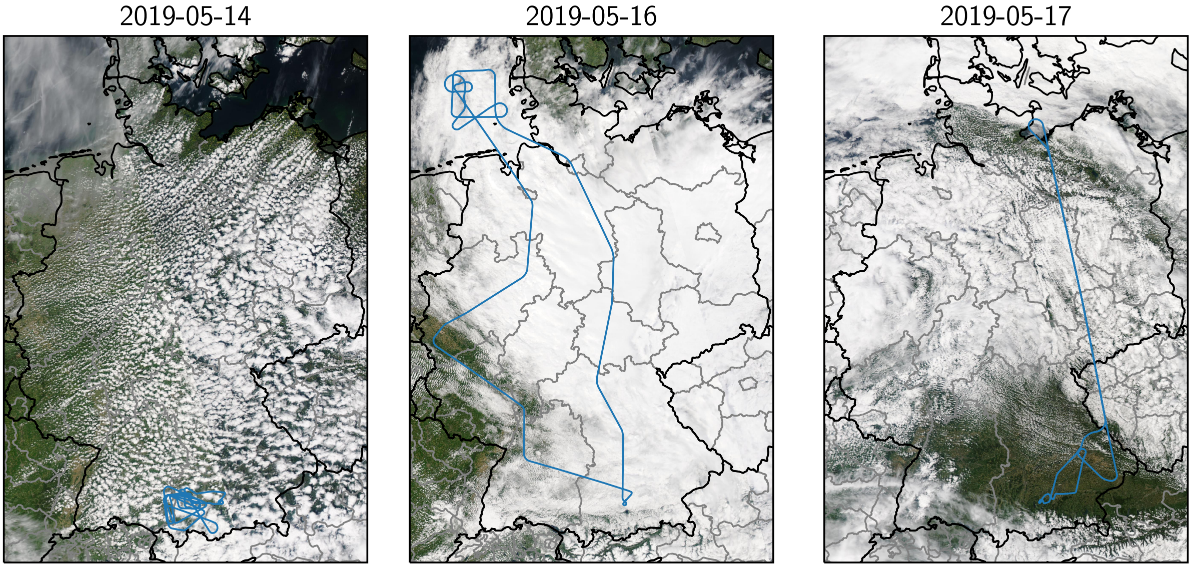

Figure 4.17: Cloud situation during EUREC^{4}A pretest as seen from MODIS Aqua satellite observations. The HALO flight track is shown in blue. MODIS data is provided by services from NASA's Global Imagery Browse Services (GIBS), part of NASA's Earth Observing System Data and Information System (EOSDIS).

4.3.2 Cloud Geometry from EUREC^{4}A Pretest

As shown in Figure 4.17, the flight on May 14 lead above a broken cumulus cloud field in the Allgäu area. Figure 4.18 shows a snapshot of observed clouds from the newly installed polarization resolving cameras. When comparing the image with one of the images from the NARVAL-II system (e.g. Fig. 3.15), substantial improvements in image quality are visible. Due to the improved automatic exposure system and the possibility for shorter integration times, the cloud tops are not over exposed anymore, while the dynamic range of the sensor is large enough to capture details of the ground surface simultaneously. In particular, the inner area of the clouds shows considerably more contrasts, which is the key improvement for the cloud tracking algorithm.

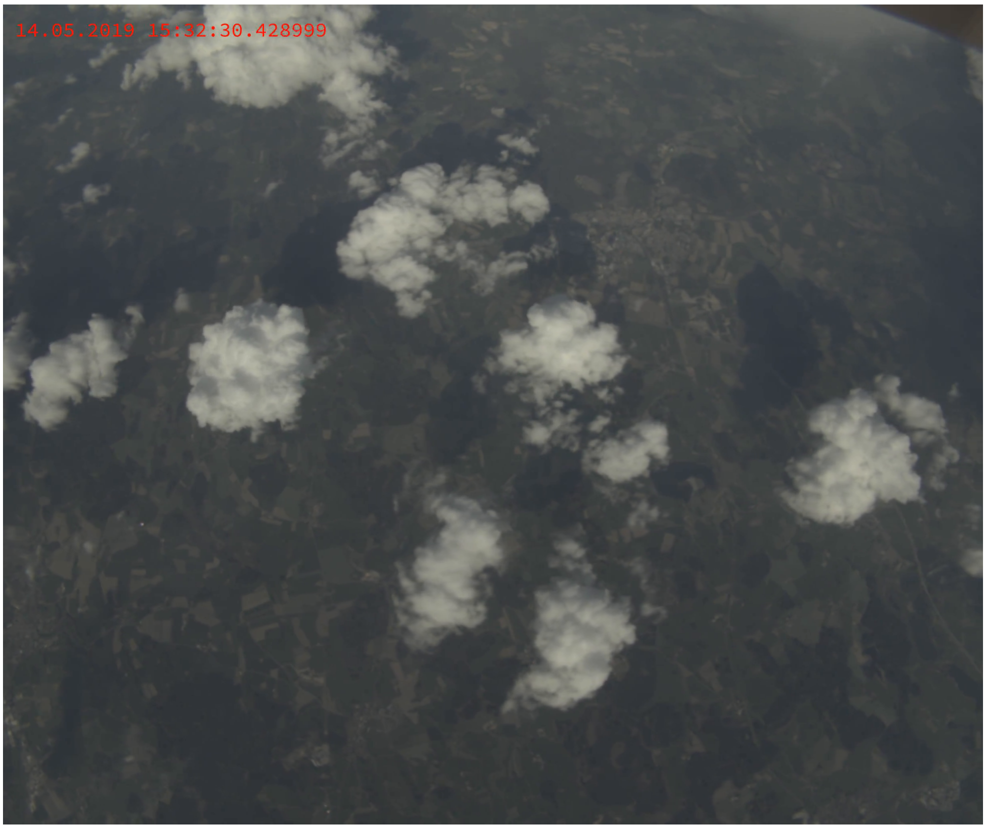

Figure 4.18: RGB image from test flight on 14 May 2019 captured with the *pola* camera: Some isolated cumulus clouds above Ellerazhofer Weiher and the city of Leutkirch in the Allgäu area, southern Germany.

Additionally, due to the improved meta data handling, required changes in the exposure time settings can be and are handled properly during cloud tracking. Due to the improvements in image quality and meta data handling, the stereographic method from Section 3.4.2 is now able to produce a much more detailed point cloud (Fig. 4.19) with less outliers. Compared to Fig. 3.14, the most prominent difference is that the new results also include many points across the cloud tops. First, this allows to quickly identify the collection of tracked cloud surface points with clouds in the original images visually while providing an interactive display of the cloud geometry. More importantly, the increased density and level of detail of the cloud surface points is key to distinguish between clouds and cloud holes automatically, which enables successful cloud surface reconstruction.

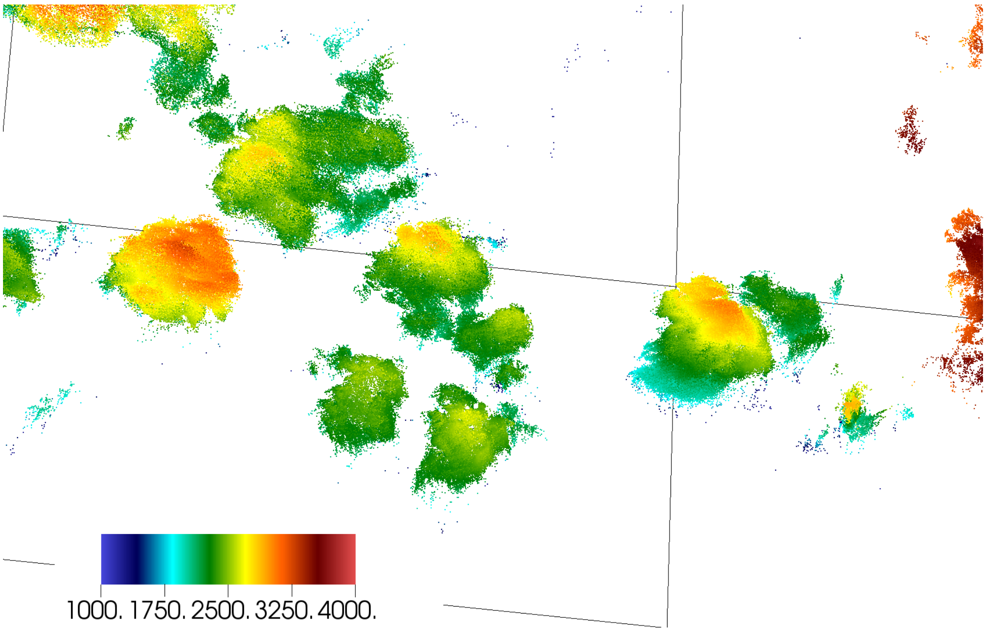

Figure 4.19: Point cloud from test flight on 14 May 2019: These points have been retrieved from images as shown in Figure 4.18 using the stereographic method. The color of the points denotes height in meter above WGS84.

The point clouds derived from the EUREC^{4}A pretest campaign can be successfully used as an input for Poisson-based surface reconstruction, leading to a meshed cloud surface. As mentioned in Section 3.4.3, Poisson based surface reconstruction always leads to a closed surface. Due to the unobserved cloud base, the algorithm tends to connect all clouds into one surface. As the point clouds contain only very few outliers and a dense set of points across the cloud, it is easy to cut this cloud surface mesh based on the distance between mesh vertices and the closest points in the point cloud, such that only actual cloud parts remain in the surface mesh. The resulting cloud surface mesh is shown in Figure 4.20. In order to provide a better visual reference to the original image, the cloud surface mesh has been positioned over satellite images of the ground surface using Google Earth and a similar camera perspective.

Together with a digital elevation model of the earth's surface, a digital model of the observation geometry can be built. Within this model, the locations and orientations of all imaging sensors of specMACS are known at all times. Using the projection method from Section 3.5.2, this allows to create a combined dataset which contains radiance mea-

Figure 4.20: Reconstructed cloud surface: Cloud surface mesh, extracted via Poisson surface reconstruction from stereographically retrieved points (Fig. 4.19. The reconstructed cloud surfaces have been converted to a COLLADA (Barnes et al., 2008) model and georeferenced using KML, such that the surfaces can be observed interactively using Google Earth. The perspective is roughly chosen to match the view of Figure 4.18.

surements from both hyperspectral cameras (VNIR and SWIR) as well as the RGB and polarization data from the polarized cameras on a common grid. In addition, information about surface type (cloud or ground), surface height above WGS84, surface orientation, and the geometric shadow flag is added to each pixel of the common data grid. This dataset provides a solid base for the investigation of cloud macrophysical properties and the application of retrievals for cloud microphysical properties.

Figure **??** shows an example of this dataset, based on the cloud scene introduced above. Due to the smaller swath of the hyperspectral sensors of specMACS, the combined data grid includes roughly the lower half of the images presented above. In this case, the image coordinates of the SWIR camera have been used as a base for the common grid. As the SWIR camera is a push-broom sensor, the axes are now time and across-track angle, which creates a distorted image compared to the "normal" photos presented above. In order to correctly represent observations of the earth's surface, the digital elevation model from the Shuttle Radar Topography Mission (SRTM) (Farr et al., 2007) has been used to generate a surface mesh of the earths surface. An additional benefit of integrating the ground surface is that the geometric shadow mask also reproduces shadows on the earths surface, without further changes to the algorithm.

,,

,,,,

4.3.3 Application of Tilted Bi-Spectral Retrieval

The retrieval of cloud surface location and orientation as demonstrated in the previous section is a prerequisite for the application of the tilted bi-spectral retrieval on measured data. However, the tilted retrieval method described in Section 3.5.3 can not be applied to the scene discussed in the previous section, as a basic assumption for the tilting method is that the ground surface is either not visible or almost black, which is valid for ocean surface outside of the sunglint region and larger clouds but not for small clouds above vegetated surfaces. In particular, the 870 nm plot of Fig. **??** shows that the brightness of the vegetated surface is comparable to the brightness of the cloud edges and thus, the measured cloud radiance is largely influenced by the unknown surface properties and the resulting high radiance values are not included in the look up table.

Instead, the tilted retrieval is applied to data from the test flight on May 16, with homogeneous overcast conditions over Germany. These favorable cloud conditions were also used by Weber (2019) and Pörtge (2019) for effective droplet radius retrievals using glory and cloudbow observations, so their results can be used for comparison. Figure 4.22 shows retrieval results along the flight path from 14:30 UTC until 14:40 UTC. This is the same time period as analyzed by Pörtge (2019, Fig. 38) using cloudbow and glory based retrievals on data from the *pola* camera. The time axis of the data from cloudbow and glory retrievals has been modified such that the indicated time is the time at which the aircraft flew closest to the observed cloud part, instead of showing the time at which the actual measurement has been taken. This allows for a better comparison between the different retrieval measurement methods. Again, *flat* and *tilt* indicate the results from the two bi-spectral retrieval methods. *flat* denotes the classical plane-parallel approach while *tilt* denotes the tilted approach. In this case, the cloud surface orientation derived from the stereographic reconstruction has been used to determine the relevant angles for the look-up table. The curves show the result of averaging all retrieval results which are marked as valid across the flight track.

The results from the bi-spectral retrieval show generally larger values as obtained from the glory and cloudbow retrievals. The difference can be caused by multiple effects. First, the measurement has been taken above vegetated ground, which can cause a significant error in the bi-spectral retrieval but should not affect the results of the glory- and cloudbow-based methods. Second, it can be expected that the bi-spectral retrieval carries information from deeper inside the cloud compared to the glory and cloudbow retrievals, which are expected to be sensitive to cloud microphysics in a smaller cloud shell. Entrainment can potentially cause the droplet size to decrease at the cloud boundary due to evaporation. Accordingly, the resulting gradient in cloud droplet size would lead to smaller effective radii retrieved by glory and cloudbow and larger effective radii retrieved by the bi-spectral retrievals. Thus, the observed differences between the retrieval results might actually carry

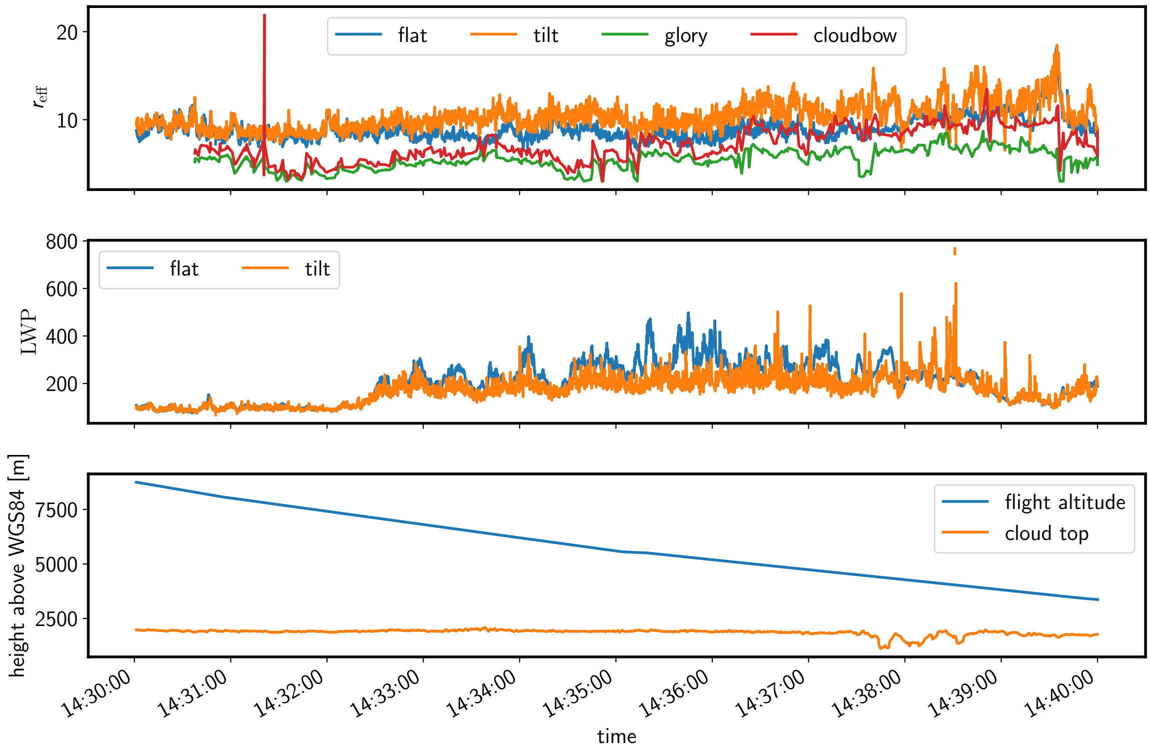

Figure 4.22: Cloud microphysics retrieval comparison using EUREC^{4}A pretest data on May 16. The bi-spectral retrieval is compared to effective radius retrievals base on glory and cloudbow observations. Flight altitude and cloud top height are provided for reference.

valuable information about the internal cloud evolution.

At about 14:32 UTC in Figure 4.22, the tilted r_{eff} retrieval slowly departs from the flat retrieval towards larger values. This raise in effective radius can also be seen in the retrievals using glory and cloudbow, but is missed by the plane-parallel retrieval. When looking at the pictures of the cloud surface before and after this departure (Fig. 4.23), it can be seen that in this period, the cloud field transitioned from a slightly broken field towards a homogeneous and closed cloud field, which however still shows occasional wave-like structures. The retrieval of liquid water path also shows that the clouds change their general structure in this period, which indicates that a change in effective radius at that point is not unlikely.

The results form the tilted retrieval show high frequency variations with large amplitudes when compared to the results of the flat retrieval method. This behavior originates in the difficulty to obtain precise cloud surface orientations. The surface normals are ultimately derived from differences of the stereographic cloud location information and small errors in cloud location can therefore lead to large errors in surface normal estimation. However, as seen most prominently in the retrieval of LWP, medium frequency variations, likely originating from larger cloud 3D effects are removed from the retrieval results. In the time

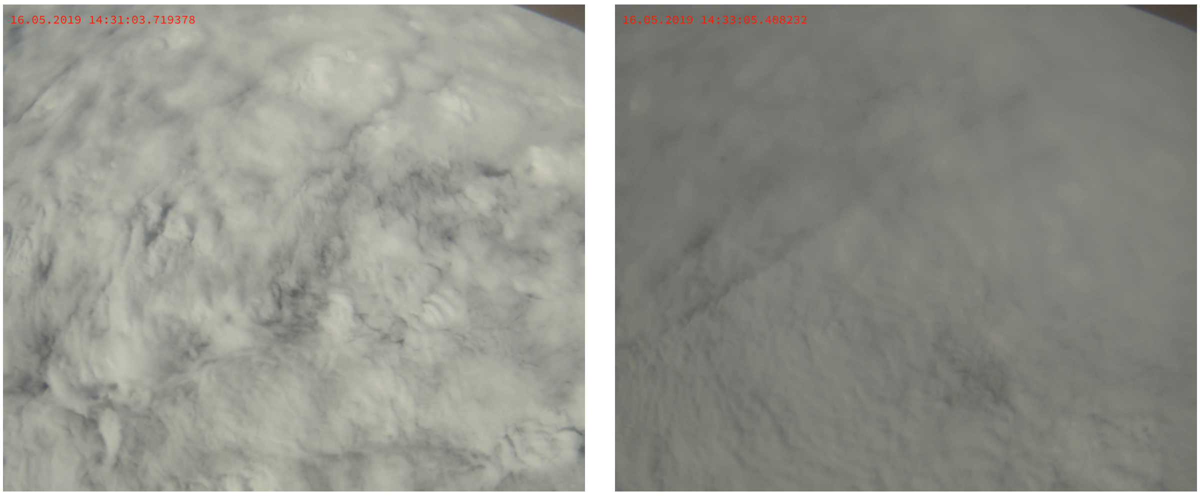

Figure 4.23: Cloud situation before and after the increase in retrieved liquid water path. The first images was taken at 14:31:03, the second image at 14:33:05.

frame between approximately 14:35 UTC and 14:37, the cloud surfaces show no visual indication of a strong change in liquid water path, suggesting a flat curve being more likely than a curve with strong gradients. The solar zenith angle at the time and location of the measurement has been $\Theta_\mathrm{s} \approx 49°$, very similar to 45° as in the second case discussed in Section 4.1.5. The theoretical wave cloud experiment showed that missing information about the cloud surface orientation on a wavy stratiform cloud likely leads to a strong overestimation in liquid water path for that solar zenith angle, which is matched by the presented measurements.

These results indicate that the application of the tilted bi-spectral retrieval may improve the microphysical retrieval quality by reducing larger systematic errors at the expense of larger high-frequency noise. A final assessment on potential improvements of the retrieval error by the tilted approach and if the differences between bi-spectral and glory/cloudbow based retrievals are really due to entrainment will be possible in a future assessment of data from the EUREC^{4}A field campaign with multiple measurements over the ocean and in-situ measurements from other aircraft.

Chapter 5

Discussion of the Developed Methods

This chapter gives a brief wrap up of the instrument and method development done in this study. First, a relation of the stereographic retrieval method to previous work is made, followed by a quick sum up of the method developed in this work. The chapter continues by pointing out how microphysical retrieval methods may benefit from the availability of cloud surface location information. An important part is Section 5.4, where the most important technical lessons learned during the system setup and method development are shown. The chapter finishes by introducing further interesting and upcoming applications of the cloud geometry retrieval.

5.1 Comparison to other Studies

A classic method for deriving cloud top height from satellite missions is to exploit the temperature gradient in the earth's atmosphere and use thermal imaging to derive cloud top temperatures (Strabala et al., 1994). At a temperature lapse rate of $6.5\,\frac{\mathrm{K}}{\mathrm{km}}$ in the lower troposphere (Anderson et al., 1986), retrieving cloud top height with uncertainties below $100\,\mathrm{m}$ would require a measurement accuracy of $0.65\,\mathrm{K}$ including uncertainties in cloud emissivity and the atmospheric temperature profile, which is hardly possible to achieve. Another approach is to use absorption of oxygen throughout the atmosphere to derive the distance an observed ray of light traveled through the atmosphere (e.g. Fischer et al., 1991; Zinner et al., 2019). While this approach can produce densely populated distance information using the same hyperspectral sensors as used for the microphysical retrieval, these methods generally suffer from similar accuracy constraints on the knowledge of atmospheric profiles. Stereographic methods usually require either a static scene or a static observer. Several experiments use stereographic methods to georeference cloud fields from ground-based all-sky cameras (e.g. Beekmans et al., 2016; Crispel and Roberts, 2018; Romps and Öktem, 2018). Spaceborne stereographic methods for the use on multi-angle imaging satellites have been developed for example for the Multi-angle Imaging SpectroRadiometer (MISR) (Moroney et al., 2002) and the Advanced Spaceborne Thermal Emission and Reflection Radiometer (ASTER) (Seiz et al., 2006). Due to the large time-delay between the measurements of an overpassing satellite (several minutes), these methods rely on an estimate of the wind field to remove cloud motion from the measurement. Stereographic distance measurement from the HALO aircraft has already been evaluated, manually by Jäkel et al. (2017) and using some automation by Schwarz (2016). The method presented in this thesis uses the fast angular speed of the moving aircraft and subsequently shorter measurement times to reduce the impact of cloud movement within the measurement.

5.2 Derivation of Cloud Location using specMACS

The 3D cloud geometry reconstruction method described in this work is able to produce an accurate set of reference points on the observed surface of clouds. The accuracy has been verified by comparison to nadir pointing active remote sensing measurements. Using data from the observation of a stratiform cloud field, it was shown that no significant systematic errors are introduced by looking in off-nadir directions. Even for sunglint conditions, cloud top heights can be derived: as clouds move through the image while the sunglint stays at a relatively stable viewing direction, clouds can be observed when they are in parts of the sensor which are unobstructed by the sunglint. Because of the wide field-of-view of the sensor, there are always viewing directions to each cloud which are not affected by the sunglint.

The derivation of cloud surface location requires accurate aircraft location and attitude information, geometric calibration of the camera intrinsics and knowledge about the mounting position and orientation of the cameras inside the aircraft. Aircraft location and attitude information on the HALO aircraft is provided by its basic instrumentation package and thus is not considered in this work. Geometric calibration of the camera intrinsics can be done using the commonly used chessboard calibration method, which can be carried out without special laboratory requirements. Finally, it is shown that it is possible to measure the exact camera orientation within the aircraft by projecting images taken with the camera onto georeferenced satellite images from the ground surface.

A visible contrast suited for point matching is a central requirement of the method. In order to obtain well resolved contrasts throughout the cloud surface, an automatic exposure control method, which is well adapted to the observation of cloudy scenes, is indispensable. Additionally, as the scenes are very bright, care has to be taken that the camera system is capable of very short exposure times. With the upgrade of the 2D camera system to the polarization resolving cameras for the EUREC^{4}A field campaign, such a system was implemented and the resulting point clouds are dense enough to support the generation of a triangulated cloud surface mesh.

5.3 Influence on Cloud Property Retrieval Methods

Cloud location information is an important auxiliary quantity for cloud microphysical retrievals. It relates the retrieved quantities to the atmospheric background profiles and thus allows to estimate other quantities like pressure and temperature at the measurement location. Furthermore, the geometry of cloud and ground surfaces is required to accurately map measurements from different sensors taken at different times onto each other if the sensors are not perfectly aligned. While useful for the alignment of the spectral measurements, the same method allows for a large improvement of effective radius retrievals using glory and cloudbow (see Sec. 5.5). A geometric model of the observed cloud scene allows to derive a shadow mask using a ray tracing method. Cloud shadows can not be identified unambiguously solely based on brightness values. Therefore, the additional shadow mask through ray tracing provides a useful filter criterion for cloud microphysical retrievals.

It is also possible to obtain the cloud surface orientation from the triangulated surface meshes. However, as this method is essentially calculating differences of large distance values, small errors in cloud location estimation lead to larger errors in the estimation of cloud surface orientation. As a result, the retrieved values for r_{eff} and LWC in Section 4.3.3 show a higher high-frequency noise if cloud surface orientation is considered compared to the case when it is ignored. Nonetheless, larger medium frequency oscillations, which are likely retrieval errors of the plane-parallel bi-spectral retrieval approach get rejected by the presented retrieval approach which considers the retrieved cloud surface orientation. A final assessment of the retrieval behaviour would however require data from clouds over the darker ocean and should consider in-situ measurements for a proper validation. The upcoming EUREC^{4}A field campaign will provide both of these.

5.4 Lessons Learned while Developing the specMACS Measurement System

During the development of the stereographic method, it became clear that a precise camera calibration, that is relative viewing angles in the order of 0.01°, is crucial to this method. A permanent time-synchronization between the aircraft position sensors and the cameras, accurate at the order of tens of milliseconds is indispensable as well. It should be noted that this does involve time stamping each individual image to cope with inter-frame jitter, as well as disabling any image stabilization inside the camera.

Another important point is the synchronization of image data and meta data. The spectral cameras and the 2D imager installed during NARVAL-II and NAWDEX used different signalling wires for image data and control signals (including exposure time, shutter state and frame rate). Due to different timing on these lines, it can not be guaranteed that a change in camera settings can be attributed to a precise frame number. The new polarized cameras which will be used during EUREC^{4}A and have already been tested in May 2019 are connected via GigE Vision. This connection and data format allows image meta data to be embedded into each image frame. That improvement ensures that every change in camera settings can be precisely associated to a single frame during post processing of the measured data. That way, no frames need to be skipped in the transition time between two different camera settings and cloud surface reconstruction is correctly handled across changes in camera settings.

The 2D imager during NARVAL-II had been operated at its shortest possible exposure time during large fractions of the measurement period. Still, many frames have been overexposed, which lead to severe image degradation. Furthermore, the new cameras are capable of shorter exposure times, which reduces the amount of overexposed images. The automatic exposure control system has been customized for EUREC^{4}A such that contrasts on bright cloud surfaces are enhanced. That way, vastly more good cloud surface points can be gathered and which has been the breakthrough for generating triangulated cloud surface models.

The first downward facing specMACS setup in HALO did not include fans to heat up the window from the inside. At outside air temperatures of down to $-80\,^{\circ}\mathrm{C}$, it was not possible to dry the inside air enough to prevent window icing. In the subsequent setup, starting with the NAWDEX field campaign, additional fans have been installed, which effectively prevented the window from icing and allows for continuous measurement, independent of flight altitude. While initially, it was planned to cool the specMACS instrument compartment in the HALO boiler room using a unidirectional compressor based heat pump, this idea has been replaced by simpler thermo electric cooling elements. That change later proved extremely valuable, as in fact, the generated heat of roughly 500 W is not sufficient to sustain the desired instrument temperature at high flight levels. Instead, the regulated thermoelectric cooling elements, which can operate in either direction, turn the heat flow around in order to heat up the instrument compartment and sustain proper temperature levels.

5.5 Polarized Measurements of Glory and Cloudbow

As already shown by Mayer et al. (2004) and Alexandrov et al. (2012), polarization resolving multi-angle observations of glory and cloudbow can be used to derive cloud droplet effective radius r_{eff} and also the variance of the size distribution v_{eff} with higher accuracy than possible with spectral methods. The upgraded polarization resolving cameras for the specMACS system during the EUREC^{4}A campaign are tailored to provide these kinds of measurements. As shown by Weber (2019) and Pörtge (2019) using measurements from the EUREC^{4}A pretest campaign in May 2019, the upgraded cameras work as expected. A passive retrieval of cloud surface geometry improves the glory and cloudbow based retrievals, as a known cloud surface location enables the collection of measurements of a small cloud volume from multiple images instead of relying on the assumption of microphysical homogeneity throughout a larger patch of clouds.

Figure 5.1 shows the observation geometry for multi-angle observations as required to measure the angular radiance distribution from glory or cloudbow. If only a single image is considered, the geometry is as indicated in Panel A. It is possible to observe the cloud surface under a large range of observation angles from a single aircraft location. However, even if the image sensor is able to resolve small details of the cloud structure (Δx), the total cloud surface area which must be considered for the measurement is relatively large (ΔX). As the retrievals use the relationship between scattering angle and observed radiance, any cloud inhomogeneities within this large cloud surface contribute to the retrieval error. Panel B shows how the situation is changed if the distance Δz to the cloud surface is known. In this case, multiple images from a fast moving aircraft or multiple aircraft can be used. By using multiple images, the same range of scattering angles can be observed at a substantially reduced footprint on the cloud surface (ΔX). This change improves the spatial retrieval resolution and as smaller cloud patches are more likely homogeneous than larger cloud patches, the retrieval accuracy is improved as well. The angular resolution (Δx) is again set by the camera resolution and, if a single, fast-moving aircraft is used to capture the images, the size of the footprint on the cloud surface can be adjusted by the sampling rate of the camera. As as e.g. the dashed lines are parallel, the distance travelled is equally large as the size of the footprint. An additional benefit of the second method is that the exact location of the measurement footprint is known in 3D space. This way, retrieval results originating from different perspectives can be matched and compared (see Fig. 4.22 for an example).

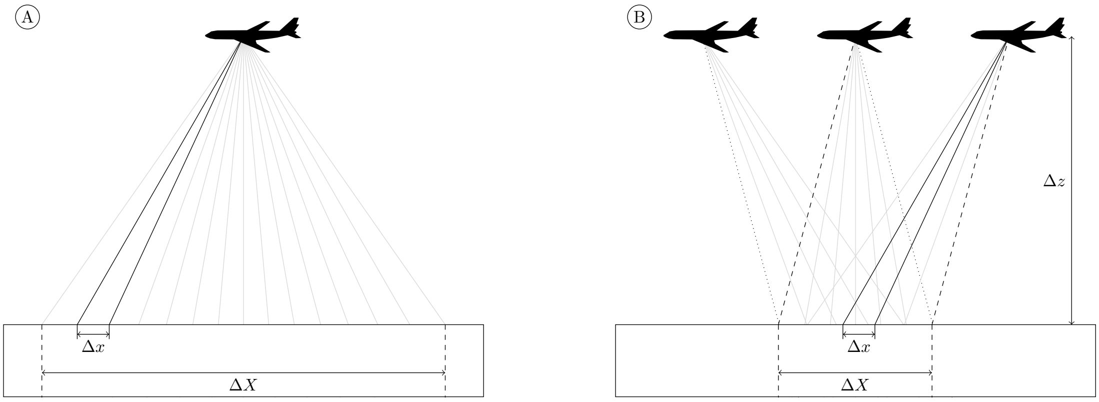

Figure 5.1: Multi-angle observations of a cloud using a single (A) or multiple (B) images. While the second option significantly reduces the measurement footprint ΔX, this method is only possible if the distance to the cloud Δz is known. The dashed and dotted lines in (B) are pairwise parallel, thus the combination of the fans of viewing rays in (B) indeed covers the same angular range as the single fan in (A).

5.6 Possibility for Multi-Aircraft Cloud Geometry

As mentioned in 4.3.2, retrieving the lower cloud boundaries is not possible when observing clouds from above. During the EUREC^{4}A field campaign, multiple aircraft will operate in a coordinated manner. In this setting, it may be possible to observe clouds from below using a low flying aircraft simultaneously with observations from above using HALO. From each of these observations, a georeferenced and oriented point cloud can be derived using the method described in this study. These point clouds can easily be merged: as each point can be handled individually the point sets only have to be appended to each other. Poisson surface reconstruction can then be applied on the merged point cloud. If one aircraft observed the cloud tops and the other the cloud base, the cloud surface reconstruction should directly lead to properly closed surfaces around the observed clouds. A closed cloud representation would allow to calculate cloud volume and thus give a first constraint to it's water content.

Chapter 6

Summary and Conclusion

The largest uncertainties in the estimated radiative forcing in global climate models are caused by a lack of knowledge on cloud feedbacks. In order to test the assumptions of the underlying cloud models, it is necessary to capture the important physical properties of clouds and their surroundings by measurements. Passive imaging techniques are highly effective in capturing many clouds in large observation areas. While passive remote sensing methods for cloud microphysical properties have been developed for decades, common applied methods are restricted to the assumption of plane-parallel clouds and to spatial resolutions in the order of one kilometer. Especially for shallow tropical clouds, which are known to cause large uncertainties in climate sensitivity estimates, the plane-parallel assumption is clearly not fulfilled and many of these clouds are much smaller than one kilometer. The key problem is that the observed radiation is influenced by the unknown three dimensional cloud structure. Previous studies suggest that part of this influence can be explained by the local cloud surface orientation. These issues lead to the primary research questions investigated within this thesis:

- Can cloud geometry be determined from passive airborne remote sensing in the solar spectral range?
- Can this information be used to improve optical and microphysical property retrievals of inhomogeneous clouds?

In order to investigate these questions, the previously existing hyperspectral imaging system specMACS has been equipped with additional two-dimensional imaging sensors and modified such that it could be used on board the HALO research aircraft in a downwards looking perspective. The setup has been tested and incrementally improved throughout four airborne field campaigns. Based on the newly available measurement data, a stereographic method for the retrieval of cloud surface location and orientation has been developed and validated. A key problem for the reconstruction of a closed cloud surface representation has been the quality of image- and metadata, which was resolved in the final iteration of the measurement setup.

In order to combine the results of the stereographic retrieval with hyperspectral measurements, a ray tracing framework (RayLi) has been developed. This framework also allows to calculate per pixel information about cloud surface orientation and to identify shadowed areas directly from the retrieved cloud geometry. The resulting dataset is the basis for the application of the tilted bi-spectral cloud microphysical retrieval developed within this thesis. The tilted bi-spectral retrieval uses local cloud surface orientation as an additional input to the retrieval method introduced by Nakajima and King (1990). The applicability of such a retrieval and the differences to the classical approach have been investigated using theoretical studies as well as measurements.

In it's latest iteration, the stereographic method is capable of producing dense georeferenced point sets across the full visible cloud surface. The dense point cloud can reliably be translated into a triangulated mesh of the visible cloud surface, a crucial information in further passive remote sensing applications. Accordingly, the answer to the first research question is positive as specMACS measurements can be used to derive cloud geometry. The answer to the second question on improving cloud property retrievals is more ambiguous. For the retrieval of effective cloud droplet radius, the conducted theoretical studies show that, depending on the cloud scene, the tilted retrieval may indeed provide better results, especially for convex cloud shapes. However, for all investigated cases with low cloud aspect ratio, the retrieval quality of liquid water path was severely reduced. Generally, the retrievals did not work when the investigated parts of the clouds are influenced by shadows, when they are illuminated almost parallel to the cloud surface, or, with respect to the sensor, from the behind. In these cases, the information about the cloud surface geometry can still be used to filter out measurements for which the retrieval is known to fail. On the other hand, the information on cloud location greatly improves droplet effective radius retrievals based on glory and cloudbow observations, in particular for spatially inhomogeneous cloud scenes (Weber, 2019; Pörtge, 2019). These retrievals are expected to produce small errors in droplet effective radius, but are representative only for a thin cloud shell. Cloud effective radius retrievals using the discussed bi-spectral retrieval methods and the methods based on glory and cloudbow show significant differences. At this state, it remains an open question whether the tilted retrieval approach performs better than the classical approach and if the differences between bi-spectral and glory/cloudbow originate from the sensitivity to different depths into the cloud or from problems in the retrieval method. Thus, the answer to the second question is partly positive as cloud geometry information improves glory and cloudbow retrieval. However, the original hypothesis about improving the bi-spectral retrieval via the tilted method could not be confirmed for all cases.

Finally, it remains to say that the current setup of the hyperspectral measurement system specMACS, including the newly developed retrieval methods, is now available for the upcoming EUREC^{4}A field campaign, which might currently be the largest effort to characterize trade wind cumulus clouds and their surroundings. During this campaign, additional in-situ measurements will provide a broader data basis to investigate improvements in cloud microphysical retrievals. Certainly the combination of all contributing measurement systems will create a unique dataset for the understanding of clouds and circulation.

Appendix A

Monte-Carlo Integration

Computational algorithms relying on random sampling to obtain numerical results are commonly called Monte-Carlo methods. The individual obtained results vary between multiple executions of the algorithm, only the expected value corresponds to the true result. As the variance of the mean of many samples is reduced with increasing count of samples, the expected value of the result can be approximated more and more by increasing the number of samples. As many samples are required to obtain an accurate result, such methods tend to be very compute intensive, but allow to solve some kinds of problems which would be even harder or impossible to solve otherwise.

A particular problem, which can be solved by Monte-Carlo methods is the definite integral over the domain X_f of a function f:

$$\int_{X_f} f(x)dx \tag{A.1}$$

The integral can be approximated by the estimator F_N, which is defined by sampling N values $x_i, i \in [1, N]$ independent and identically distributed according to a chosen probability distribution p:

$$F_N = \frac{1}{N} \sum_{i=1}^{N} \frac{f(x_i)}{p(x_i)} \tag{A.2}$$

The choice for p can be free as long as its domain $X_p \supseteq X_f$, the support $\mathrm{supp}(X_p) \supseteq \mathrm{supp}(X_F)$ and $\int_{X_p} p(x)dx = 1$. The expected value $\mathrm{E}[F_N]$ is equal to the solution of the integral:

$$
\begin{aligned}
\mathrm{E}[F_N] &= \mathrm{E}\left[\frac{1}{N}\sum_{i=1}^{N}\frac{f(x_i)}{p(x_i)}\right] && \text{(A.3)}\\
&= \frac{1}{N}\sum_{i=1}^{N}\mathrm{E}\left[\frac{f(x)}{p(x)}\right] && \text{(A.4)}\\
&= \mathrm{E}\left[\frac{f(x)}{p(x)}\right] && \text{(A.5)}\\
&= \int_{X_p}\frac{f(x)}{p(x)}p(x)dx && \text{(A.6)}\\
&= \int_{X_p} f(x)dx && \text{(A.7)}\\
&= \int_{X_f} f(x)dx && \text{(A.8)}
\end{aligned}
$$

The variance $\mathrm{Var}[F_N]$ is dependent on the choice of p and gets reduced by increasing the number of samples:

$$
\begin{aligned}
\mathrm{Var}[F_N] &= \mathrm{Var}\left[\frac{1}{N}\sum_{i=1}^{N}\frac{f(x_i)}{p(x_i)}\right] && \text{(A.9)}\\
&= \frac{1}{N^2}\sum_{i=1}^{N}\mathrm{Var}\left[\frac{f(x)}{p(x)}\right] && \text{(A.10)}\\
&= \frac{1}{N}\mathrm{Var}\left[\frac{f(x)}{p(x)}\right] && \text{(A.11)}\\
&= \frac{1}{N}\left(\int_{X_p}\left(\frac{f(x)}{p(x)}\right)^2 p(x)dx - \mathrm{E}[F_N]^2\right) && \text{(A.12)}\\
&= \frac{1}{N}\left(\int_{X_f}\frac{f^2(x)}{p(x)}dx - \mathrm{E}[F_N]^2\right) && \text{(A.13)}
\end{aligned}
$$

An ideal choice of p would be proportional to f: $f = cp$ and $X_f = X_p$. In this case, the variance simplifies to:

$$\mathrm{Var}[F_N] = \frac{1}{N}\left(\int_{X_f} c^2 p(x)dx - c^2\right) = 0 \tag{A.14}$$

However, this particular choice is difficult to obtain, as taking samples from that p would essentially require to solve the integral over f, which was the purpose of the entire calculation. Still, choosing a p which is closer to being proportional to f will already reduce the variance and heuristics for choosing it are called variance reduction techniques.

In the above derivation, the bounds of the integral are deliberately not given as upper and lower bounds, but as the entire domain of the probability distribution. This is the big advantage of numerical integration using Monte-Carlo methods: the number of samples taken (N) can be chosen independently of the dimensionality of the integral and thus the probability distribution. The scattering part of the radiative transfer equations consists of a recursively defined integral over the whole sphere around the scattering location. As the integral is defined recursively and a general closed form is not known, this poses an infinite-dimensional integral, which is impossible to solve to arbitrary depth if more than one sample per dimension has to be taken. By allowing to choose N independently of the number of dimensions, solving the problem becomes feasible.

Appendix B

flatds file format

The specMACS system captures image data at a high data rate during the measurement phase. As measurement flights are not easy to repeat, the focus of storing the measurement data is on how to get the data reliably and fast enough on a permanent storage medium. The easiest way to do so would be just to sequentially write out all the raw sensor data to a file. But additionally to the raw measurement data, some metadata has to be associated with the raw data as well, such that raw data can later be properly calibrated and referenced with respect to space and time. Historically, specMACS data has been stored in the ENVI file format. The ENVI format consists of a raw data file and a secondary header file consisting of metadata, which are associated by a common file name prefix. The format is frequently used for hyperspectral observations, but allows only little extensibility. In particular, changing sensor settings, 2D images, and per-frame timestamps can not be represented well in the format. All of these data is relevant for the specMACS system. Furthermore, there has been desire to only have one self-contained file for each measurement and to allow for netCDF-like access to the data, which provides great extensibility and is very common in atmospheric science and thus allows for better reuse of the captured data.

Flatds tries to combine both worlds: fast sequential writing and multi-dimensional data access of many variables which are enriched with metadata stored in attributes. A flatds file starts with the ASCII-letters *FLATDS*. The following two bytes are reserved and by default 0. If flatds is extended in future, the two 0-bytes may be changed, indicating that the format has been changed and should not be read according to the rules described below. Flatds uses little endian byte order. The last 8 bytes of a flatds file store the header offset from the beginning of the file as a 64bit unsigned integer. The header is stored between the header offset and (file size - 8) as MessagePack (Furuhashi, 2019) encoded data according to the following scheme:

```
{
    "vars": {
        <name>: {
            "ofs": <file offset>,
```

```
            "t": <dtype>,
            "st": [<strides,...>],
            "is": <item size>,
            "d": [<dimension indices,...>],
            "attrs": {...}
        }
    },
    "dims": [
        [<name>, <size>],
        ...
    ],
    "attrs": {...}
}
```

On the top level of the header structure, variables *(vars)*, dimensions *(dims)* and optionally global attributes *(attrs)* are defined.

vars Variables can be stored at any location in a *flatds* file as long as they do not collide with the initial 8 byte signature and the header data. The data layout is chosen by the writer implementation and is meant to be adapted to the data acquisition process. Variable data must be stored in a regular pattern, but may be interleaved by other variables. Later, the reader must be able to locate the variable data inside the file. This is the purpose of the *vars* entry in the header structure. A variable is identified by a freely chosen *name*. The first byte of the variable data can be found at *file offset* bytes from the beginning of the file. The *strides* array has an entry for each dimension of the variable data and describes how many bytes the read pointer must be incremented to advance one element in the respective dimensions. The *item size* is the number of bytes of a single element of the variable. The *dtype* can currently be one of ”uint64”, ”int64”, ”float32”, ”float64”, ”uint8”, ”int8”, ”uint16”, ”int16”, ”uint32”, ”int32” and defines how the element data has to be interpreted. The *dimension indices* array also has one entry for each dimension and is a zero-based pointer into the *dims* structure, describing each variable dimension. Note that variables sharing common dimensions should create only one entry in the *dims* structure and each variable should point to the same dimension. The *attrs* are optional and can contain metadata for the variables. In particular, it is encouraged to use metadata according to the CF conventions (Eaton et al., 2019).

dims Dimensions are meant to be shared amongst variables and thus are stored outside of the variable definitions. They are stored as an ordered list of [*name*, *size*] pairs. The name can be freely chosen, but if it is equal to a name of a one-dimensional variable and the variable’s only dimension is this dimension, the variable should be interpreted as the dimenson’s coordinates. The size of the dimension describes the number of elements along this dimension.

attrs Global attributes are optional. Otherwise the same rules as for variable attributes apply.

List of Figures

Glossary

EUREC^{4}A Field campaign taking place in Jan/Feb 2020 (Bony et al., 2017) `http://www.eurec4a.eu`. 42, 44, 87

2DCAM two dimensional RGB camera of specMACS. 53

AABB Axis aligned bounding box. The smallest box with it's surfaces being parallel to the coordinate frames axes which entirely includes another geometric structure.. 25

AC Alternating Current. 36

ACRIDICON-CHUVA Field campaign based in Manaus, Brazil in September 2014 (Wendisch et al., 2016). 35, 42

CMIP3 third phase of the Coupled Model Intercomparison Project of the World Climate Research Programme's (WCRP). 1

DC Direct Current. 36, 38

DISORT DIScrete ORdinate Radiative Transfer, a deterministic solution to radiative transfer in one dimensional geometry. Developed by Chandrasekhar (1960) and Stamnes et al. (1988). The implementation used for this work is by Buras et al. (2011) and contained in libRadtran. 70

EGM2008 Earth Gravitational Model 2008, an accurate model for the geoid undulation (i.e. difference between the WGS84 ellipsoidal earth model and the geoid) (Pavlis et al., 2012).. 48

Ethernet Physical interface for local area computer networks as specified in IEEE 802.3. 36, 38, 41

GPS Global Positioning System, US american satellite based world wide navigation system.. 47, 117

HALO High Altitude and Long Range Research Aircraft (Krautstrunk and Giez, 2012). 34, 39, 42, 44, 47, 53, 102

HTTP HyperText Transfer Protocol. 38

IFOV instantaneous field of view: the opening angle or solid angle of a single pixel of a remote sensing instrument. 8

KML Keyhole Markup Language, an OGC standard for annotating images and other data with georeferencing information.. 48

libRadtran Library for radiative transfer. A collection of radiative transfer codes and additional functions (Emde et al., 2016; Mayer and Kylling, 2005). 70, 115

local horizon Cartesian Coordinate frame, which is parallel to the earth's surface at some location and aligned to the local north. 53

LWC Liquid Water Content, ammount of liquid water in a given volume. 16

LWP Liquid Water Path, total ammount of liquid water in an atmpospheric column. 70

mounttree Data structure and library for transformations between nested coordinate systems. 48

MYSTIC Monte Carlo code for the physically correct tracing of photons in cloudy atmospheres (Mayer, 2009; Mayer and Kylling, 2005; Emde et al., 2016). 69

NARVAL-II next-generation aircraft remote-sensing for validation studies field campaign based in Barbados (Stevens et al., 2019). 1, 39, 40, 43, 70

NAWDEX North Atlantic Waveguide and Downstream Impact EXperiment (Schäfler et al., 2018) `http://nawdex.org`. 40, 43

NK Nakajima-King type retrieval for cloud optical thickness and effective droplet radius (Nakajima and King, 1990).. 69

RayLi Modular Monte Carlo code, developed within the work of this thesis. 4, 69

reference Cartesian Coordinate frame, which is tangential to the earth's surface at an arbitrary location close to the measurement area. This frame is used for calculations between measurements from multiple aircraft locations and for raytraycing.. 53

REST REpresentational State Transfer. 38

RS-422 Serial communication bus using twisted pair according to stadards TIA/EIA-422. 38, 40

SLS specMACS life support system. 36–38, 40

specMACS hyperspectral imaging system of the Munich Aerosol Cloud Scanner. 34, 36, 39, 41, 42, 44, 109, 113, 115–117

SWIR ShortWave InfraRed sensor of specMACS. 34, 38–40, 42, 44, 53, 64, 91, 113

TEC ThermoElectric Cooler, solid-state electrically driven heat pump, based on the Peltier effect. 39, 40

TRU Transformer Rectifier Unit. 36

VGA Video Graphics Array, connection between computer and monitor. 41

VNIR Visible and Near InfraRed sensor of specMACS. 34, 38, 39, 42, 44, 53, 64, 91, 113

WGS84 World Geodetic System 1984, ellipsoidal coordinate system which spans around the earth and is used amongst others by aviation in general and GPS in particular (NIMA Geodesy and Geophysics Department, 2004). 48, 50, 51, 53, 90, 115

Bibliography

Mikhail D. Alexandrov, Brian Cairns, Claudia Emde, Andrew S. Ackerman, and Bastiaan van Diedenhoven. Accuracy assessments of cloud droplet size retrievals from polarized reflectance measurements by the research scanning polarimeter. *Remote Sensing of Environment*, 125:92–111, 2012. ISSN 0034-4257. doi: https://doi.org/10.1016/j.rse.2012.07.012. URL `http://www.sciencedirect.com/science/article/pii/S0034425712002866`.

Gail P. Anderson, Shepard Anthony Clough, F. X. Kneizys, James H. Chetwynd, and Eric P. Shettle. AFGL atmospheric constituent profiles (0-120 km). Technical report, 1986.

Matthew P. Bailey and John Hallett. A Comprehensive Habit Diagram for Atmospheric Ice Crystals: Confirmation from the Laboratory, AIRS II, and Other Field Studies. *Journal of the Atmospheric Sciences*, 66(9):2888–2899, 2009. doi: 10.1175/2009JAS2883.1. URL `https://doi.org/10.1175/2009JAS2883.1`.

H. W. Barker, M. P. Jerg, T. Wehr, S. Kato, D. P. Donovan, and R. J. Hogan. A 3D cloud-construction algorithm for the EarthCARE satellite mission. *Quarterly Journal of the Royal Meteorological Society*, 137(657):1042–1058, 2011. ISSN 1477-870X. doi: 10.1002/qj.824. URL `http://dx.doi.org/10.1002/qj.824`.

Mark Barnes, Ellen Levy Finch, and Sony Computer Entertainment Inc. *COLLADA – Digital Asset Schema Release 1.5.0.* The Khronos Group Inc., P.O. Box 1019, Clearlake Park, CA 95424, U.S.A., April 2008.

Peter Bauer, Alan Thorpe, and Gilbert Brunet. The quiet revolution of numerical weather prediction. *Nature*, 525(7567):47–55, sep 2015. doi: 10.1038/nature14956. URL `https://doi.org/10.1038%2Fnature14956`.

C. Beekmans, J. Schneider, T. Läbe, M. Lennefer, C. Stachniss, and C. Simmer. Cloud photogrammetry with dense stereo for fisheye cameras. *Atmospheric Chemistry and Physics*, 16(22):14231–14248, 2016. doi: 10.5194/acp-16-14231-2016. URL `https://www.atmos-chem-phys.net/16/14231/2016/`.

Oren Ben-Kiki, Clark Evans, and Ingy döt Net. YAML Ain't Markup Language (YAML™) Version 1.2, 10 2009. URL `https://yaml.org/spec/1.2/spec.pdf`.

Matthew Bolitho, Michael Kazhdan, Randal Burns, and Hugues Hoppe. Parallel Poisson Surface Reconstruction. In *Proceedings of the 5th International Symposium on Advances in Visual Computing: Part I*, ISVC '09, pages 678–689, Berlin, Heidelberg, 2009. Springer-Verlag. ISBN 978-3-642-10330-8. doi: 10.1007/978-3-642-10331-5_63. URL `http://dx.doi.org/10.1007/978-3-642-10331-5_63`.

Sandrine Bony and Jean-Louis Dufresne. Marine boundary layer clouds at the heart of tropical cloud feedback uncertainties in climate models. *Geophysical Research Letters*, 32(20), 2005. doi: 10.1029/2005GL023851. URL `https://agupubs.onlinelibrary.wiley.com/doi/abs/10.1029/2005GL023851`.

Sandrine Bony, Bjorn Stevens, Dargan M. W. Frierson, Christian Jakob, Masa Kageyama, Robert Pincus, Theodore G. Shepherd, Steven C. Sherwood, A. Pier Siebesma, Adam H. Sobel, Masahiro Watanabe, and Mark J. Webb. Clouds, circulation and climate sensitivity. *Nature Geoscience*, 8:261, Mar 2015. URL `https://doi.org/10.1038/ngeo2398`. Perspective.

Sandrine Bony, Bjorn Stevens, Felix Ament, Sebastien Bigorre, Patrick Chazette, Susanne Crewell, Julien Delanoë, Kerry Emanuel, David Farrell, Cyrille Flamant, Silke Gross, Lutz Hirsch, Johannes Karstensen, Bernhard Mayer, Louise Nuijens, James H. Ruppert, Irina Sandu, Pier Siebesma, Sabrina Speich, Frédéric Szczap, Julien Totems, Raphaela Vogel, Manfred Wendisch, and Martin Wirth. EUREC4A: A Field Campaign to Elucidate the Couplings Between Clouds, Convection and Circulation. *Surveys in Geophysics*, 38(6):1529–1568, Nov 2017. ISSN 1573-0956. doi: 10.1007/s10712-017-9428-0. URL `https://doi.org/10.1007/s10712-017-9428-0`.

Jean-yves Bouguet. Pyramidal implementation of the Lucas Kanade feature tracker. *Intel Corporation, Microprocessor Research Labs*, 2000.

G. Bradski. The OpenCV Library. *Dr. Dobb's Journal of Software Tools*, 2000.

Gary Bradski and Adrian Kaehler. *Learning OpenCV - Computer Vision with the OpenCV Library*. O'Reilly Media, Inc., 1005 Gravenstein Highway North, Sebastopol, CA 95472, 2008. ISBN 978-0-596-55404-0.

I. N. Bronstein, K. A. Semendjajew, G. Musiol, and H. Mühlig. *Taschenbuch der Mathematik*. Wissenschaftlicher Verlag Harri Deutsch GmbH, Gräfstraße 47, 60486 Frankfurt am Main, 7 edition, 2008. ISBN 3817120079.

Robert Buras and Bernhard Mayer. Efficient unbiased variance reduction techniques for Monte Carlo simulations of radiative transfer in cloudy atmospheres: The solution . *Journal of Quantitative Spectroscopy and Radiative Transfer* , 112(3):434–447, 2011. ISSN 0022-4073. doi: http://dx.doi.org/10.1016/j.jqsrt.2010.10.005. URL `http://www.sciencedirect.com/science/article/pii/S0022407310003791`.

Robert Buras, Timothy Dowling, and Claudia Emde. New secondary-scattering correction in DISORT with increased efficiency for forward scattering. *Journal of Quantitative Spectroscopy and Radiative Transfer*, 112(12):2028–2034, 2011. ISSN 0022-4073. doi: https://doi.org/10.1016/j.jqsrt.2011.03.019. URL `http://www.sciencedirect.com/science/article/pii/S0022407311001385`.

S. Chandrasekhar. *Radiative transfer.* Dover Publications, New York, 1960. ISBN 9780486605906.

Charles Cox and Walter Munk. Measurement of the Roughness of the Sea Surface from Photographs of the Sun's Glitter. *J. Opt. Soc. Am.*, 44(11):838–850, Nov 1954. doi: 10.1364/JOSA.44.000838. URL `http://www.osapublishing.org/abstract.cfm?URI=josa-44-11-838`.

P. Crispel and G. Roberts. All-sky photogrammetry techniques to georeference a cloud field. *Atmospheric Measurement Techniques*, 11(1):593–609, 2018. doi: 10.5194/amt-11-593-2018. URL `https://www.atmos-meas-tech.net/11/593/2018/`.

R. Davies. The Effect of Finite Geometry on the Three-Dimensional Transfer of Solar Irradiance in Clouds. *Journal of the Atmospheric Sciences*, 35(9):1712–1725, 1978. doi: 10.1175/1520-0469(1978)035⟨1712:TEOFGO⟩2.0.CO;2. URL `https://doi.org/10.1175/1520-0469(1978)035<1712:TEOFGO>2.0.CO;2`.

Anthony Davis, Alexander Marshak, Robert Cahalan, and Warren Wiscombe. The Landsat Scale Break in Stratocumulus as a Three-Dimensional Radiative Transfer Effect: Implications for Cloud Remote Sensing. *Journal of the Atmospheric Sciences*, 54(2):241–260, 1997. doi: 10.1175/1520-0469(1997)054⟨0241:TLSBIS⟩2.0.CO;2. URL `https://doi.org/10.1175/1520-0469(1997)054<0241:TLSBIS>2.0.CO;2`.

B. N. Delaunay. Sur la sphère vide. *Bull. Acad. Sci. URSS*, 1934(6):793–800, 1934.

David H. Douglas and Thomas K. Peucker. Algorithms for the Reduction of the Number of Points Required to Represent a Digitized Line or its Caricature. *Cartographica: The International Journal for Geographic Information and Geovisualization*, 10(2):112–122, 1973. doi: 10.3138/FM57-6770-U75U-7727. URL `https://doi.org/10.3138/FM57-6770-U75U-7727`.

J. L. Dufresne and S. Bony. An Assessment of the Primary Sources of Spread of Global Warming Estimates from Coupled Atmosphere Ocean Models. *Journal of Climate*, 21: 5135, 2008. doi: 10.1175/2008JCLI2239.1.

Brian Eaton, Jonathan Gregory, Bob Drach, Karl Taylor, Steve Hankin, Jon Blower, John Caron, Rich Signell, Phil Bentley, Greg Rappa, Heinke Höck, Alison Pamment, Martin Juckes, and Martin Raspaud. CF Conventions and Metadata. `http://cfconventions.org/`, 10 2019.

C. Emde, R. Buras-Schnell, A. Kylling, B. Mayer, J. Gasteiger, U. Hamann, J. Kylling, B. Richter, C. Pause, T. Dowling, and L. Bugliaro. The libRadtran software package for radiative transfer calculations (version 2.0.1). *Geoscientific Model Development*, 9(5):1647–1672, 2016. doi: 10.5194/gmd-9-1647-2016. URL `https://www.geosci-model-dev.net/9/1647/2016/`.

F. Ewald, T. Kölling, A. Baumgartner, T. Zinner, and B. Mayer. Design and characterization of specMACS, a multipurpose hyperspectral cloud and sky imager. *Atmospheric Measurement Techniques*, 9(5):2015–2042, 2016. doi: 10.5194/amt-9-2015-2016. URL `http://www.atmos-meas-tech.net/9/2015/2016/`.

F. Ewald, T. Zinner, T. Kölling, and B. Mayer. Remote sensing of cloud droplet radius profiles using solar reflectance from cloud sides – Part 1: Retrieval development and characterization. *Atmospheric Measurement Techniques*, 12(2):1183–1206, 2019. doi: 10.5194/amt-12-1183-2019. URL `https://www.atmos-meas-tech-discuss.net/amt-2018-234/`.

Florian Ewald. *Retrieval of vertical profiles of cloud droplet effective radius using solar reflectance from cloud sides*. PhD thesis, LMU München, March 2016. URL `http://nbn-resolving.de/urn:nbn:de:bvb:19-205322`.

Tom G. Farr, Paul A. Rosen, Edward Caro, Robert Crippen, Riley Duren, Scott Hensley, Michael Kobrick, Mimi Paller, Ernesto Rodriguez, Ladislav Roth, David Seal, Scott Shaffer, Joanne Shimada, Jeffrey Umland, Marian Werner, Michael Oskin, Douglas Burbank, and Douglas Alsdorf. The Shuttle Radar Topography Mission. *Reviews of Geophysics*, 45(2), 2007. doi: 10.1029/2005RG000183. URL `https://agupubs.onlinelibrary.wiley.com/doi/abs/10.1029/2005RG000183`.

J. Fischer, W. Cordes, A. Schmitz-Peiffer, W. Renger, and P. Mörl. Detection of Cloud-Top Height from Backscattered Radiances within the Oxygen A Band. Part 2: Measurements. *Journal of Applied Meteorology*, 30(9):1260–1267, 1991. doi: 10.1175/1520-0450(1991)030⟨1260:DOCTHF⟩2.0.CO;2. URL `https://doi.org/10.1175/1520-0450(1991)030<1260:DOCTHF>2.0.CO;2`.

Sadayuki Furuhashi. MessagePack: It's like JSON. but fast and small. `https://msgpack.org/`, 10 2019.

Branko Grünbaum. *Convex Polytopes*. Springer New York, 2003. doi: 10.1007/978-1-4613-0019-9. URL `https://doi.org/10.1007%2F978-1-4613-0019-9`.

James E. Hansen and Larry D. Travis. Light scattering in planetary atmospheres. *Space Science Reviews*, 16(4):527–610, Oct 1974. ISSN 1572-9672. doi: 10.1007/BF00168069. URL `https://doi.org/10.1007/BF00168069`.

L. G. Henyey and J. L. Greenstein. Diffuse radiation in the Galaxy. *Astrophysical Journal*, 93:70–83, Jan 1941. doi: 10.1086/144246.

M. Hess, P. Koepke, and I. Schult. Optical Properties of Aerosols and Clouds: The Software Package OPAC. *Bulletin of the American Meteorological Society*, 79(5):831–844, 1998. doi: 10.1175/1520-0477(1998)079⟨0831:OPOAAC⟩2.0.CO;2. URL `https://doi.org/10.1175/1520-0477(1998)079<0831:OPOAAC>2.0.CO;2`.

Y. X. Hu and K. Stamnes. An Accurate Parameterization of the Radiative Properties of Water Clouds Suitable for Use in Climate Models. *Journal of Climate*, 6(4):728–742, 1993. doi: 10.1175/1520-0442(1993)006⟨0728:AAPOTR⟩2.0.CO;2. URL `https://doi.org/10.1175/1520-0442(1993)006<0728:AAPOTR>2.0.CO;2`.

IPCC. *Climate Change 2013: The Physical Science Basis. Contribution of Working Group I to the Fifth Assessment Report of the Intergovernmental Panel on Climate Change.* Cambridge University Press, Cambridge, United Kingdom and New York, NY, USA, 2013. ISBN ISBN 978-1-107-66182-0. doi: 10.1017/CBO9781107415324. URL `www.climatechange2013.org`.

M. Iqbal. *An introduction to solar radiation.* Academic Press, 1983. ISBN 9780123737526.

M. Jacob, F. Ament, M. Gutleben, H. Konow, M. Mech, M. Wirth, and S. Crewell. Investigating the liquid water path over the tropical Atlantic with synergistic airborne measurements. *Atmospheric Measurement Techniques*, 12(6):3237–3254, 2019. doi: 10.5194/amt-12-3237-2019. URL `https://www.atmos-meas-tech.net/12/3237/2019/`.

K. O. L. F. Jayaweera and B. J. Mason. The behaviour of freely falling cylinders and cones in a viscous fluid. *Journal of Fluid Mechanics*, 22(4):709–720, 1965. doi: 10.1017/S002211206500109X.

E. Jäkel, M. Wendisch, T. C. Krisna, F. Ewald, T. Kölling, T. Jurkat, C. Voigt, M. A. Cecchini, L. A. T. Machado, A. Afchine, A. Costa, M. Krämer, M. O. Andreae, U. Pöschl, D. Rosenfeld, and T. Yuan. Vertical distribution of the particle phase in tropical deep convective clouds as derived from cloud-side reflected solar radiation measurements. *Atmospheric Chemistry and Physics*, 17(14):9049–9066, 2017. doi: 10.5194/acp-17-9049-2017. URL `https://www.atmos-chem-phys.net/17/9049/2017/`.

Charles F. F. Karney. GeographicLib, version 2009-03, mar 2009. URL `https://doi.org/10.5281/zenodo.32463`.

Michael Kazhdan and Hugues Hoppe. Screened Poisson Surface Reconstruction. *ACM Trans. Graph.*, 32(3):29–1, jul 2013. ISSN 0730-0301. doi: 10.1145/2487228.2487237. URL `http://doi.acm.org/10.1145/2487228.2487237`.

Michael Kazhdan, Matthew Bolitho, and Hugues Hoppe. Poisson Surface Reconstruction. In *Proceedings of the Fourth Eurographics Symposium on Geometry Processing*, SGP '06, pages 61–70, Aire-la-Ville, Switzerland, Switzerland, 2006. Eurographics Association. ISBN 3-905673-36-3. URL `http://dl.acm.org/citation.cfm?id=1281957.1281965`.

M. D. King, W. P. Menzel, Y. J. Kaufman, D. Tanre, Bo-Cai Gao, S. Platnick, S. A. Ackerman, L. A. Remer, R. Pincus, and P. A. Hubanks. Cloud and aerosol properties, precipitable water, and profiles of temperature and water vapor from MODIS. *IEEE Transactions on Geoscience and Remote Sensing*, 41(2):442–458, Feb 2003. doi: 10.1109/TGRS.2002.808226.

Harald Koschmieder. Theorie der horizontalen Sichtweite. *Zeitschrift für die Erforschung der höheren Luftschichten*, 12:33–55, 1926.

Monika Krautstrunk and Andreas Giez. *The Transition From FALCON to HALO Era Airborne Atmospheric Research: Background – Methods – Trends*, pages 609–624. Springer Berlin Heidelberg, Berlin, Heidelberg, 2012. ISBN 978-3-642-30183-4. doi: 10.1007/978-3-642-30183-4_37. URL `https://doi.org/10.1007/978-3-642-30183-4_37`.

T Kölling. Characterization, calibration and operation of a hyperspectral sky imager. Master's thesis, LMU, München, March 2015.

T. Kölling, T. Zinner, and B. Mayer. Aircraft-based stereographic reconstruction of 3-D cloud geometry. *Atmospheric Measurement Techniques*, 12(2):1155–1166, 2019. doi: 10.5194/amt-12-1155-2019.

Johann Heinrich Lambert. *Photometrie.* Verlag von Wilhelm Engelmann, Leipzig, 1892.

William E. Lorensen and Harvey E. Cline. Marching Cubes: A High Resolution 3D Surface Construction Algorithm. *SIGGRAPH Comput. Graph.*, 21(4):163–169, aug 1987. ISSN 0097-8930. doi: 10.1145/37402.37422. URL `http://doi.acm.org.emedien.ub.uni-muenchen.de/10.1145/37402.37422`.

Bruce D. Lucas and Takeo Kanade. An Iterative Image Registration Technique with an Application to Stereo Vision. In *Proceedings of the 7th International Joint Conference on Artificial Intelligence - Volume 2*, IJCAI'81, pages 674–679, San Francisco, CA, USA, 1981. Morgan Kaufmann Publishers Inc.

J. David MacDonald and Kellogg S. Booth. Heuristics for ray tracing using space subdivision. *The Visual Computer*, 6(3):153–166, May 1990. ISSN 1432-2315. doi: 10.1007/BF01911006. URL `https://doi.org/10.1007/BF01911006`.

S. Maneewongvatana and Dave Mount. It's okay to be skinny, if your friends are fat. *Center for Geometric Computing 4th Annual Workshop on Computational Geometry*, 1999/// 1999.

A. Marshak, J. V. Martins, V. Zubko, and Y. J. Kaufman. What does reflection from cloud sides tell us about vertical distribution of cloud droplet sizes? *Atmospheric Chemistry and Physics*, 6(12):5295–5305, 2006. doi: 10.5194/acp-6-5295-2006. URL `https://www.atmos-chem-phys.net/6/5295/2006/`.

J. V. Martins, A. Marshak, L. A. Remer, D. Rosenfeld, Y. J. Kaufman, R. Fernandez-Borda, I. Koren, A. L. Correia, V. Zubko, and P. Artaxo. Remote sensing the vertical profile of cloud droplet effective radius, thermodynamic phase, and temperature. *Atmospheric Chemistry and Physics*, 11(18):9485–9501, 2011. doi: 10.5194/acp-11-9485-2011. URL `https://www.atmos-chem-phys.net/11/9485/2011/`.

B. Mayer. Radiative transfer in the cloudy atmosphere. *EPJ Web of Conferences*, 1: 75–99, 2009. doi: 10.1140/epjconf/e2009-00912-1. URL `http://dx.doi.org/10.1140/epjconf/e2009-00912-1`.

B. Mayer and A. Kylling. Technical note: The libRadtran software package for radiative transfer calculations - description and examples of use. *Atmospheric Chemistry and Physics*, 5(7):1855–1877, 2005. doi: 10.5194/acp-5-1855-2005. URL `https://www.atmos-chem-phys.net/5/1855/2005/`.

B. Mayer, M. Schröder, R. Preusker, and L. Schüller. Remote sensing of water cloud droplet size distributions using the backscatter glory: a case study. *Atmospheric Chemistry and Physics*, 4(5):1255–1263, 2004. doi: 10.5194/acp-4-1255-2004. URL `https://www.atmos-chem-phys.net/4/1255/2004/`.

M. Mech, E. Orlandi, S. Crewell, F. Ament, L. Hirsch, M. Hagen, G. Peters, and B. Stevens. HAMP – the microwave package on the High Altitude and LOng range research aircraft (HALO). *Atmospheric Measurement Techniques*, 7(12):4539–4553, 2014. doi: 10.5194/amt-7-4539-2014. URL `https://www.atmos-meas-tech.net/7/4539/2014/`.

Gustav Mie. Beiträge zur Optik trüber Medien, speziell kolloidaler Metallösungen. *Annalen der Physik*, 330(3):377–445, 1 1908. ISSN 1521-3889. doi: 10.1002/andp.19083300302. URL `https://doi.org/10.1002/andp.19083300302`.

C. Moroney, R. Davies, and J. P. Muller. Operational retrieval of cloud-top heights using MISR data. *IEEE Transactions on Geoscience and Remote Sensing*, 40(7):1532–1540, Jul 2002. ISSN 0196-2892. doi: 10.1109/TGRS.2002.801150.

Ken Museth. VDB: High-resolution Sparse Volumes with Dynamic Topology. *ACM Trans. Graph.*, 32(3):27–1, jul 2013. ISSN 0730-0301. doi: 10.1145/2487228.2487235. URL `http://doi.acm.org/10.1145/2487228.2487235`.

Teruyuki Nakajima and Michael D. King. Determination of the Optical Thickness and Effective Particle Radius of Clouds from Reflected Solar Radiation Measurements. Part I: Theory. *Journal of the Atmospheric Sciences*, 47(15):1878–1893, 1990. doi: 10.1175/1520-0469(1990)047⟨1878:DOTOTA⟩2.0.CO;2. URL `https://doi.org/10.1175/1520-0469(1990)047<1878:DOTOTA>2.0.CO;2`.

NIMA Geodesy and Geophysics Department. NGA: DoD World Geodetic System 1984. Technical Report 8350.2, National Imagery and Mapping Agency, 3200 South Second

Street, St. Louis, MO 63118-3399, June 2004. URL `https://earth-info.nga.mil/GandG/publications/tr8350.2/tr8350_2.html`.

A. Ono. The Shape and Riming Properties of Ice Crystals in Natural Clouds. *Journal of the Atmospheric Sciences*, 26(1):138–147, 1969. doi: 10.1175/1520-0469(1969)026⟨0138:TSARPO⟩2.0.CO;2. URL `https://doi.org/10.1175/1520-0469(1969)026<0138:TSARPO>2.0.CO;2`.

Sabrina Jessica Pavicic. Cloudfraction during the NARVAL-2 campaign. Master's thesis, Ludwig-Maximilians Universität, München, 2018.

Nikolaos K. Pavlis, Simon A. Holmes, Steve C. Kenyon, and John K. Factor. The development and evaluation of the Earth Gravitational Model 2008 (EGM2008). *Journal of Geophysical Research: Solid Earth*, 117(B4), 2012. doi: 10.1029/2011JB008916. URL `https://agupubs.onlinelibrary.wiley.com/doi/abs/10.1029/2011JB008916`.

Thomas K. Peucker, Robert J. Fowler, James J. Little, and David M. Mark. Digital Representation of Three-Dimensional Surfaces By Triangulated Irregular Networks (TIN). Technical report, Office of Naval Research, Geography Programs, October 1976. URL `https://archive.org/details/DTIC_ADA094241`.

Matt Pharr, Wenzel Jakob, and Greg Humphreys. *Physically based rendering : from theory to implementation*. Morgan Kaufmann Publishers, Cambridge, MA, 2017.

Les Piegl and Wayne Tiller. *The NURBS Book*. Springer Berlin Heidelberg, 1995. doi: 10.1007/978-3-642-97385-7. URL `https://doi.org/10.1007/978-3-642-97385-7`.

S. Platnick, M. D. King, S. A. Ackerman, W. P. Menzel, B. A. Baum, J. C. Riedi, and R. A. Frey. The MODIS cloud products: algorithms and examples from Terra. *IEEE Transactions on Geoscience and Remote Sensing*, 41(2):459–473, Feb 2003. doi: 10.1109/TGRS.2002.808301.

C. M. R. Platt. Lidar Backscatter from Horizontal Ice Crystal Plates. *Journal of Applied Meteorology*, 17(4):482–488, 1978. doi: 10.1175/1520-0450(1978)017⟨0482:LBFHIC⟩2.0.CO;2. URL `https://doi.org/10.1175/1520-0450(1978)017<0482:LBFHIC>2.0.CO;2`.

PROJ. *PROJ coordinate transformation software library*, 2019. URL `https://proj.org/`.

H. R. Pruppacher and R. L. Pitter. A Semi-Empirical Determination of the Shape of Cloud and Rain Drops. *Journal of the Atmospheric Sciences*, 28(1):86–94, 1971. doi: 10.1175/1520-0469(1971)028⟨0086:ASEDOT⟩2.0.CO;2. URL `https://doi.org/10.1175/1520-0469(1971)028<0086:ASEDOT>2.0.CO;2`.

Veronika Pörtge. Cloud Droplet Size Distributions from Observations of Glory and Cloudbow. Master's thesis, Ludwig-Maximilians-Universität München, 11 2019.

Urs Ramer. An iterative procedure for the polygonal approximation of plane curves. *Computer Graphics and Image Processing*, 1(3):244–256, 1972. ISSN 0146-664X. doi: https://doi.org/10.1016/S0146-664X(72)80017-0. URL `http://www.sciencedirect.com/science/article/pii/S0146664X72800170`.

R. A. Roebeling, A. J. Feijt, and P. Stammes. Cloud property retrievals for climate monitoring: Implications of differences between Spinning Enhanced Visible and Infrared Imager (SEVIRI) on METEOSAT-8 and Advanced Very High Resolution Radiometer (AVHRR) on NOAA-17. *Journal of Geophysical Research: Atmospheres*, 111(D20), 2006. doi: 10.1029/2005JD006990. URL `https://agupubs.onlinelibrary.wiley.com/doi/abs/10.1029/2005JD006990`.

David M. Romps and Ruşen Öktem. Observing clouds in 4D with multi-view stereo photogrammetry. *Bulletin of the American Meteorological Society*, 0(0), 2018. doi: 10.1175/BAMS-D-18-0029.1. URL `https://doi.org/10.1175/BAMS-D-18-0029.1`.

Radu Bogdan Rusu. *Semantic 3D Object Maps for Everyday Manipulation in Human Living Environments*. PhD thesis, Technische Universität München, München, 2009.

Radu Bogdan Rusu and Steve Cousins. 3D is here: Point Cloud Library (PCL). In *IEEE International Conference on Robotics and Automation (ICRA)*, Shanghai, China, May 9-13 2011.

Ulrich Schwarz. Derivation of cloud geometry with imaging spectral and geometric measurements. Master's thesis, Ludwig-Maximilians-Universität München, 03 2016.

Andreas Schäfler, George Craig, Heini Wernli, Philippe Arbogast, James D. Doyle, Ron McTaggart-Cowan, John Methven, Gwendal Rivière, Felix Ament, Maxi Boettcher, Martina Bramberger, Quitterie Cazenave, Richard Cotton, Susanne Crewell, Julien Delanoë, Andreas Dörnbrack, André Ehrlich, Florian Ewald, Andreas Fix, Christian M. Grams, Suzanne L. Gray, Hans Grob, Silke Groß, Martin Hagen, Ben Harvey, Lutz Hirsch, Marek Jacob, Tobias Kölling, Heike Konow, Christian Lemmerz, Oliver Lux, Linus Magnusson, Bernhard Mayer, Mario Mech, Richard Moore, Jacques Pelon, Julian Quinting, Stephan Rahm, Markus Rapp, Marc Rautenhaus, Oliver Reitebuch, Carolyn A. Reynolds, Harald Sodemann, Thomas Spengler, Geraint Vaughan, Manfred Wendisch, Martin Wirth, Benjamin Witschas, Kevin Wolf, and Tobias Zinner. The North Atlantic Waveguide and Downstream Impact Experiment. *Bulletin of the American Meteorological Society*, 99(8):1607–1637, 2018. doi: 10.1175/BAMS-D-17-0003.1. URL `https://doi.org/10.1175/BAMS-D-17-0003.1`.

T. W. Sederberg, D. C. Anderson, and R. N. Goldman. Implicit representation of parametric curves and surfaces. *Computer Vision, Graphics, and Image Processing*, 28(1): 72–84, 1984. ISSN 0734-189X. doi: https://doi.org/10.1016/0734-189X(84)90140-3. URL `http://www.sciencedirect.com/science/article/pii/0734189X84901403`.

Gabriela Seiz, Roger Davies, and Armin Grün. Stereo cloud-top height retrieval with ASTER and MISR. *International Journal of Remote Sensing*, 27(9):1839–1853, 2006. doi: 10.1080/01431160500380703. URL `https://doi.org/10.1080/01431160500380703`.

SensorML. OGC® SensorML: Model and XML Encoding Standard. OGC 12-000, Open Geospatial Consortium, Feb 2014. URL `http://www.opengis.net/doc/IS/SensorML/2.0`.

Jianbo Shi and C. Tomasi. Good features to track. In *1994 Proceedings of IEEE Conference on Computer Vision and Pattern Recognition*, pages 593–600, Jun 1994. doi: 10.1109/CVPR.1994.323794.

A. Slingo and J. M. Slingo. The response of a general circulation model to cloud longwave radiative forcing. I: Introduction and initial experiments. *Quarterly Journal of the Royal Meteorological Society*, 114(482):1027–1062, 1988. ISSN 1477-870X. doi: 10.1002/qj.49711448209. URL `http://dx.doi.org/10.1002/qj.49711448209`.

Knut Stamnes, S-Chee Tsay, Warren Wiscombe, and Kolf Jayaweera. Numerically stable algorithm for discrete-ordinate-method radiative transfer in multiple scattering and emitting layered media. *Appl. Opt.*, 27(12):2502–2509, Jun 1988. doi: 10.1364/AO.27.002502. URL `http://ao.osa.org/abstract.cfm?URI=ao-27-12-2502`.

Bjorn Stevens, Chin-Hoh Moeng, Andrew S. Ackerman, Christopher S. Bretherton, Andreas Chlond, Stephan de Roode, James Edwards, Jean-Christophe Golaz, Hongli Jiang, Marat Khairoutdinov, Michael P. Kirkpatrick, David C. Lewellen, Adrian Lock, Frank Müller, David E. Stevens, Eoin Whelan, and Ping Zhu. Evaluation of Large-Eddy Simulations via Observations of Nocturnal Marine Stratocumulus. *Monthly Weather Review*, 133(6):1443–1462, 2005. doi: {10.1175/MWR2930.1}. URL `https://doi.org/10.1175/MWR2930.1`.

Bjorn Stevens, Felix Ament, Sandrine Bony, Susanne Crewell, Florian Ewald, Silke Gross, Akio Hansen, Lutz Hirsch, Marek Jacob, Tobias Kölling, Heike Konow, Bernhard Mayer, Manfred Wendisch, Martin Wirth, Kevin Wolf, Stephan Bakan, Matthias Bauer-Pfundstein, Matthias Brueck, Julien Delanoë, André Ehrlich, David Farrell, Marvin Forde, Felix Gödde, Hans Grob, Martin Hagen, Evelyn Jäkel, Friedhelm Jansen, Christian Klepp, Marcus Klingebiel, Mario Mech, Gerhard Peters, Markus Rapp, Allison A. Wing, and Tobias Zinner. A High-Altitude Long-Range Aircraft Configured as a Cloud Observatory: The NARVAL Expeditions. *Bulletin of the American Meteorological Society*, 100(6):1061–1077, 2019. doi: 10.1175/BAMS-D-18-0198.1. URL `https://doi.org/10.1175/BAMS-D-18-0198.1`.

Kathleen I. Strabala, Steven A. Ackerman, and W. Paul Menzel. Cloud Properties inferred from 8 - 12-µm Data. *Journal of Applied Meteorology*, 33(2):212–229, 1994. doi:

10.1175/1520-0450(1994)033⟨0212:CPIFD⟩2.0.CO;2. URL `https://doi.org/10.1175/1520-0450(1994)033<0212:CPIFD>2.0.CO;2`.

Thomas Trost. Electrostatic discharge (ESD)—Facts and faults—A review. *Packaging Technology and Science*, 8(5):231–247, 1995. doi: 10.1002/pts.2770080502. URL `https://onlinelibrary.wiley.com/doi/abs/10.1002/pts.2770080502`.

B. Vant-Hull, A. Marshak, L. A. Remer, and Z. Li. The Effects of Scattering Angle and Cumulus Cloud Geometry on Satellite Retrievals of Cloud Droplet Effective Radius. *IEEE Transactions on Geoscience and Remote Sensing*, 45(4):1039–1045, April 2007. ISSN 0196-2892. doi: 10.1109/TGRS.2006.890416.

Tamás Várnai and Alexander Marshak. Observations of Three-Dimensional Radiative Effects that Influence MODIS Cloud Optical Thickness Retrievals. *Journal of the Atmospheric Sciences*, 59(9):1607–1618, 2002. doi: 10.1175/1520-0469(2002)059⟨1607:OOTDRE⟩2.0.CO;2. URL `https://doi.org/10.1175/1520-0469(2002)059<1607:OOTDRE>2.0.CO;2`.

Tamás Várnai and Alexander Marshak. A method for analyzing how various parts of clouds influence each other's brightness. *Journal of Geophysical Research: Atmospheres*, 108 (D22), 2003. ISSN 2156-2202. doi: 10.1029/2003JD003561. URL `http://dx.doi.org/10.1029/2003JD003561`. 4706.

Hans Wallach. Über visuell wahrgenommene Bewegungsrichtung. *Psychologische Forschung*, 20(1):325–380, Dec 1935. ISSN 1430-2772. doi: 10.1007/BF02409790. URL `https://doi.org/10.1007/BF02409790`.

M. J. Webb, C. A. Senior, D. M. H. Sexton, W. J. Ingram, K. D. Williams, M. A. Ringer, B. J. McAvaney, R. Colman, B. J. Soden, R. Gudgel, T. Knutson, S. Emori, T. Ogura, Y. Tsushima, N. Andronova, B. Li, I. Musat, S. Bony, and K. E. Taylor. On the contribution of local feedback mechanisms to the range of climate sensitivity in two GCM ensembles. *Climate Dynamics*, 27(1):17–38, Jul 2006. ISSN 1432-0894. doi: 10.1007/s00382-006-0111-2. URL `https://doi.org/10.1007/s00382-006-0111-2`.

Anna Weber. Retrieval of Cloud Droplet Size Distribution from Polarised Aircraft Observations of the Cloudbow. Master's thesis, Ludwig-Maximilians-Universität München, 08 2019.

Manfred Wendisch, Dörthe Müller, Dieter Schell, and Jost Heintzenberg. An Airborne Spectral Albedometer with Active Horizontal Stabilization. *Journal of Atmospheric and Oceanic Technology*, 18(11):1856–1866, 2001. doi: 10.1175/1520-0426(2001)018⟨1856:AASAWA⟩2.0.CO;2. URL `https://doi.org/10.1175/1520-0426(2001)018<1856:AASAWA>2.0.CO;2`.

Manfred Wendisch, Ulrich Pöschl, Meinrat O. Andreae, Luiz A. T. Machado, Rachel Albrecht, Hans Schlager, Daniel Rosenfeld, Scot T. Martin, Ahmed Abdelmonem, Armin

Afchine, Alessandro C. Araùjo, Paulo Artaxo, Heinfried Aufmhoff, Henrique M. J. Barbosa, Stephan Borrmann, Ramon Braga, Bernhard Buchholz, Micael Amore Cecchini, Anja Costa, Joachim Curtius, Maximilian Dollner, Marcel Dorf, Volker Dreiling, Volker Ebert, André Ehrlich, Florian Ewald, Gilberto Fisch, Andreas Fix, Fabian Frank, Daniel Fütterer, Christopher Heckl, Fabian Heidelberg, Tilman Hüneke, Evelyn Jäkel, Emma Järvinen, Tina Jurkat, Sandra Kanter, Udo Kästner, Mareike Kenntner, Jürgen Kesselmeier, Thomas Klimach, Matthias Knecht, Rebecca Kohl, Tobias Kölling, Martina Krämer, Mira Krüger, Trismono Candra Krisna, Jost V. Lavric, Karla Longo, Christoph Mahnke, Antonio O. Manzi, Bernhard Mayer, Stephan Mertes, Andreas Minikin, Sergej Molleker, Steffen Münch, Björn Nillius, Klaus Pfeilsticker, Christopher Pöhlker, Anke Roiger, Diana Rose, Dagmar Rosenow, Daniel Sauer, Martin Schnaiter, Johannes Schneider, Christiane Schulz, Rodrigo A. F. de Souza, Antonio Spanu, Paul Stock, Daniel Vila, Christiane Voigt, Adrian Walser, David Walter, Ralf Weigel, Bernadett Weinzierl, Frank Werner, Marcia A. Yamasoe, Helmut Ziereis, Tobias Zinner, and Martin Zöger. ACRIDICON–CHUVA Campaign: Studying Tropical Deep Convective Clouds and Precipitation over Amazonia Using the New German Research Aircraft HALO. *Bulletin of the American Meteorological Society*, 97(10):1885–1908, 2016. doi: 10.1175/BAMS-D-14-00255.1. URL `http://dx.doi.org/10.1175/BAMS-D-14-00255.1`.

M. Wirth, A. Fix, P. Mahnke, H. Schwarzer, F. Schrandt, and G. Ehret. The airborne multi-wavelength water vapor differential absorption lidar WALES: system design and performance. *Applied Physics B*, 96(1):201, Feb 2009. ISSN 1432-0649. doi: 10.1007/s00340-009-3365-7. URL `https://doi.org/10.1007/s00340-009-3365-7`.

W. J. Wiscombe. Improved Mie scattering algorithms. *Appl. Opt.*, 19(9):1505–1509, May 1980. doi: 10.1364/AO.19.001505. URL `http://ao.osa.org/abstract.cfm?URI=ao-19-9-1505`.

WMO. *Guide to meteorological instruments and methods of observation.* World Meteorological Organization, Geneva, Switzerland, 2014 edition, 2017. ISBN 978-92-63-10008-5.

Sven Woop, Carsten Benthin, and Ingo Wald. Watertight Ray/Triangle Intersection. *Journal of Computer Graphics Techniques (JCGT)*, 2(1):65–82, June 2013. ISSN 2331-7418. URL `http://jcgt.org/published/0002/01/05/`.

Matthew C. Wyant, Christopher S. Bretherton, Julio T. Bacmeister, Jeffrey T. Kiehl, Isaac M. Held, Ming Zhao, Stephen A. Klein, and Brian J. Soden. A comparison of low-latitude cloud properties and their response to climate change in three AGCMs sorted into regimes using mid-tropospheric vertical velocity. *Climate Dynamics*, 27(2):261–279, Aug 2006. ISSN 1432-0894. doi: 10.1007/s00382-006-0138-4. URL `https://doi.org/10.1007/s00382-006-0138-4`.

Zhengyou Zhang. A Flexible New Technique for Camera Calibration. volume 22, pages 1330–1334, December 2000. URL `https://www.microsoft.com/en-us/research/publication/a-flexible-new-technique-for-camera-calibration/`.

T. Zinner and B. Mayer. Remote sensing of stratocumulus clouds: Uncertainties and biases due to inhomogeneity. *Journal of Geophysical Research: Atmospheres*, 111(D14), 2006. doi: 10.1029/2005JD006955. URL `https://agupubs.onlinelibrary.wiley.com/doi/abs/10.1029/2005JD006955`.

T. Zinner, B. Mayer, and M. Schröder. Determination of three-dimensional cloud structures from high-resolution radiance data. *Journal of Geophysical Research: Atmospheres*, 111(D8), 2006. doi: 10.1029/2005JD006062. URL `https://agupubs.onlinelibrary.wiley.com/doi/abs/10.1029/2005JD006062`.

T. Zinner, A. Marshak, S. Lang, J. V. Martins, and B. Mayer. Remote sensing of cloud sides of deep convection: towards a three-dimensional retrieval of cloud particle size profiles. *Atmospheric Chemistry and Physics*, 8(16):4741–4757, 2008. doi: 10.5194/acp-8-4741-2008. URL `http://www.atmos-chem-phys.net/8/4741/2008/`.

T. Zinner, U. Schwarz, T. Kölling, F. Ewald, E. Jäkel, B. Mayer, and M. Wendisch. Cloud geometry from oxygen-A-band observations through an aircraft side window. *Atmospheric Measurement Techniques*, 12(2):1167–1181, 2019. doi: 10.5194/amt-12-1167-2019. URL `https://www.atmos-meas-tech-discuss.net/amt-2018-220/`.

Acknowledgements

The work of this thesis would not have been possible without the help of a lot of great people contributing directly or indirectly to it. Without any of them it also would not have been even close as much fun as it has been. I want to name a few but this will never be exhaustive. I often remember the email from Tobias advertising a fun time working on this new shiny specMACS instrument waiting on the rooftop right in the building where I was reading. Just a few minutes later, I did my fist steps into the meteorological institute and the chair of Prof. Bernhard Mayer. Tobias and Bernhard directly guided me to the roof where Flo immediately showed me the instrument, of which I did not yet know how much time I would be spending on. During my first field campaign, only a few weeks later, I was told about cirrus and cumulus and all the rest. Without them, I would not even got close to be doing a PhD at a meteorological institute and their continuous support and open ear has been invaluable throughout all the time. I also want to thank Linda, who is most certainly the longest office colleague I had. It always has been a great time! On the first day at the institute, my desk has been full of her newest electronics and as I am writing this, she's occupying that same place again. Of course Hans is the best guy to steal a year worth of PhD from and to drive on a car rally with. The time in preparing and running NARVAL-II and NAWDEX has been awesome, including ”SLS in a week”, which has been a great idea! Getting around would also not have been possible without the great support from Garfield and Barbara. Nici created this huge box around specMACS, without her and the whole enviscope team, it would not have been thinkable to do a last minute sneak into HALOs infamous boiler room. Building all the required hardware would also not be possible without Meinhard and Anton. And then, there's Tommy. He always has a thumb up, and the best coffee in the air. I always enjoyed working with Anna and Veronika, who helped in the preparations of EUREC^{4}A and did the analyses of glory and cloudbow. Fabi showed to me the world of triangles, mostly at night time though. There also have been some squares, he calls them ”Bladdeen” and they are quite heavy. I remember many evenings with Kulla, discussing about everything. By the way, he's also quite good at maths. Tete is simply great! She also tought me about the advantages of ship office and her comments to this document have been very helpful. I also want to thank all my friends and family for supporting me, in particular during the final phase of this work, where I quite possibly was not available to them as much as I would have liked to be.

Statement of Authorship

Erklärung:

Hiermit erkläre ich, die vorliegende Arbeit selbständig verfasst zu haben und keine anderen als die in der Arbeit angegebenen Quellen und Hilfsmittel benutzt zu haben.

Tobias Kölling
München, den 16.01.2020